



Geomechanical Interpretation of Microseismicity at  
the Preston New Road PNR-1z Well, Lancashire,  
England

August 2019

Report Commissioned by the Oil and Gas Authority, London

Report Internal ID: OLG.OGA-PNR2

**Authors:**

Dr. James Verdon, Lead Geophysicist, Outer Limits Geophysics LLP

Mr Tom Kettleby, Contract Geophysicist, Outer Limits Geophysics LLP

Professor Michael Kendall, Lead Geophysicist, Outer Limits Geophysics LLP

## SUMMARY

- This report analyses and interprets microseismicity recorded during hydraulic fracturing at the PNR-1z well, Lancashire, in October – December 2018, with a focus on understanding the causative mechanisms for the induced seismicity that occurred.
- We combine observations of event focal mechanisms, spatial distribution of moment release, and events during the injection hiatus, to identify a pre-existing fault on which most of the larger events occurred.
- We identify several features in the microseismic data that could not be easily explained through either simple pore pressure increases from the well or hydraulic fracture growth. Instead, we investigate the role that elastic stress transfer may have played in controlling the seismicity.
- We develop a stochastic modelling process to investigate the impact of tensile hydraulic fracture opening on the stress state in the surrounding rocks. We find that most events occur in regions that experience stress changes that promote failure on features that have the same orientation as the fault. This implies that stress transfer is playing a significant role in controlling where the microseismicity occurs.
- We compute the stress change transferred to nearby faults identified by 3D seismic surveys, but find that stress transfer effects on the larger faults are not significant. Two of the “seismic discontinuities” identified in the HFP do experience significant, positive stress changes, but no microseismicity occurs on these features.
- We also develop simple fluid-flow models to simulate the diffusion of elevated pressures into the subsurface. These concur with the assessments described above in that the spatio-temporal evolution of some of the microseismicity is difficult to explain through simple pressure-diffusion effects.
- The fluid-flow models also indicate that, regardless of the fault zone permeability, elevated pressures would have occurred along its length. Therefore the distribution of microseismicity can be used to infer that the overall dimensions of the fault are constrained to a zone extending from approximately the position of Stage 18 to Stage 39/40, and to a maximum distance of approximately 200 m from the well.

## DISCLAIMER

Forecasts, projections and forward-looking statements contained in this presentation are derived from geophysical modelling based on a range of parameters that are not necessarily well constrained. Therefore the nature of this work entails a number of risks, uncertainties or assumptions. Hence, no representation or warranty is given as to the achievement or reasonableness of any projections, estimates, forecasts or forward-looking statements contained in this presentation.

3rd party information contained in the presentation is believed to be accurate. However, the authors disclaim any liability if such information is found to be inaccurate.

The dissemination of this presentation nor its contents is to be taken as any form of commitment on the part of the author to enter any contract or otherwise legally binding obligation or commitment. The authors expressly reserve the right without prior notice or liability to terminate discussions with any recipient or other parties.

All material is copyright. It may be produced in whole or in part subject to the inclusion of an acknowledgement of the source, but should not be included in any commercial usage or sale. Reproduction for purposes other than those indicated above requires the written permission of the authors.

## 1. INTRODUCTION

This report provides a geomechanical interpretation of microseismicity induced by hydraulic fracturing of the Preston New Road PNR-1z well, situated on the Fylde Peninsula, Lancashire, by Cuadrilla Resources Ltd. (CRL) in October to December, 2018. During this operation, microseismic events exceeded the UK Traffic Light Scheme (TLS) red light threshold of  $M_L = 0.5$  on several occasions.

Each exceedance of the red light required the operator to stop injection, conduct well-integrity assessment checks, reduce pressure in the well, and pause operations for a period of at least 18 hours. The largest event that occurred had a magnitude of  $M_L = 1.5$ : this event was felt by some local residents near to the pad. Seismicity of this magnitude occurs when the hydraulic fractures interact with and reactivate pre-existing faults in the subsurface (e.g., Maxwell et al., 2008; Maxwell et al., 2009; Kettlety et al., 2019; Igonin et al., 2019; Eyre et al., 2019).

Hydraulic fracturing in PNR-1z was monitored by a combination of surface and downhole arrays. The surface array used a network of geophones and broadband seismometers buried roughly 50 cm into the topsoil. The purpose of the surface array was to administer the TLS: it was able to detect events with magnitudes from approximately  $M = -0.5$  and above.

The downhole array consisted of 24 3-component borehole geophones, placed at over 1,500 m depth in the PNR-2 well, roughly 200 m laterally and above the nearest stages in PNR-1z. The purpose of the downhole array was to provide high-resolution monitoring of the propagation of hydraulic fractures. The proximity of this array to the hydraulic fracturing allows it to pick up very small microseismic events, with magnitudes down to  $M = -2$ . At PNR-1z, this array recorded more than 39,000 microseismic events, the majority of which were far too small to be detected by the surface monitoring array. The microseismicity can be used to image the interaction between the hydraulic fractures and any pre-existing faults, and thereby gain a greater understanding of how the hydraulic fracturing led to fault reactivation.

### 1.1. MECHANISMS FOR FAULT REACTIVATION DURING HYDRAULIC FRACTURING

Fault reactivation by subsurface human activities is typically described with respect to the *in situ* stress conditions resolved into normal ( $\sigma_n$ ) and shear ( $\tau$ ) stresses acting on a fault. If the shear stress exceeds the Mohr-Coulomb failure envelope given by:

$$\tau > \phi(\sigma_n - P) + C, \quad (1)$$

where  $P$  is the pore pressure,  $\phi$  is the friction coefficient and  $C$  is the cohesion, then the fault will slip, potentially causing seismicity (although “slow”, aseismic slip can also occur). Equation (1) can be re-written in terms of the Coulomb Failure Stress,  $CFS$ :

$$CFS = \tau - \phi(\sigma_n - P), \quad (2)$$

where a change in  $CFS$ , noted hereafter as  $\Delta CFS$ , that is positive implies that the stress conditions are moving towards the failure threshold, increasing the likelihood of induced seismicity.

Equation (2) shows that failure can be reached in a number of ways: by increasing the shear stress; by decreasing the normal stress; or by increasing the pore pressure. Hydraulic fracturing will always cause an increase in  $P$  as fluid is injected into the subsurface, while periods of flowback will have the opposite effect. Depending on the relative orientations and positions of both the hydraulic fracturing and the pre-existing faults in question, the tensile opening of hydraulic fractures can cause either increases or decreases in either  $\sigma_n$  or  $\tau$ .

Figure 1.1. depicts several methods by which hydraulic fracturing can lead to fault slip. These effects may complement each other, or they may counteract each other, depending on the specific geomechanical conditions at a particular site, and the position and orientation of the fault with respect to the hydraulic fractures.

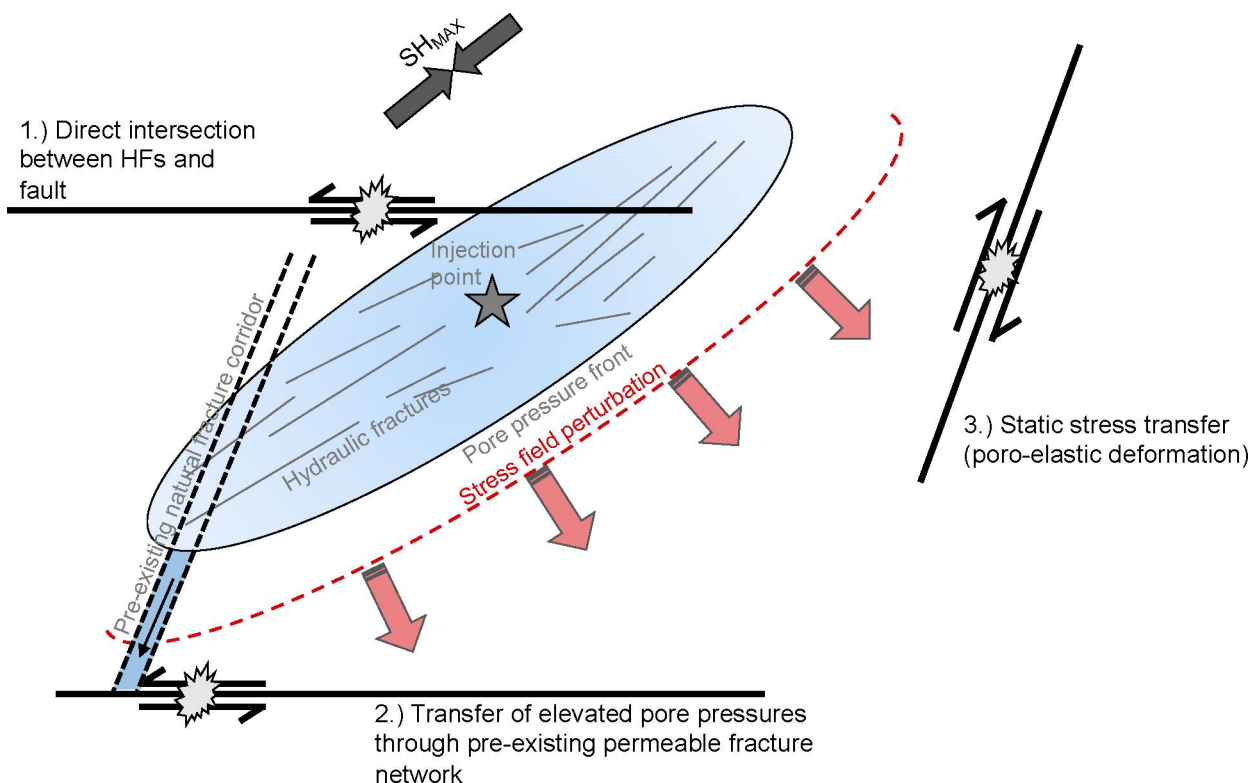


Figure 1.1: Schematic showing the various mechanisms by which hydraulic fracturing can reactivate faults. Adapted from Igonin et al. (2019).

Hydraulic fracturing fluid is injected into the subsurface at elevated pressures. If the hydraulic fractures directly intersect a fault, then the pressurised fluid may propagate into the fault zone, increasing the pore pressure, resulting in positive  $\Delta CFS$  as described by Equation (2). As such, pore pressure increase produced by direct intersection between hydraulic fractures and faults (Mechanism 1 in Figure 1.1) is well established as a mechanism for induced seismicity.

Shale rocks have very low matrix permeabilities, which means that it will take a long time for elevated pressures to move away from the stimulated volume of rock (e.g. Shapiro and Dinske, 2009). However, fault reactivation has been observed during hydraulic fracturing at distances that are too large, or at times that are too short, to be reasonably explained by pore pressure transfer

through low permeability shale rock (e.g., Schultz et al., 2015; Bao and Eaton, 2016; Deng et al., 2016; Igonin et al., 2019).

These observations imply that alternative triggering mechanisms may also act to create induced seismicity during hydraulic fracturing. The two triggering mechanisms that are most commonly inferred in such cases are (i) poro-elastic stress transfer (e.g., Deng et al., 2016; Bao and Eaton, 2016), and (ii) the presence of higher-permeability pathways that facilitate rapid transfer of pore pressure perturbations to larger distances (e.g., Holland et al., 2013; Schultz et al., 2015; Igonin et al., 2019).

The tensile opening of hydraulic fractures will create displacement, and therefore strain, in the surrounding rocks. This strain will be accompanied by a change in the stress field (Wang et al., 2006), impacting both  $\sigma_n$  and  $\tau$  acting on a fault. The nature of these changes will depend on the orientation of the fault and its position relative to the fractures, and can either promote or inhibit failure, as determined by the sign of the resulting  $\Delta CFS$  value. This stress transfer occurs instantaneously, and may occur over larger distances than the pore pressure pulse associated with injection (e.g., Deng et al., 2016). This mechanism may therefore provide a potential explanation for events that occur at relatively large distances (more than a few hundred metres) from the injection well (Mechanism 3 in Figure 1.1). Stress transfer produced by deformation of planar features in the subsurface is often invoked to explain distributions of aftershocks after a larger earthquake (e.g., Stein, 1999), and distributions of earthquakes as dykes propagate in volcanic settings (e.g., Toda et al., 2002; Green et al., 2015).

Although the matrix permeability of shale rocks is very low, the presence of pre-existing fracture networks or fracture corridors may provide locally-enhanced permeability (e.g., Questiaux et al., 2010). This is particularly true of fractures that are aligned near to the critical stress state, i.e., such that the  $CFS$  value is maximised (Rogers, 2003; Ghanizadeh et al., 2015). Fracture corridors may therefore provide a means by which elevated pore pressures are transmitted from the well, reactivating faults that are at greater distance from the well than might be expected given the low matrix permeabilities of shale rocks (Mechanism 2 in Figure 1.1) (e.g., Igonin et al., 2019).

The purpose of this report is to analyse and interpret the observed downhole microseismic data, in order to identify any pre-existing faults that were reactivated by the hydraulic fracturing, and to investigate the causative mechanisms by which the faults were reactivated.

## 2. MICROSEISMIC MONITORING AT PNR

A surface monitoring array and a downhole geophone array were used in combination to monitor the microseismicity at the Preston New Road site. The monitoring array setup and observations, including the use of microseismic observations to manage induced seismicity in real time, are described in more detail by Clarke et al. (2019), but for completeness are briefly re-capped here.

### 2.1. SURFACE ARRAY

The primary objective of the surface monitoring array was to provide accurate local magnitudes for larger events ( $M_L > 0$ ) in order to administer the TLS. The array, shown in Figure 2.1, consisted of 2 broadband seismometers and 6 geophones deployed by CRL, augmented by 4 seismometers deployed by the British Geological Survey (BGS). During real-time monitoring, the surface array detected 54 events with a minimum magnitude of  $M_L = -0.8$ . The aperture of the surface array was sufficient to enable focal mechanisms to be determined for many of the events.

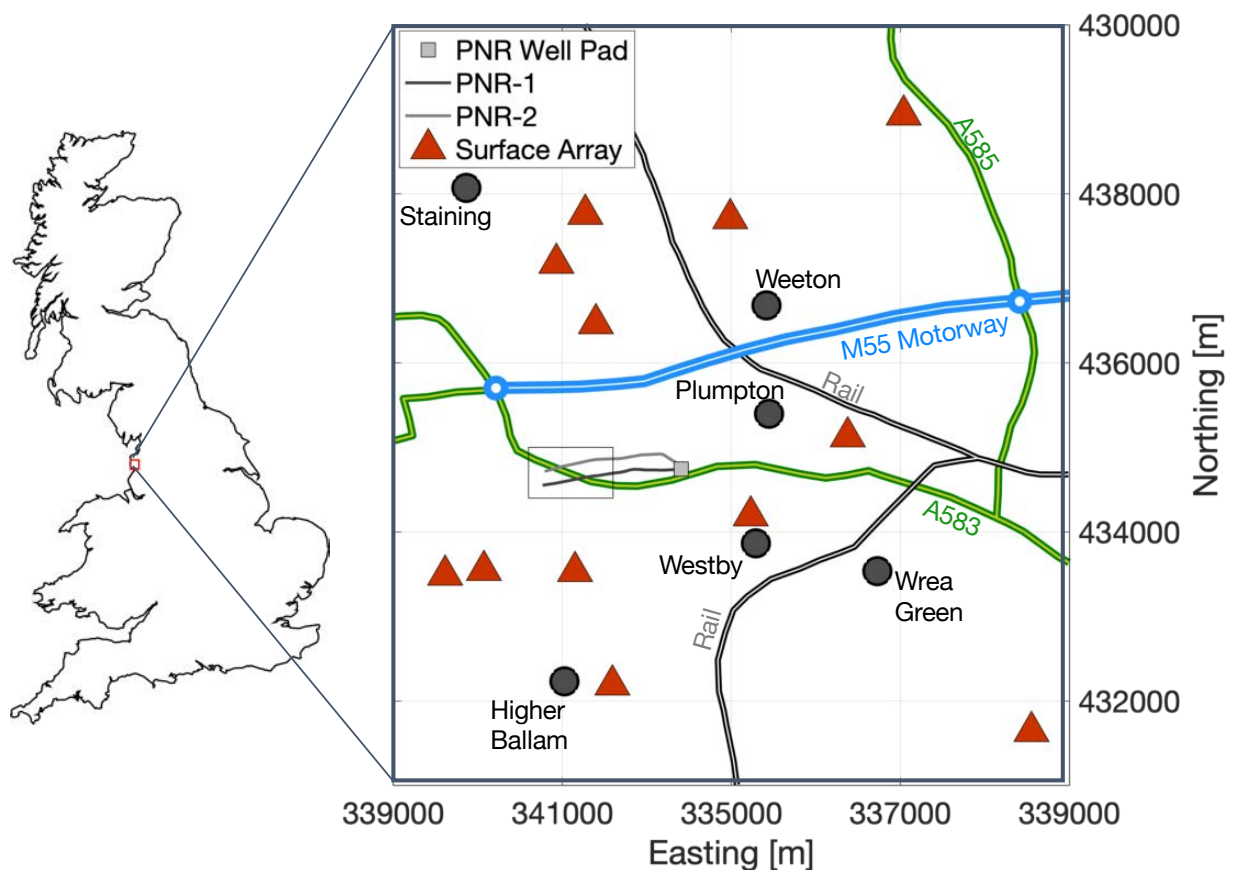


Figure 2.1: Map of the surface monitoring array for the PNR-1z well. Major road and rail links, and nearby villages are marked. Adapted from Clarke et al. (2019).

## 2.2. DOWNHOLE ARRAY

Surface arrays are limited in their event detection capability by the relatively high levels of noise at the surface, and by the fact that they are separated from the events by over 2,000 m of rock. Geophones installed in boreholes near to the reservoir can therefore provide a significant improvement in event detection (e.g., Maxwell et al., 2010). The microseismicity at PNR was monitored by an array of 24 geophones placed in the build section (i.e., the section where the well deviates from vertical to horizontal) of the nearby PNR-2 well (Figure 2.2). This array reported over 39,000 events during real-time monitoring with a minimum magnitude of  $M_w = -3.0$ . The locations of all recorded microseismic events are shown in Figure 2.3. The proximity of the downhole array to the events also means that it provides more accurate event locations than the surface array.

In the following sections, we use the event locations provided by the downhole array for all events. We use the downhole event moment magnitudes for the majority of events that were not detected by the surface array, but use the local magnitudes provided by the surface array where available for the larger events, such that our report is consistent with the magnitudes reported by the BGS during real-time operations.

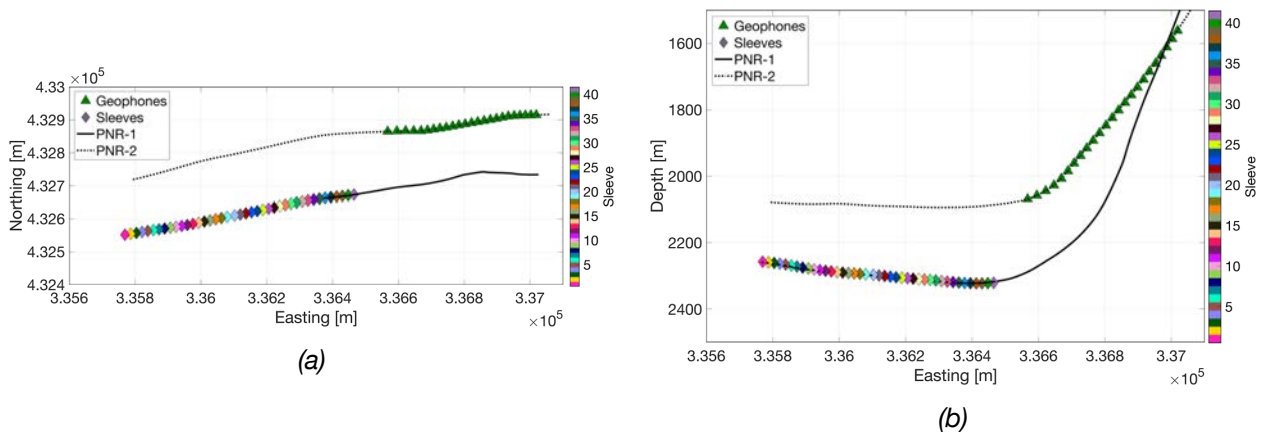


Figure 2.2: Map (a) and cross-section (b) showing the downhole microseismic monitoring array deployed in the PNR-2 well (green triangles) and the injection sleeves in the PNR-1z well (diamonds, coloured by sleeve number from toe to heel). Adapted from Clarke et al. (2019).

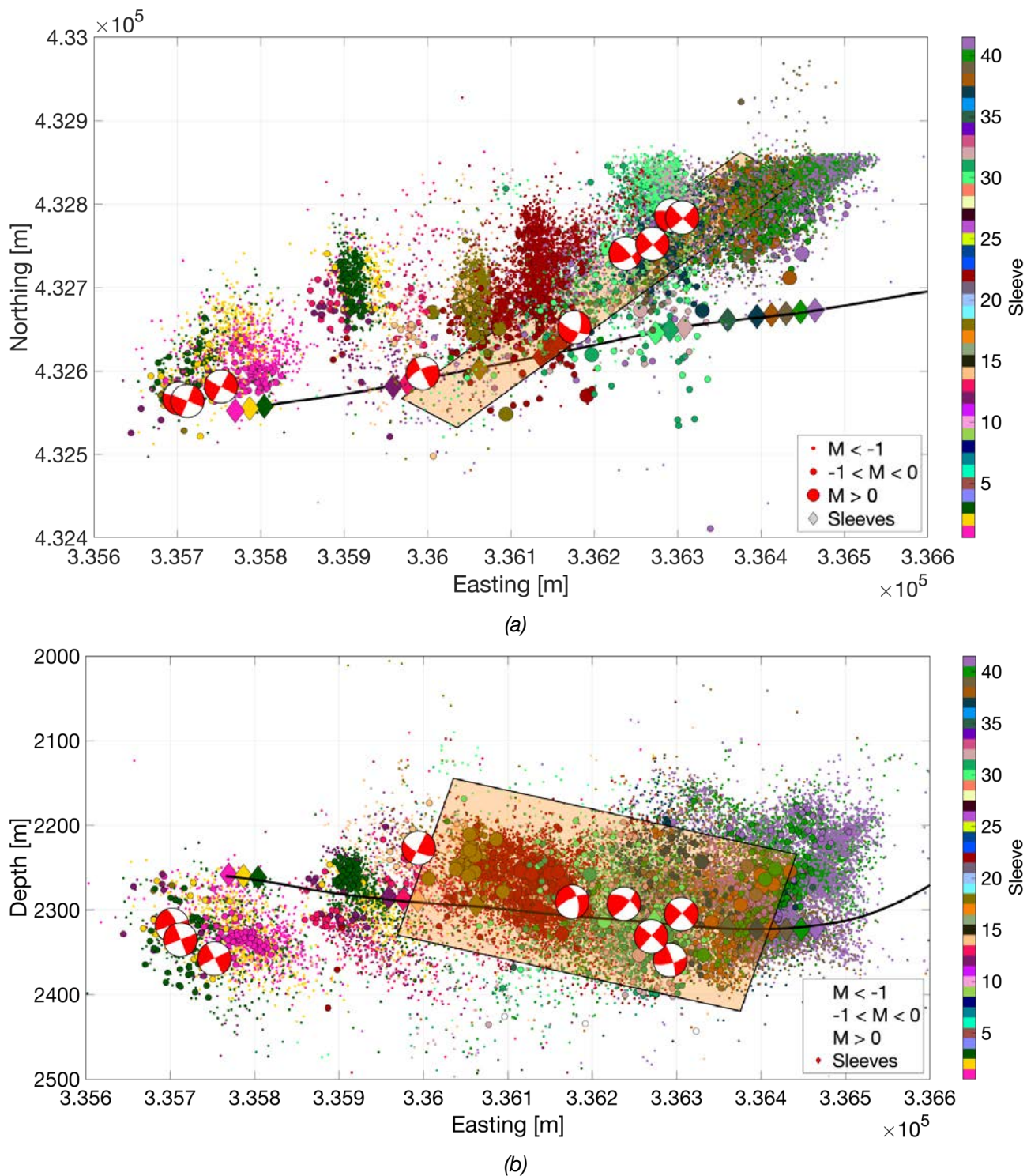


Figure 2.3: Map (a) and cross-section (b) of all events recorded during hydraulic fracturing on the PNR-1z well. Events are sized by magnitude and coloured by the sleeve with which they are associated. The focal mechanisms for some of the largest events are shown. Most of the large events occurred on a single plane, the position of which is marked by the orange box.

### 2.3. IDENTIFICATION OF PRE-EXISTING SEISMOGENIC STRUCTURES

The microseismicity occurs primarily to the north of the well, with “clouds” of events for each stage presumed to track the propagation of hydraulic fractures northwards from each sleeve. The cause for this northward propagation, as opposed to a symmetric distribution of fractures north and south of the well, is not clear. However, such asymmetry is not uncommon, and is typically ascribed to gradients of geomechanical parameters within the reservoir (e.g., Maxwell et al., 2011).

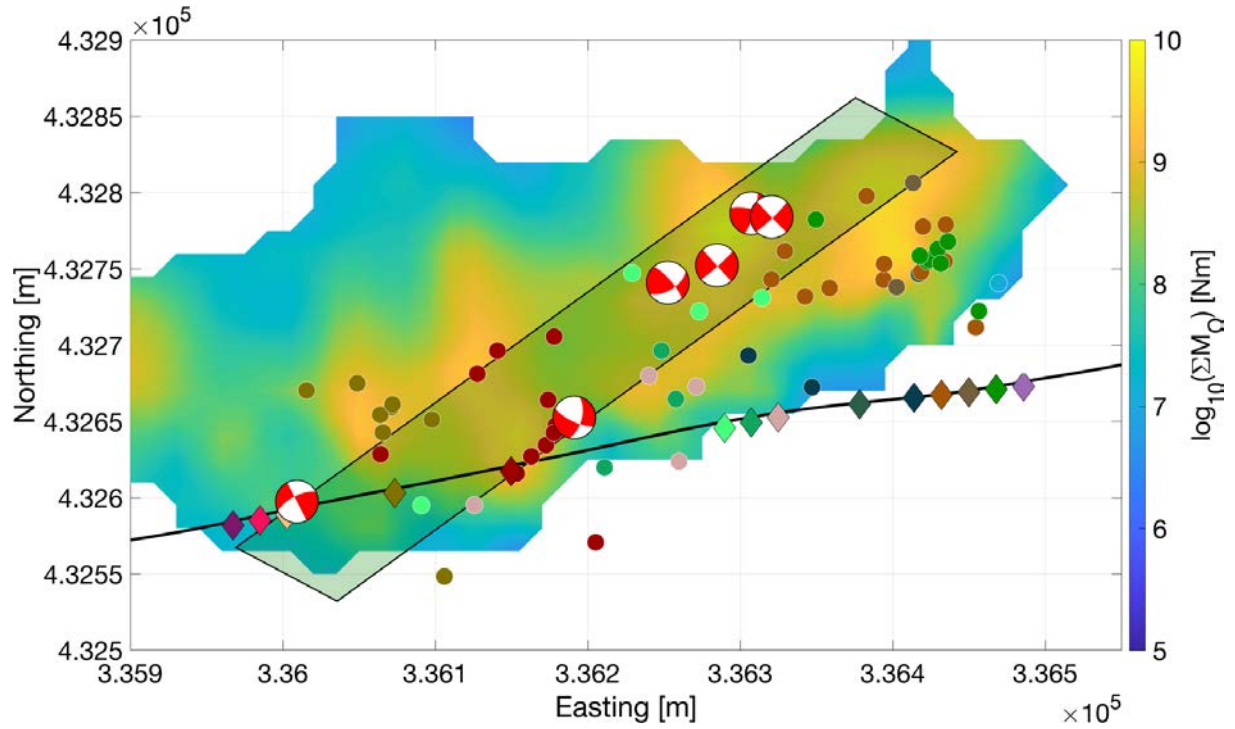
A key aspect for understanding induced seismicity is to identify pre-existing structures, such as faults or fracture zones, on which larger events may occur. In Figure 2.3 the events do not display an obvious alignment along a pre-existing fault, an observation which often provides the clearest evidence of fault reactivation (e.g., Igonin et al., 2019; Kettlety et al., 2019; Eyre et al., 2019). Instead, we use a combination of observations to identify and define the seismogenic structures responsible for the largest events.

### 2.4. FOCAL MECHANISMS

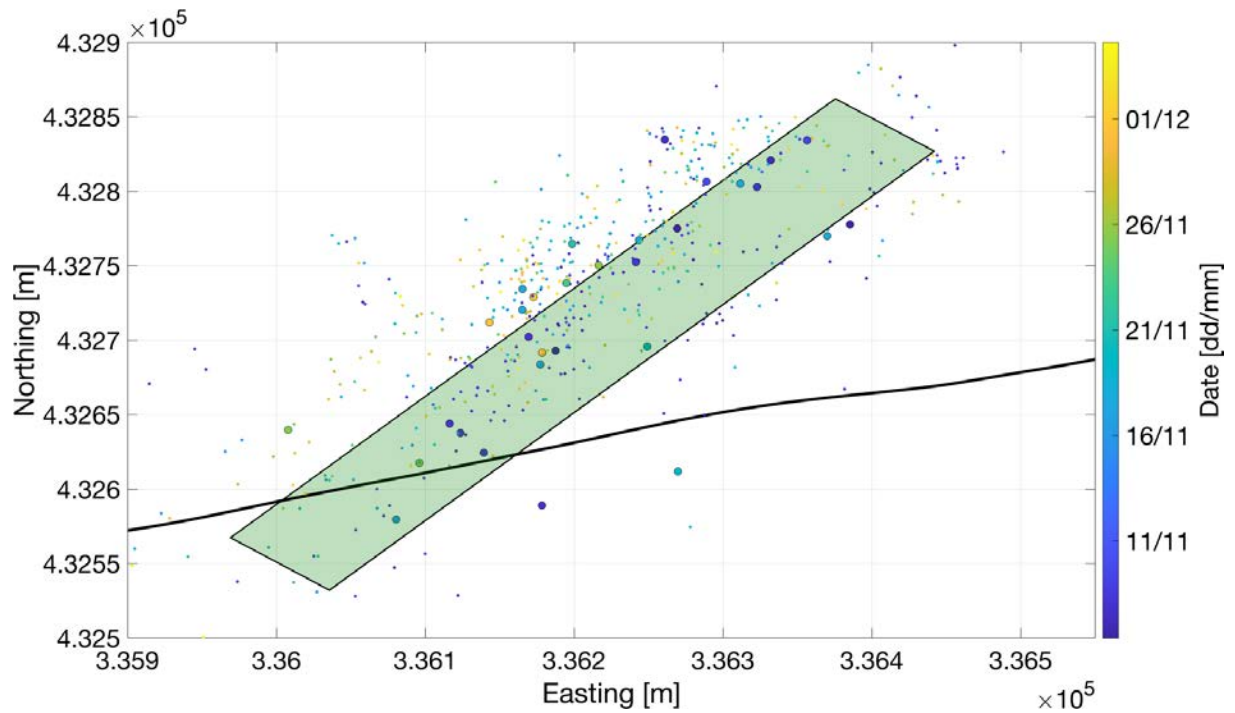
The focal mechanisms for 6 of the largest events are shown in Figure 2.4. The events all have similar mechanisms: either left-lateral strike slip on a near-vertical fault striking NE-SW, or right-lateral strike-slip on a near-vertical fault striking NW-SE. The consistent orientation of these focal mechanisms provides a constraint for the orientation of any potential seismogenic structure.

### 2.5. MAPPING LARGE EVENTS AND CUMULATIVE MOMENT RELEASE

Figure 2.4 also shows the positions of all events with  $M > 0$ , and maps the cumulative seismic moment release,  $\Sigma M_0$ . These observations allow us to identify a single zone in which almost all of the larger events occurred, and within which the overall cumulative seismic moment release was highest. This zone intersects the PNR-1z well at roughly the position of Sleeve 18, which was the first stage on which an event exceeding the  $M \geq 0.5$  TLS threshold occurred. Interaction between injection activities and this zone occurred along the well towards the heel. Importantly, the orientation of this zone matches the orientation of the NE-SW plane of the observed focal mechanisms.



(a)



(b)

Figure 2.4: Maps showing the observations used to identify seismogenic structures. (a) shows all events with  $M > 0$  (dots coloured by sleeve number as per Figure 2.3), the cumulative seismic moment (contours), and the focal mechanisms of the largest events. (b) shows a map of the events that occurred during the injection hiatus from 3<sup>rd</sup> November to 7<sup>th</sup> December. We combine the largest events and the injection hiatus events to map a plane striking at  $237^\circ$  and dipping at  $70^\circ$  (black-outlined box). Adapted from Clarke et al. (2019)

## 2.6. MICROSEISMICITY DURING INJECTION HIATUS

From the 3<sup>rd</sup> of November, CRL paused the injection program, initially in response to repeated  $M > 0.5$  events that had occurred during the previous week, and subsequently to address issues within the wellbore related to closing injection sleeves. The injection was paused until 7<sup>th</sup> December. Observations of microseismicity during this injection hiatus (Figure 2.4b) allowed the most definitive identification of a pre-existing seismogenic structure. The events during hiatus, almost all of which had magnitudes less than  $M < -1$ , were all located along the same feature that we had identified from the focal mechanism orientations, the positions of the largest events, and the cumulative moment release map.

Our overall interpretation of the observed microseismicity is that a pre-existing fracture zone or fault plane runs northeast from the well (as marked in Figures 2.3 and 2.4). During hydraulic stimulation, larger events occurred when the hydraulic fractures from each stage intersected this feature. During the hiatus, whereas the microseismic events associated with hydraulic fracturing stopped, low levels of microseismicity continued to persist along this feature for a longer period of time. We fit a plane to a combined population of the  $M > 0$  events (Figure 2.4a) and the hiatus events (Figure 2.4b), by finding the plane that minimises the least-squares distance between each event and the plane, finding a strike of  $237^\circ$  and a dip of  $70^\circ$ , which is consistent with the observed focal mechanisms. We term this fault NEF-1 (Northeast Fault-1) hereafter. We note that the largest event, with a magnitude of  $M = 1.5$ , could correspond to a rupture with displacement of less than 1 cm with a length less than 100 m. At this scale the distinction between a “small fault” and a “large fracture” is somewhat arbitrary: we will use “fault” hereafter to describe the NEF-1 feature, while keeping this fact in mind.

With the maximum and minimum horizontal stresses oriented approximately north-south and east-west respectively, this plane is well-oriented for the observed left-lateral strike slip motion, and the observed focal mechanisms are therefore consistent with the local stress conditions.

We note that this feature does not appear to be visible on the 3D reflection seismic data acquired by CRL prior to drilling PNR-1z. This is not uncommon for faults on which induced seismicity occurs (e.g., Kettlety et al., 2019; Igonin et al., 2019): if the reactivated faults are strike-slip, then detection using reflection seismic data can be challenging.

## 2.7. MICROSEISMIC OBSERVATIONS IN DETAIL

In Figures 2.5 – 2.11 we examine the evolution of the microseismicity in greater detail (maps for all stages are shown in Appendix I). Figure 2.5 shows the microseismicity during Stage 1. The northward growth of the hydraulic fractures is immediately apparent. In other respects, the microseismicity observed here is typical of most hydraulic fracturing data. However, we note the onset of a smaller cluster of events occurring approximately 100 m to the NE of the main microseismic cloud. Figure 2.6 shows the events that occurred during Stages 2 and 3. While these events are similar to those that occurred during Stage 1, the microseismicity in the cluster to the NE becomes even more pronounced. There are two competing hypotheses for the occurrence of these events: the presence of a pre-existing permeable connection that allows the rapid transfer of hydraulic pressure to this zone; or that the tensile fracture opening of Stages 1 – 3 produces deformation that generates positive  $\Delta CFS$  changes in the vicinity of the NE cluster.

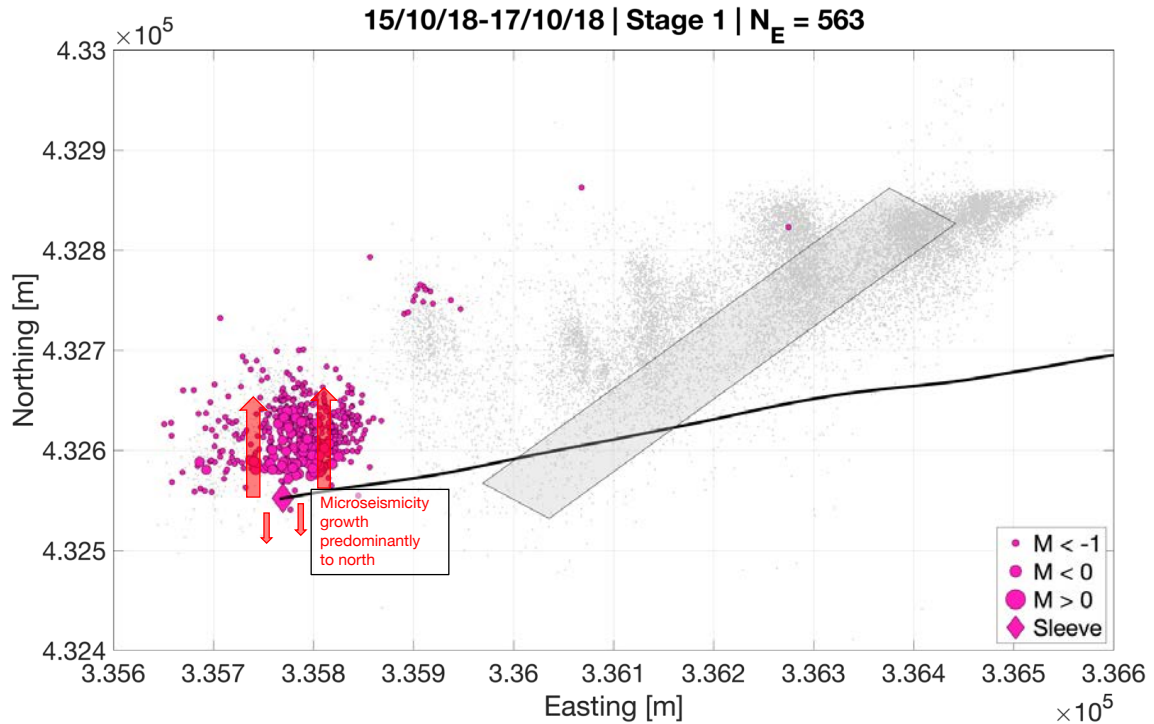


Figure 2.5: Map view of microseismic event locations during hydraulic stimulation of Sleeve 1. Coloured circles show Stage 1 events, scaled by magnitude. Grey dots show all recorded events, and the NEF-1 fault is also shown. The total number of events with signal-to-noise ratio greater than 5 is listed in the title. Most of the microseismicity is located to the north of the well, indicating preferential fracture growth in this direction.

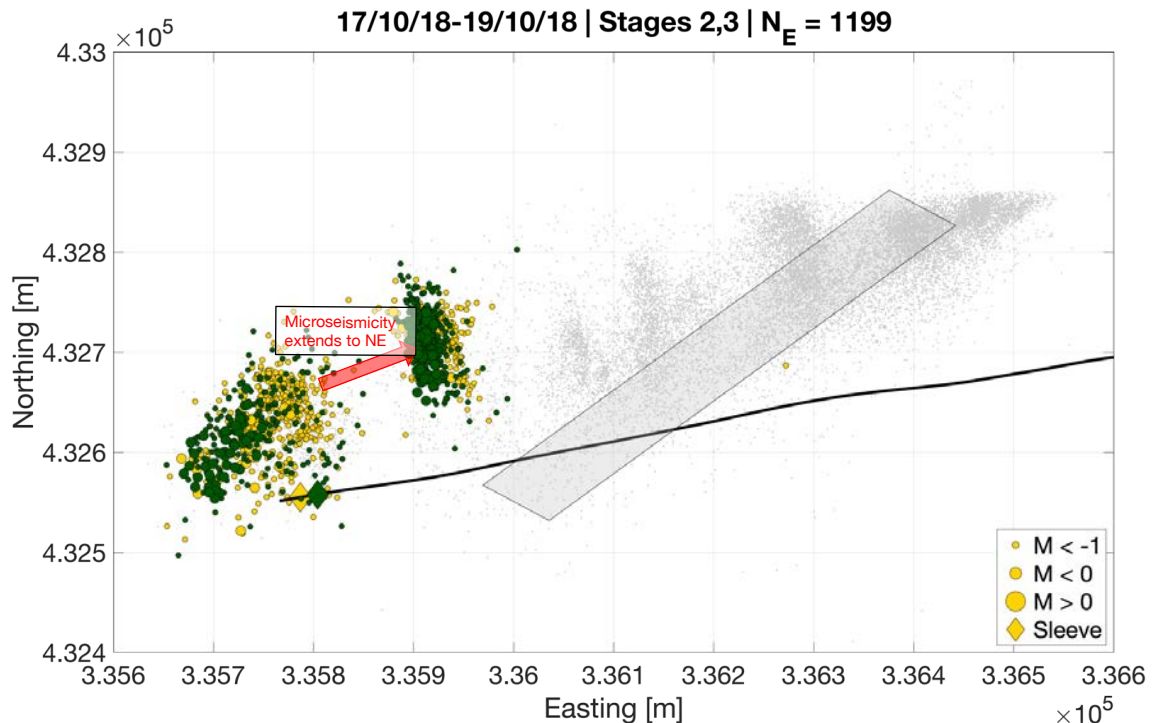


Figure 2.6: Map view of microseismic event locations during hydraulic stimulation of Stages 2 (yellow) and 3 (green). We note a cluster of microseismicity occurring to the NE of the main zone.

CRL then moved eastward along the well to stimulate Stages 12 and 13. The events associated with these stages are plotted in Figure 2.7. As with the previous stages, we observed microseismicity trending northwards from the well, tracking the propagation of hydraulic fractures. A small amount of microseismicity was located back towards the earlier stages – however this was of relatively small number, and represents primarily the tail-end of activity from Stages 1 – 3, as opposed to a re-initiation of microseismicity in this area.

The lack of microseismicity propagating back from Stages 12 and 13 to the loci of Stages 1 – 3 poses a question, given that during Stages 1 – 3 microseismicity was able to propagate to the loci of Stages 12 and 13. If a hydraulic pathway is responsible for the connection from Stages 1 – 3 to 12 and 13, then why does this connection only work in one direction, and not also allow microseismicity to propagate back to the west?

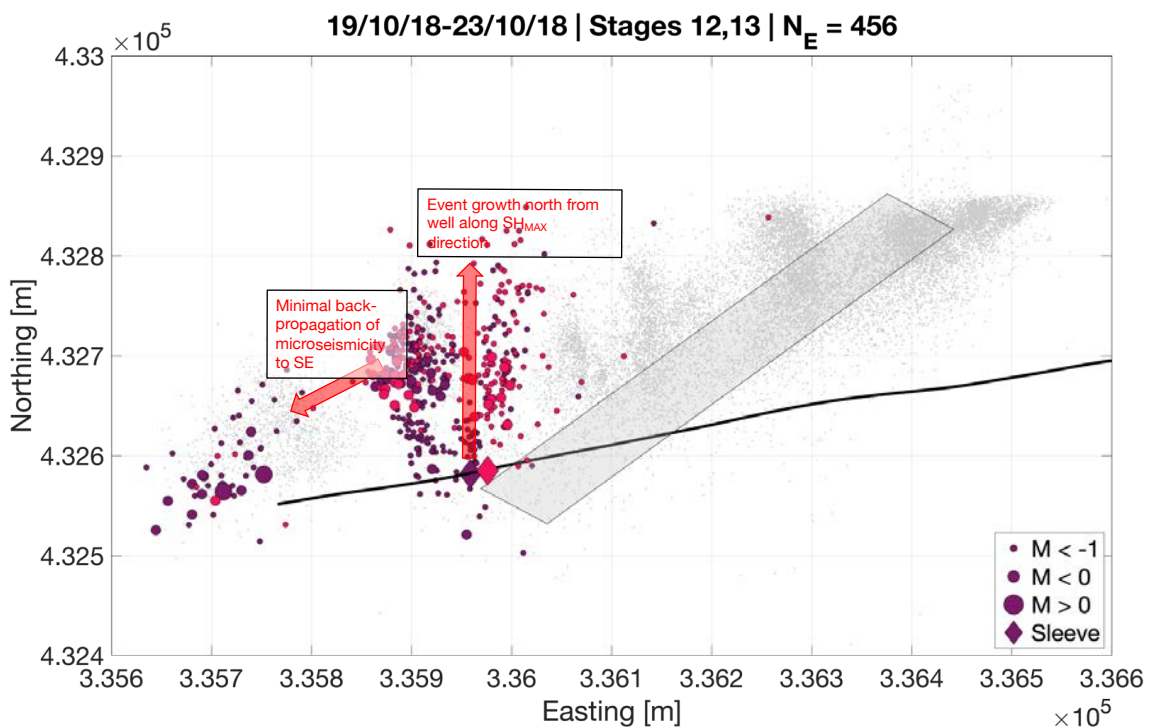


Figure 2.7: Map view of microseismic event locations during hydraulic stimulation of Stages 12 (purple) and 13 (pink). Most of the events track hydraulic fracture propagation north from the well. There is a minimal back-propagation of events to the SW.

The first stage to show clear evidence of fault reactivation was Stage 18 (Figure 2.8). This stage injected a very small fluid volume,  $< 10 \text{ m}^3$ , before it was halted by a red light TLS event. However, it was accompanied by a significant number of microseismic events – more than any of the preceding stages, extending  $> 150 \text{ m}$  northwards from the well. It is unusual for such small injection volumes to trigger an  $M = 0.5$  event, and it is unlikely that a  $10 \text{ m}^3$  injection volume would create a hydraulic fracture over  $150 \text{ m}$  long.

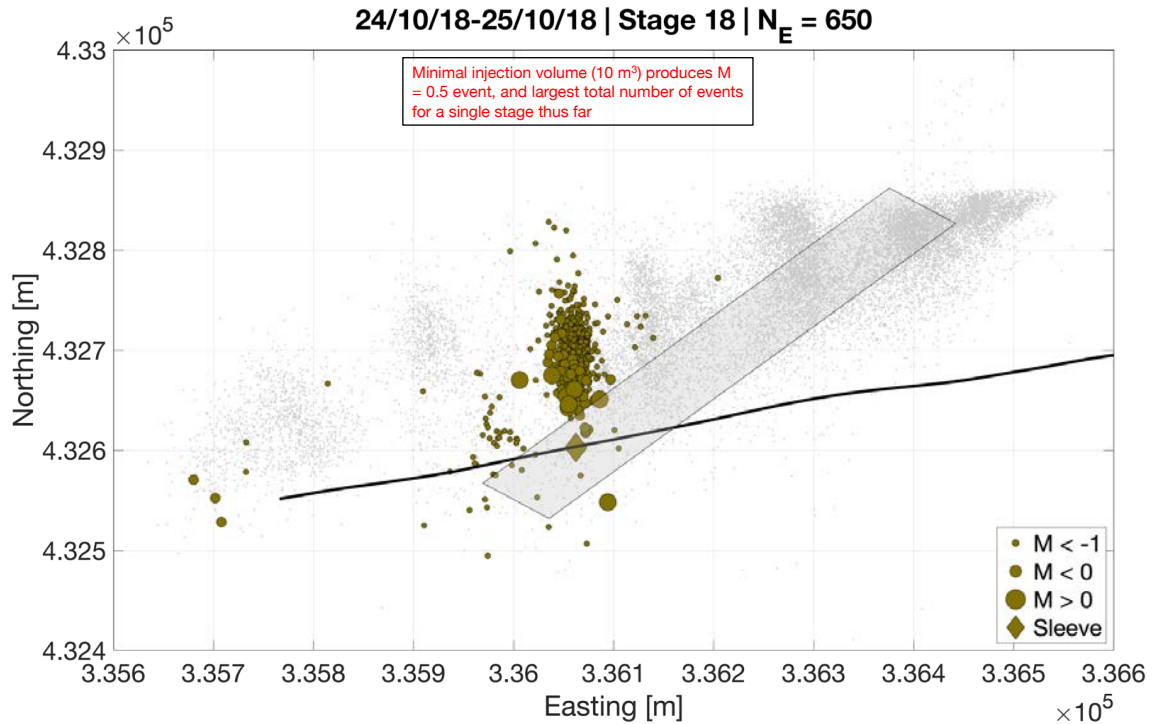


Figure 2.8: Map view of microseismic event locations during hydraulic stimulation of Stage 18. Only  $10 \text{ m}^3$  of fluid had been injected when an  $M = 0.5$  event resulted in a pause to injection. Despite the small injection volume, this stage had more microseismic events than any of the preceding ones.

Figure 2.9 shows the microseismic events during Stage 22, which is towards the western end of the NEF-1 fault. We notice two trends in the observed microseismicity: a cluster of events that extends northwards from the well, tracking the propagation of hydraulic fractures, and a second trend of events that crosses this northward cluster, extending to the NE along the NEF-1 fault.

Figure 2.10 shows the microseismic events during Stage 32, which is towards the middle of the NEF-1 fault. If microseismicity were driven purely by elevated pore fluid pressure from the well, then we would expect the highest levels of microseismicity to occur near to the well, and decreasing with distance because pore pressure perturbations will be smaller at greater distances from the well. Instead, we observe a “gap” in events between the injection sleeve at the well, with the main focus of the microseismicity located 100 – 200 m north of the well.

Unlike Stage 22 (Figure 2.9), we do not observe propagation of microseismicity to the NE or SW along the NEF-1 fault. There is some microseismicity to the SW – this represents continued activity in the area from earlier stages, and does not represent re-initiation of microseismicity in this region. Indeed, low levels of microseismicity persist along NEF-1 throughout the injection hiatus period in November 2018 (Figure 2.4). However, the lack of propagation of significant amounts of microseismicity along the NEF-1 fault, especially back towards the west, is common to all the later stages that intersected this feature.

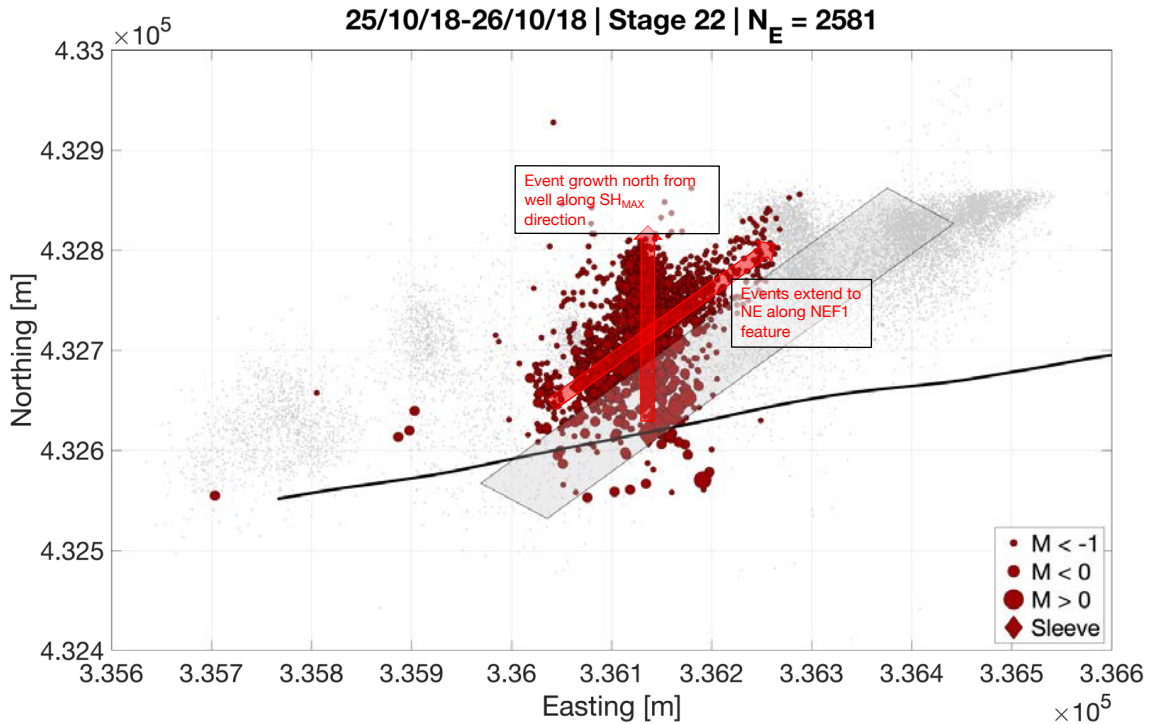


Figure 2.9: Map view of microseismic event locations during hydraulic stimulation of Stage 22. Two event trends are identified: events propagating northwards from the well, tracking the expected hydraulic fracture growth, and events propagating to the NE, following the NEF-1 fault.

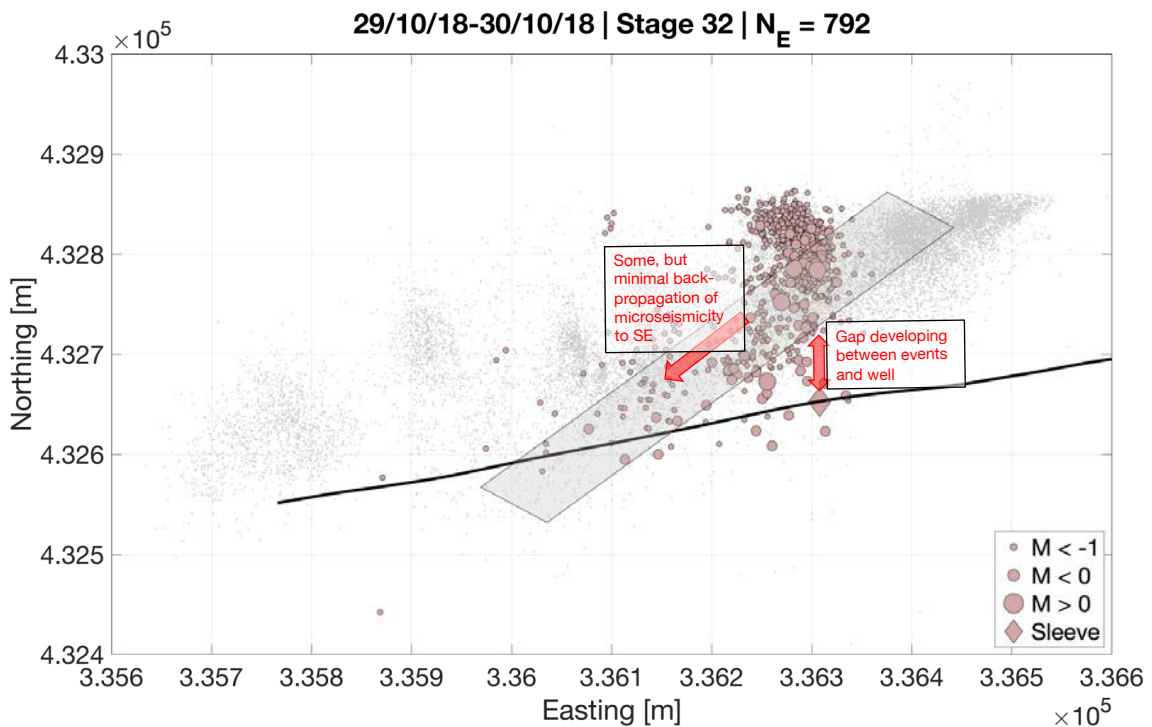


Figure 2.10: Map view of microseismic event locations during hydraulic stimulation of Sleeve 32. We observe a gap between the injection point at the well and the main focus of microseismicity roughly 100 m to the north. We do not observe significant numbers of microseismic events propagating back to the west along the NEF-1 fault.

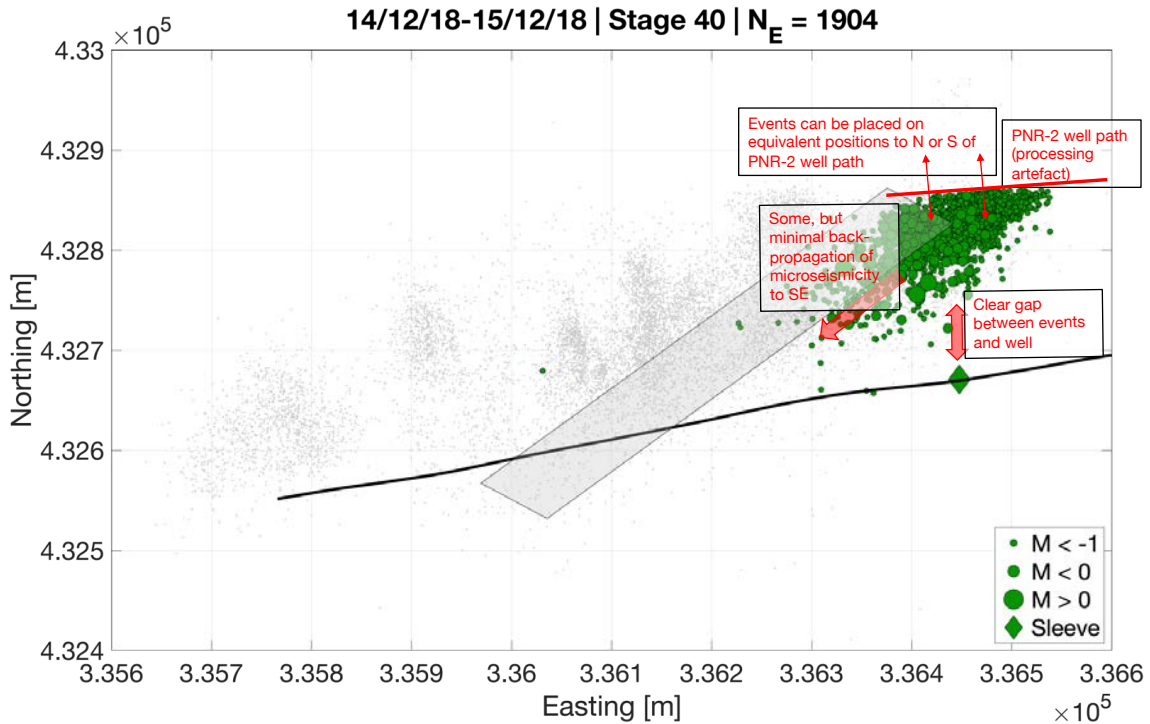


Figure 2.11: Map view of microseismic event locations during hydraulic stimulation of Stage 40. These events show a processing artefact that places all events to the south of the PNR-2 well path, when in reality some of these events will have occurred further north. We again observe a gap between the injection point on the well and the main focus of microseismicity roughly 100 m to the north, and do not observe significant numbers of microseismic events propagating back to the west along the NEF-1 fault.

Figure 2.11 shows microseismic events from Stage 40. The heel-most stages (39 – 41) show a location artefact produced by the geometry of the monitoring array (Figure 2.2). When locating microseismic events with a single downhole array, a fundamental ambiguity of  $180^\circ$  is produced by the use of particle motion to constrain the back-azimuth of the event from the array (e.g., Jones et al., 2010). Because the monitoring array is placed at an oblique angle in the build section of PNR-2, the resulting spatial ambiguity means that events at the heel of the well could be placed in equivalent positions to the north or south of the well. The processing contractor has resolved this ambiguity by placing all of the heel-most stage events to the south of the PNR-2 well path, creating a sharp east-west trending “edge” to the microseismicity cloud. This is a processing artefact, and in reality some of this microseismicity will propagate further to the north underneath the PNR-2 well path (which is 200 m shallower than the PNR-1z well).

As identified for Stage 32 (Figure 2.10), there is a clear gap between the injection point on the well and the focus of the microseismicity roughly 100 m further north. This gap becomes more pronounced for the later stages. We also note the lack of microseismicity back-propagating along the NEF-1 feature to the southwest.

The observations presented above pose a series of questions that are difficult to answer if the microseismic hypocentres are to be explained purely in terms of diffusion of elevated pressures emanating from the well:

- Why do some stages (Stages 2 and 3, Stage 22) show migration of microseismicity to the NE of the northward-propagating hydraulic fractures, but later stages (e.g., Stages 12 and

13, Stages 30 – 32) do not have a corresponding migration of microseismicity back to the southwest along the same pathways? If pressure transfer along a permeable pathway is to be invoked as a causative mechanism, why is this hydraulic connection not able to function in both directions?

- Why does Stage 18 generate such high rates of microseismicity, at distances of up to 150 m from the well, with only 10 m<sup>3</sup> of fluid injected?
- Why is there a gap between the well and the observed microseismicity for the heel-most stages, whereas we would expect pore pressure increases, and therefore microseismicity, to be highest near to the well?

These problems suggest that an alternative mechanism may be playing a significant role in triggering the microseismicity observed during hydraulic fracturing of PNR-1z.

## 2.8. SPATIO-TEMPORAL EVOLUTION OF MICROSEISMICITY

The evolution of microseismic event distances (from the injection point) with time can reveal the underlying physical mechanisms that are causing the events (e.g., Shapiro et al., 2006). Shapiro et al. (1997) show that, if microseismicity is driven by pore pressure diffusion from the well, then for constant-rate injection a triggering front should develop that extends in distance,  $r$ , from the injection point as a function of time  $t$ :

$$r = \sqrt{4\pi Dt}, \quad (3)$$

where  $D$  is the hydraulic diffusivity. The diffusive case can be contrasted with the case of hydraulic fracture propagation where, assuming minimal leak-off of fracturing fluid, the length of hydraulic fracture propagation might be expected to show a linear time-distance relationship, since the length of a hydraulic fracture  $L$  scales with the injection rate  $Q$ , the height  $h_f$  and width  $w_f$  of the hydraulic fracture (Economides and Nolte, 2003; Shapiro et al., 2006):

$$L = \frac{Qt}{2h_f w_f} \quad (4)$$

Figure 2.12 shows examples of  $r$  vs  $t$  behaviour for several stages ( $r$  vs  $t$  plots for all stages are shown in Appendix II). We overlay curves produced by Equation (3) using different values of  $D$ , and by Equation (4), assuming arbitrary values of  $h_f = 25$  m and  $w_f = 2.5$  mm (see Chapter 3 for a more detailed evaluation of expected hydraulic fracture dimensions).

In Figure 2.12 we do not see the  $r \propto t^{1/2}$  behaviour that is characteristic of a pore pressure diffusion-controlled triggering process (Equation 3). We instead see microseismicity occurring near-instantaneously across different distances from the injection point. The behaviour is somewhat consistent with the linear relationship between  $r$  and  $t$  given by Equation (4). For a typical flow rate of 0.07 m<sup>3</sup>/s, we might expect a hydraulic fracture to propagate a distance of 300 m in less than 10 minutes. This is, however, an upper bound because Equation (4) assumes no leak-off of fluid into the formation, and also because in reality we would expect multiple hydraulic fractures to form from an injection sleeve, sharing the fluid volume between them.

These observations, and the observations presented in Section 2.7, motivate us to evaluate the potential role played by the transfer of stress associated with tensile opening of hydraulic fractures as a triggering mechanism for the microseismicity.

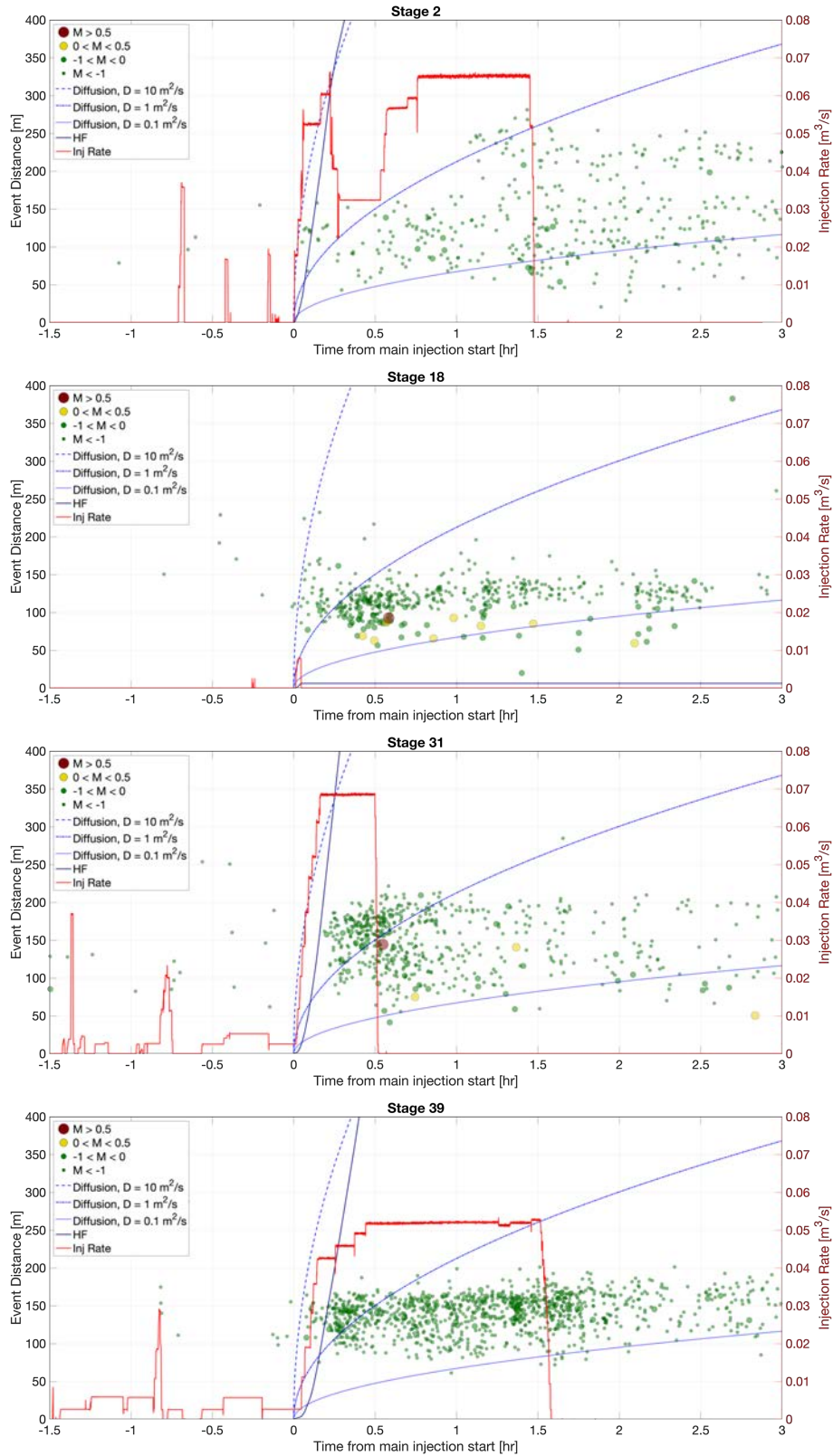


Figure 2.12: Distance of microseismic events (dots) from the injection point as a function of time, for each injection stage. The time-distance behaviour can reveal the underlying triggering cause. We also show the injection rate (red line), and the expected time-distance behaviour produced by diffusion models with  $D = 0.1, 1$  and  $10 \text{ m}^2/\text{s}$  (blue dashed lines), and a hydraulic fracture model assuming  $h_f = 25 \text{ m}$ ,  $w_f = 2.5 \text{ mm}$  and no fluid loss (black line).

## 2.9. COMMENTS ON MICROSEISMIC EVENT LOCATION ACCURACY

The microseismic events occur to the north of the well. As described above, our preferred interpretation is that this represents asymmetric fracture growth, with most of the hydraulic fractures propagating northwards. This is not uncommon, and is typically driven by gradients in material properties and/or stress, which create a preferred direction for fracture propagation (e.g., Maxwell et al., 2011).

However, an alternative explanation is that this is an artefact produced by mis-location of the events. It is beyond the scope of this study to perform wholesale re-analysis of the microseismic event locations. However, simple assumptions about the event location accuracies can be tested based on standard microseismic event location procedures.

To locate microseismicity using a single vertical geophone array, several observations are combined (Figure 2.13). The distance between the event and the array, and the depth of the event, are determined by the differences in arrival times between P- and S-waves across the array (the “moveout”), using an assumed velocity model. The azimuth of the event from the array is determined using a hodogram analysis of the particle motion of the P-wave, which is parallel to the direction of ray propagation.

For the depths and radial distances of the events, they occur at similar depths to the well (Figure 2.3b), and at similar positions along the well relative to their respective stages. This indicates that the locations are accurate with respect to these parameters, and that no systematic error has been introduced by the estimation of moveout across the array, or by the choice of velocity model.

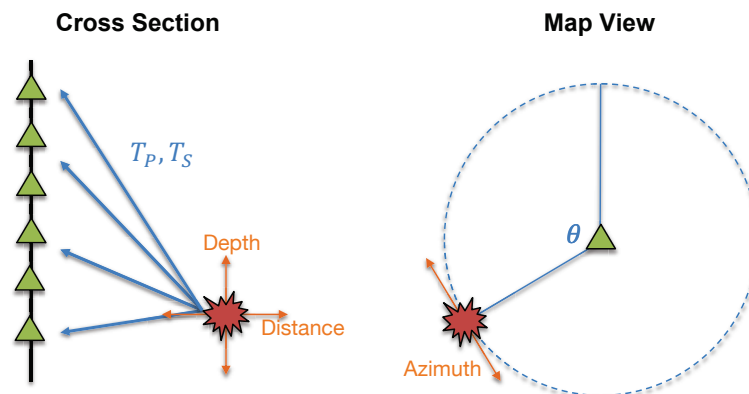
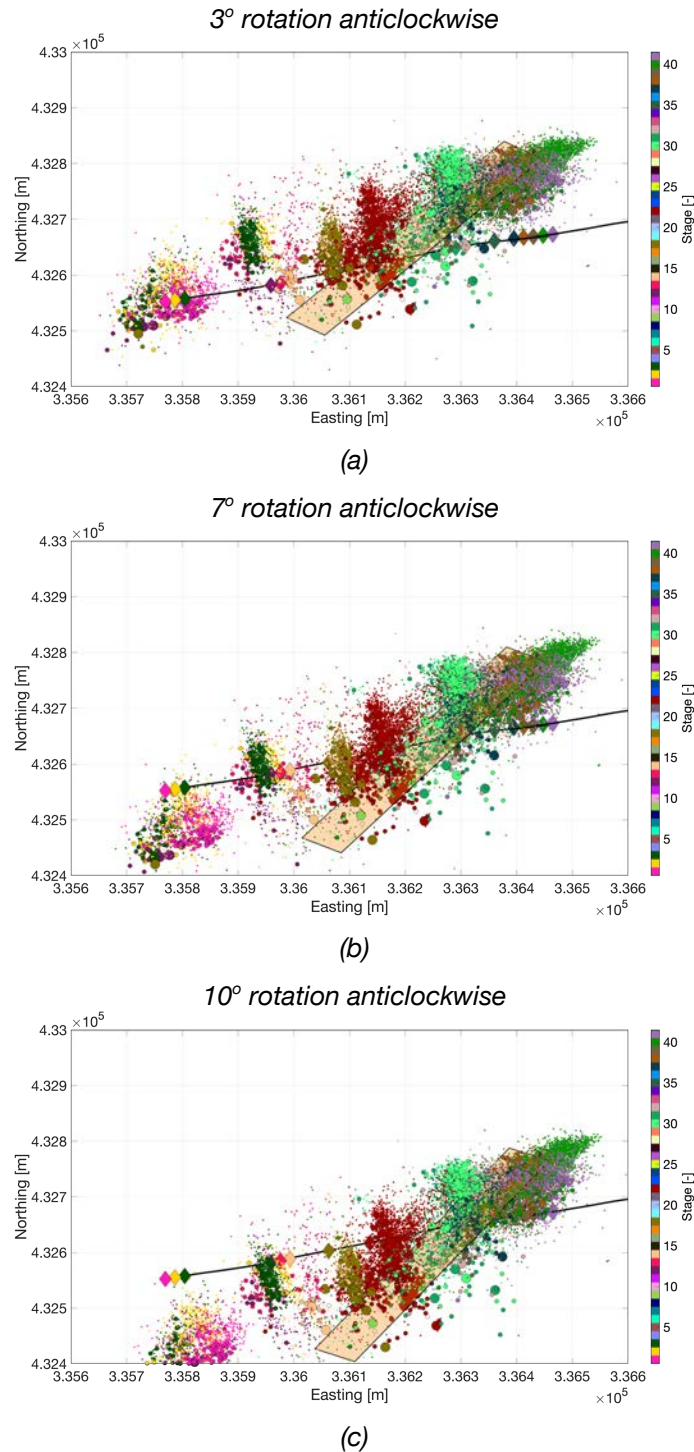


Figure 2.13: Schematic showing how microseismic events are located using a single downhole microseismic array. The depth of the event, and its radial distance from the array, are determined by the differential arrival times of P- and S-waves on each station (the “moveout”). The direction of the event from the array is determined from hodogram analysis of the P-wave particle motion, which will be parallel to the direction of ray propagation.

The hodogram analysis determines the azimuth of the event from the monitoring array. This analysis presumes that the orientations of the 3 geophone components are well-constrained, with the constraint typically provided by the location of check-shots from known positions. For PNR-1, “jarring” of the sleeves was used to create acoustic emissions to determine the orientation of the array. The procedure was repeated several times to ensure a robust measurement. Nevertheless,

it is possible that a systematic mis-orientation of the geophones could then produce a mis-location of the events.



*Figure 2.14: Impact of geophone mis-orientation on microseismic event locations. We plot event locations rotated anticlockwise about the mid-point of the monitoring array by 3° (a), 7° (b), and 10° (c). In (a), the events at the toe of the well now straddle it, but events at the middle and heel of the well are still to the north of it. In (b) the events at the middle of the well straddle it, but events at the toe are to the south and events at the heel are to the north. In (c) the events at the heel straddle the well, but events at the toe are significantly to the south.*

A mis-orientation of the geophones would produce a lateral rotation of the event locations around the mid-point of the array. In Figure 2.14 we show the impact of such a rotation on the event locations, rotating the events by  $3^\circ$ ,  $7^\circ$ , and  $10^\circ$ . These angles are chosen such that events at the toe, the middle, and the heel will be positioned to straddle the well. In Figure 2.14a the events at the toe of the well now straddle it, however the events at the middle and heel of the well are still predominantly to the north of it. In Figure 2.14b, the events at the middle of the well now straddle it, but the events at the toe are now to the south of the well, while events at the heel are still to the north of it. In Figure 2.14c, events at the toe of the well are now a significant distance to the south.

Overall, the impact of a geophone mis-orientation is to rotate all the events by a consistent angle around the array. Therefore, there is no single rotation that can place events both at the heel and at the toe of the well to straddle the well. Indeed, applying a rotation of the type shown in Figure 2.14 would imply that hydraulic fractures at the heel of the well propagate northwards and at the toe of the well propagate southwards. This is harder to explain with respect to geomechanics, as it would imply different gradients in geomechanical properties or stress conditions along the well. Instead, our preferred interpretation is that the event locations are accurate, and that the predominantly-northward propagation of hydraulics fractures is caused by a consistent south-to-north gradient in geomechanical conditions.

### 3. DEFORMATION AND STRESS TRANSFER

In this chapter we assess whether the deformation produced in the surrounding rock frame by tensile opening of hydraulic fractures could provide an alternative explanation for the observed microseismicity at PNR-1z. We use analytical solutions to calculate the deformation produced by fractures undergoing tensile opening (Okada, 1992) using the PSCMP code developed by Wang et al. (2006). We compare observed microseismic event locations with areas that are predicted to receive positive  $\Delta CFS$  changes from the modelled deformation. A strong correlation between event locations and positive  $\Delta CFS$  changes would indicate that stress transfer effects are playing a dominant role in controlling when and where the microseismicity takes place.

#### 3.1. MODELLING HYDRAULIC FRACTURES

As the input, or loading, for our stress-transfer simulations, we require models that describe the number of hydraulically-stimulated fractures, their dimensions, and the amount of fracture opening that takes place. This can be done using coupled hydro-mechanical fracture simulation codes (e.g., Warpinski et al., 1994; Profit et al., 2016). However, results from such models are highly dependent on geomechanical input parameters that may not be well constrained, and these models are commonly tuned specifically to match microseismic observations. Modelling of this kind is beyond the scope of this study, since our objective is not to model hydraulic fracture propagation itself, but to model the impacts of the hydraulic fracturing on the surrounding rock mass. Instead, we adopt a stochastic approach, generating populations of tensile-opening fractures by drawing their properties (dimensions, positions, orientations, etc.) from statistical distributions representing typical hydraulic fracturing cases. The use of a stochastic approach allows us to create thousands of model instantiations, such that we can identify features in the resulting deformation that are consistent across a range of input hydraulic fracture models, and so may be considered robust and not dependent on a single choice of model parametrisation.

The statistical distributions we use to parameterise our fracture models are described below:

- **Fracture positions:** the lateral and vertical positions of the fractures are assumed to be normally distributed, centred on the position of the sleeve, with a standard deviation of 25 m.
- **Fracture orientation:** the fractures are modelled as uniformly-opening vertical rectangular patches. Fracture strikes are sampled from a Von Mises distribution with an average of  $170^\circ$ , matching the local maximum horizontal stress direction, with a standard deviation of  $10^\circ$ .
- **Fracture propagation direction:** Based on observations of the microseismic event cloud, we place 80% of fractures to the north from the well, and 20% to the south.
- **Fracture lengths:** The fracture lengths are normally distributed, with a mean of 25 m and a standard deviation of 50 m. The maximum allowed length is 250 m, and the minimum is 15 m. At least one fracture must extend to the same distance from the well as the microseismic cloud observed for each well.

- **Fracture aspect ratio:** All fractures have a fixed aspect ratio of 0.2 (fracture height/fracture length).
- **Fracture opening width:** Each fracture is assumed to open in a purely tensile manner with no shear component. To constrain the approximate width of each fracture, we use the analytical solutions for fracture width for a given injection pressure (Figure 3.1), frequently employed in fracture modelling for the opening of a Griffith crack (Perkins and Kern, 1961). For the injection rates at PNR ( $0.07 \text{ m}^3\text{s}^{-1}$ ), a shear modulus of 25 GPa, a Poisson's ratio of 0.25, and a fracture aspect ratio of 0.2, the fracture width from this analytical solution would be around 2.1 mm. This value for width is then used to find the total number of fractures, by dividing the total volume injected by the volume contained within the average 75 m long fracture. This is likely to be an overestimate of the total amount of fracturing, since some fluid will inevitably leak-off into the formation rather than contribute to fracture opening (Perkins and Kern, 1961; Nordgren, 1972). Fracture width within the model itself is then defined as the total volume of fluid injected divided by the total area of all stochastically generated fractures. This gives widths very similar to that found using the solutions of Perkins & Kern (1961) with normally distributed values of  $2.6 \pm 0.3 \text{ mm}$  for each set of fractures.

This approach yields fracture networks such as those depicted in Figure 3.1. In the following section we describe how we use the opening of these simulated fracture networks as the loading for our geomechanical model.

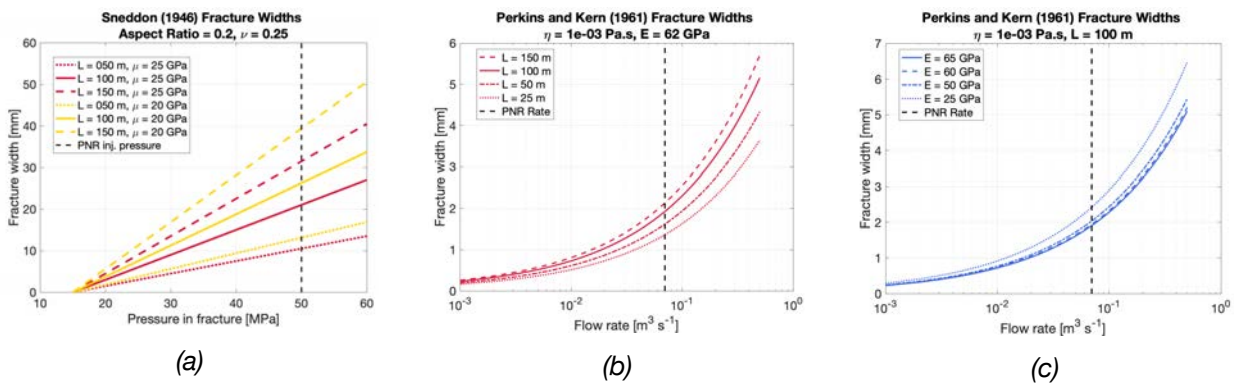


Figure 3.1: Impact of pressure and flow-rate on hydraulic fracture width, based on the models of Sneddon (1946) and Perkins and Kern (1961). For conditions at PNR-1, a fracture width of 2 – 3 mm is reasonable.

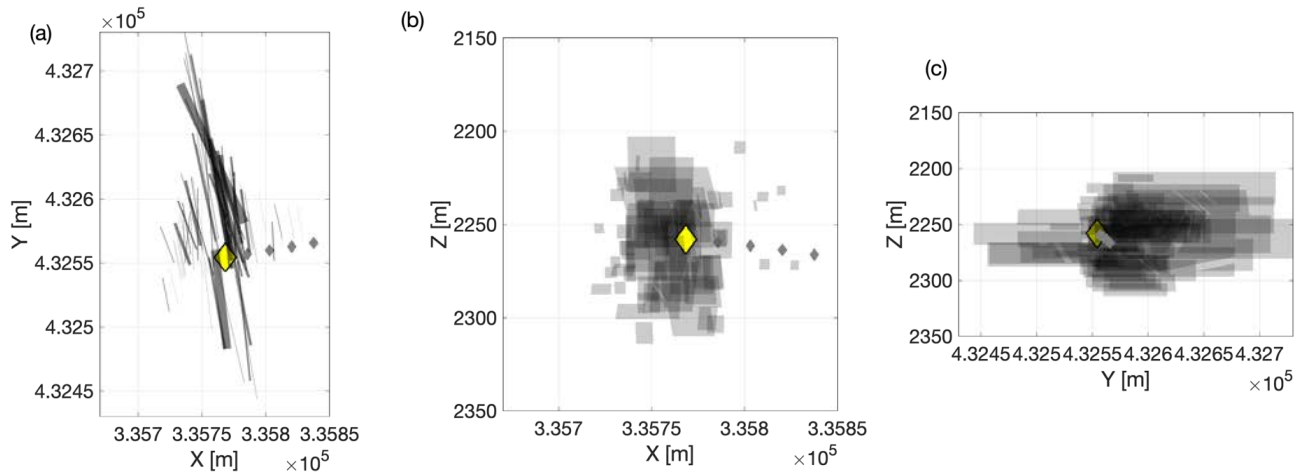


Figure 3.2: Example hydraulic fracture models generated by our stochastic approach (for Stage 1 in this case), shown in map (a) and cross-section (b and c) view.

### 3.2. MODELLING STRESS CHANGE

For a given set of tensile fractures, we use the PSCMP code (Wang et al., 2006) to compute the deformation in the surrounding rocks. Figure 3.3 shows an example of stress transfer produced by a single tensile fracture, and how these can be resolved onto a plane with a specific orientation to compute the  $\Delta CFS$  change. We use Young's modulus  $E = 62.5$  GPa, shear modulus  $G = 25$  GPa, Skempton's coefficient  $\beta = 0.4$ , and friction coefficient  $\phi = 0.7$ . We resolve the modelled stress changes into  $\Delta CFS$  acting on receivers that have strike of  $240^\circ$  and dip of  $70^\circ$ , matching the NEF-1 fault described above, and a rake of  $0^\circ$ , corresponding to left-lateral strike-slip as observed for the focal mechanisms of most of the larger events (Figure 2.4). We compute the  $\Delta CFS$  changes in 3D around the PNR-1z well (e.g., Figure 3.4).

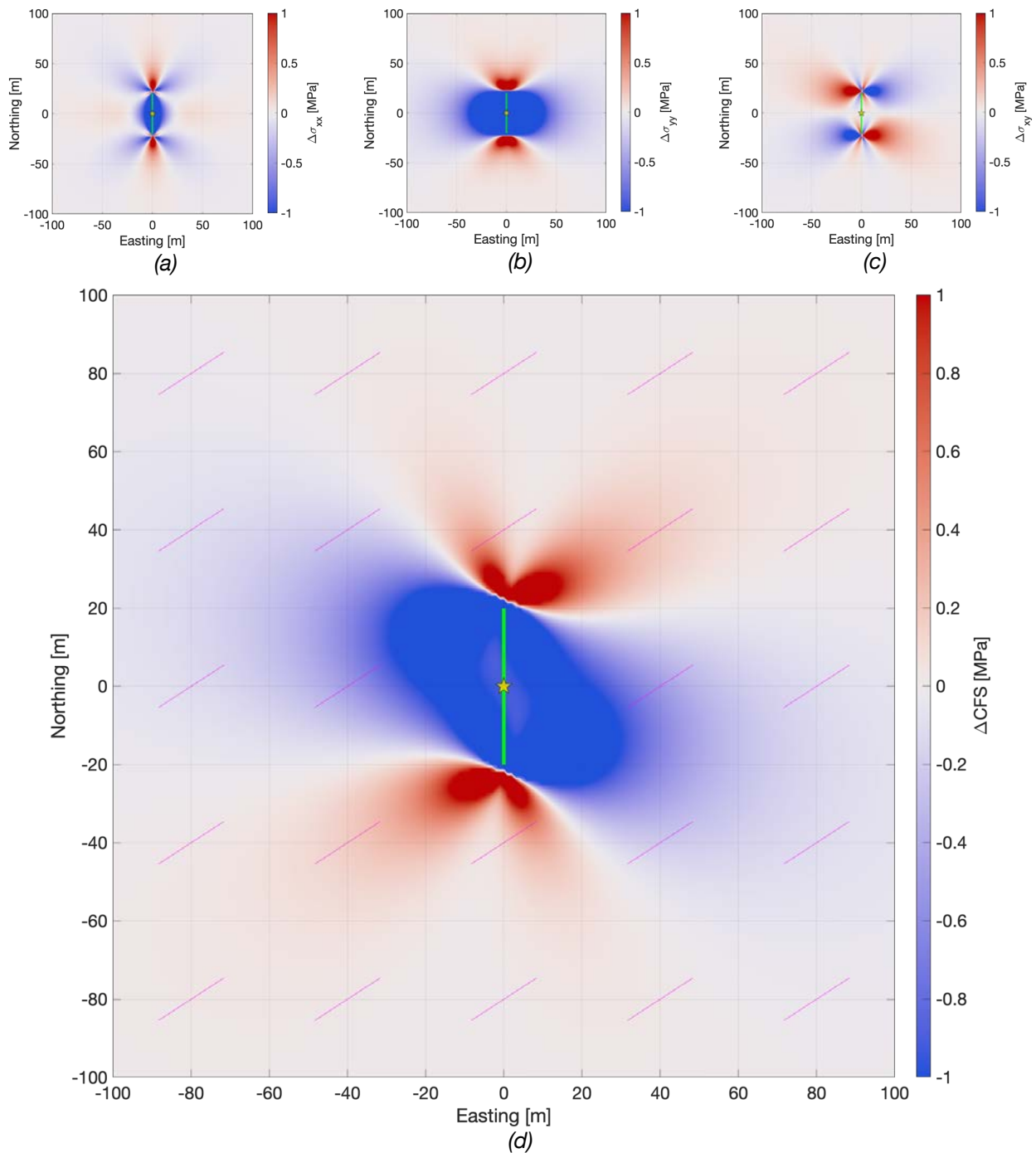


Figure 3.3: Modelling approach to compute  $\Delta\text{CFS}$ : Here we show the changes to stress tensor components  $\sigma_{xx}$  (a),  $\sigma_{yy}$  (b) and  $\sigma_{xy}$  (c) caused by a single tensile fracture with length and height = 40 m (green line) opening by 3 mm. In (d) we resolve these stress changes into  $\Delta\text{CFS}$  acting on fractures with a strike of  $237^\circ$  and dip of  $70^\circ$  (purple lines), assuming a rake of  $0^\circ$  (left-lateral strike slip motion). Positive  $\Delta\text{CFS}$  (red “lobes”) indicate areas where the deformation would promote slip on fractures that had this orientation.

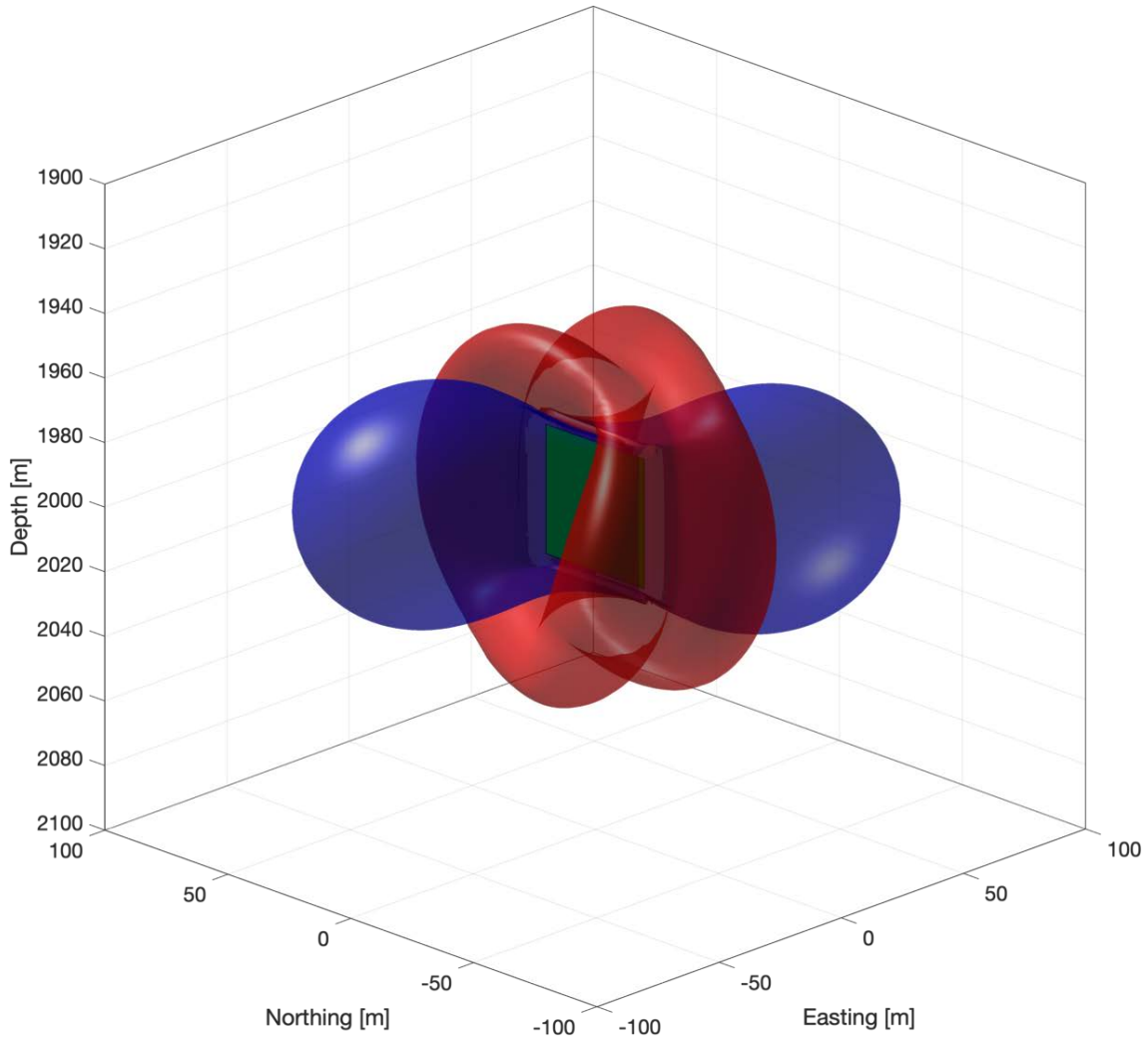


Figure 3.4: 3D view of  $\Delta CFS$  positive and negative “lobes”, in this case produced by a 20 m x 20 m fracture (green square) opening by 3 mm, resolved onto on fractures with a strike of 237°, dip of 70°, and rake of 0°. The lobes are drawn at the  $\Delta CFS = +0.1$  MPa (red) and  $\Delta CFS = -0.1$  MPa (blue) isobars. For this particular geometry of fractures, positive  $\Delta CFS$  is generally found near the fracture tips, and negative  $\Delta CFS$  is generally found in regions adjacent to the fracture faces.

To avoid overinterpretation of artefacts that may be unique to one particular stochastic instantiation, for each stage we generate 1,000 repeated model iterations derived from the statistical distributions outlined in Section 3.1, and for each point in the subsurface we take the median  $\Delta CFS$  change calculated from all of the models. This removes outliers that are the product of a single stochastic instantiation and identifies stress changes that are consistent across the statistical distributions of input parameters described in Section 3.1, and therefore can be considered robust.

Figure 3.5 shows an example result for a single stage, showing the regions of the subsurface where tensile fracture opening has caused positive  $\Delta CFS$  (red lobes), where fault slip would be promoted, and where it has caused negative  $\Delta CFS$  (blue lobes), where fault slip would be discouraged. Lobes of positive  $\Delta CFS$  extend north and south of the hydraulic fracture tips, as well as above and below, while negative lobes extend east and west perpendicular to the fracture faces. The variability within the zone of hydraulic fracture propagation is high: this is because the

$\Delta CFS$  values in close proximity to opening fractures can be very high, and so modelled stress changes within this zone are strongly dependent on the particular stochastic fracture model used as the input. However, further from the fracture zone, the variance in  $\Delta CFS$  values is low: in these areas the stress change is not sensitive to the particular stochastic fracture model used, and so can be considered to be robust. In other words, the general distribution and shape of the lobes of positive and negative  $\Delta CFS$  seen in 3.4 exist for all fracture models that have tensile fractures extending roughly 100 m from the well, and therefore the use of the median value allows us to examine the average effect of the fracture sets, without any perturbations produced by the stochastic model generation process.

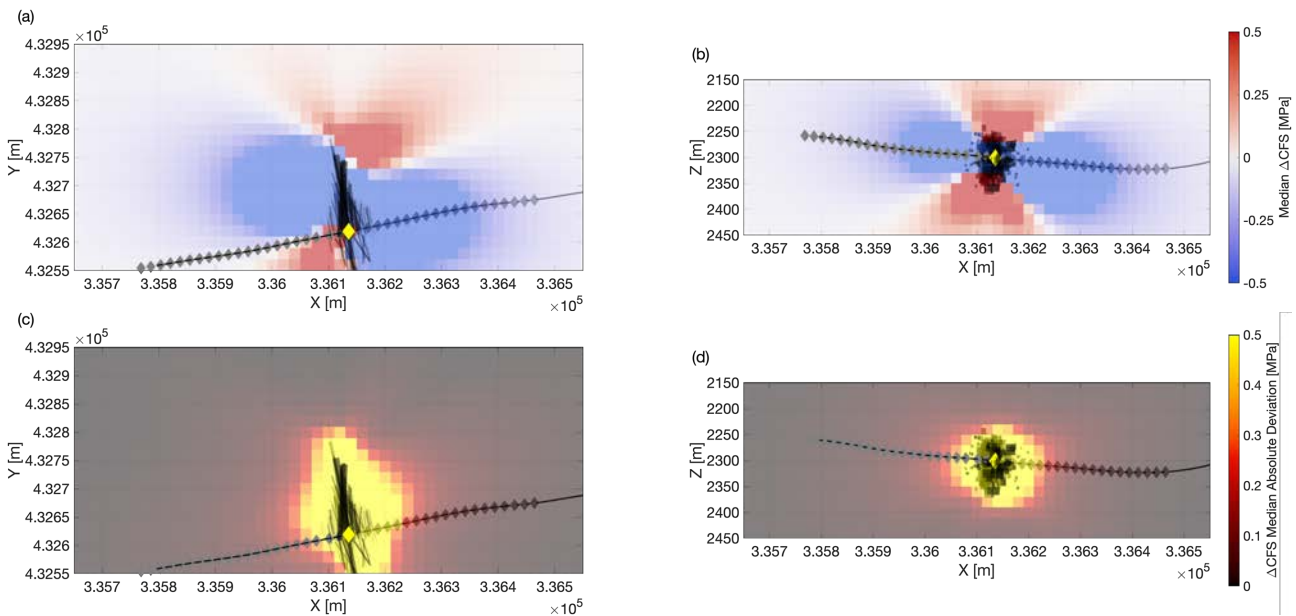


Figure 3.5: Map (a) and cross-section (b) showing the median  $\Delta CFS$  computed for a single hydraulic fracture stage (Stage 22 in this case). (c) and (d) show the median absolute deviation of  $\Delta CFS$ .

### 3.3. COULOMB INDEX

To assess whether stress transfer is playing a significant role in fault reactivation, we compare the lobes of positive and negative  $\Delta CFS$  with the observed microseismic event locations. If stress transfer effects are playing a significant role in triggering seismicity, then we would expect the majority of events to occur within lobes of positive  $\Delta CFS$ . If stress transfer is not playing a substantive role, then we would expect events to occur at random in both positive and negative lobes, and so have equal numbers of events within both.

The Coulomb Index,  $CI$ , is defined as the proportion of events (from 0 – 100 %) within a given population that are found within lobes of positive  $\Delta CFS$ . A  $CI$  value of 50% would indicate that events occurred equally in positive and negative  $\Delta CFS$  lobes, and therefore that stress-transfer effects have not played a significant role in triggering seismicity. In contrast, a high  $CI$  value would indicate that most events occurred in regions that experienced a positive  $\Delta CFS$  change, and therefore that stress-transfer played a significant role in triggering seismicity.

### 3.4. RESULTS

Figure 3.6 shows an example map and cross-section of  $\Delta CFS$  changes for Stage 30 ( $\Delta CFS$  maps are shown for all stages in Appendix III). For a given stage we compute  $\Delta CFS$  for 3 deformation cases:

1. Deformation induced by hydraulic fracturing of all preceding stages. This shows the  $\Delta CFS$  conditions at the initiation of the stage in question.
2. Deformation induced by hydraulic fracturing of the stage in question. This shows the additional  $\Delta CFS$  change induced by the stage in question.
3. Combining the deformation from all preceding stages with the stage in question. This shows the  $\Delta CFS$  changes that will have occurred by the end of the stage in question.

Figure 3.6 also shows the microseismicity that occurred during Stage 30, coloured by the  $\Delta CFS$  change at each event location. For this stage, the microseismic event locations are controlled by the positions of positive lobes of  $\Delta CFS$ , indicating that transfer of stress from tensile fracture opening is playing a dominant role in producing the microseismicity observed at PNR-1z.

The dominant role played by stress transfer can be further demonstrated by considering the  $C/I$  values computed on a stage-by-stage basis. In Figure 3.7, we find that  $C/I$  values consistently exceed 50%, and for most of the stages where reactivation of the NEF-1 fault was observed, once the impact of deformation associated with prior stages is taken into account the  $C/I$  values consistently exceed 75%. These values imply that stress transfer played a key role in causing fault reactivation during stimulation of PNR-1z.

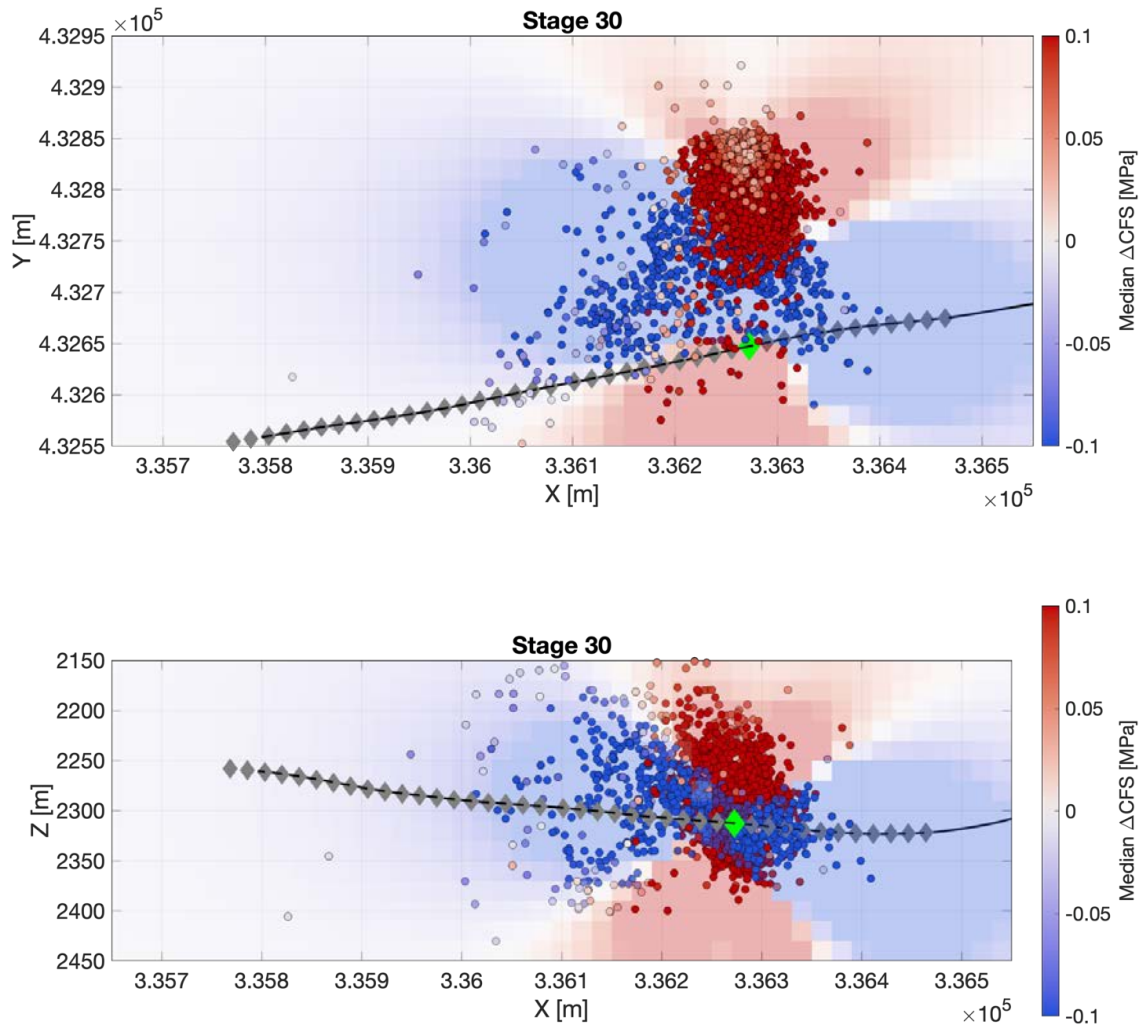


Figure 3.6: Map (a) and cross-section (b) showing the median  $\Delta\text{CFS}$  for Stage 30, with the microseismic events (dots) overlain and coloured by the  $\Delta\text{CFS}$  at the event's location. Note that the map (a) is plotted at the well depth, and the cross-section (b) at the Y-coordinate of the injection point, onto which the event positions are projected. As a result, in this plot events away from these planes that receive positive  $\Delta\text{CFS}$  may project into a negative lobe, and vice versa. This an inevitable consequence of collapsing 3-dimensional data into a 2-D plot.

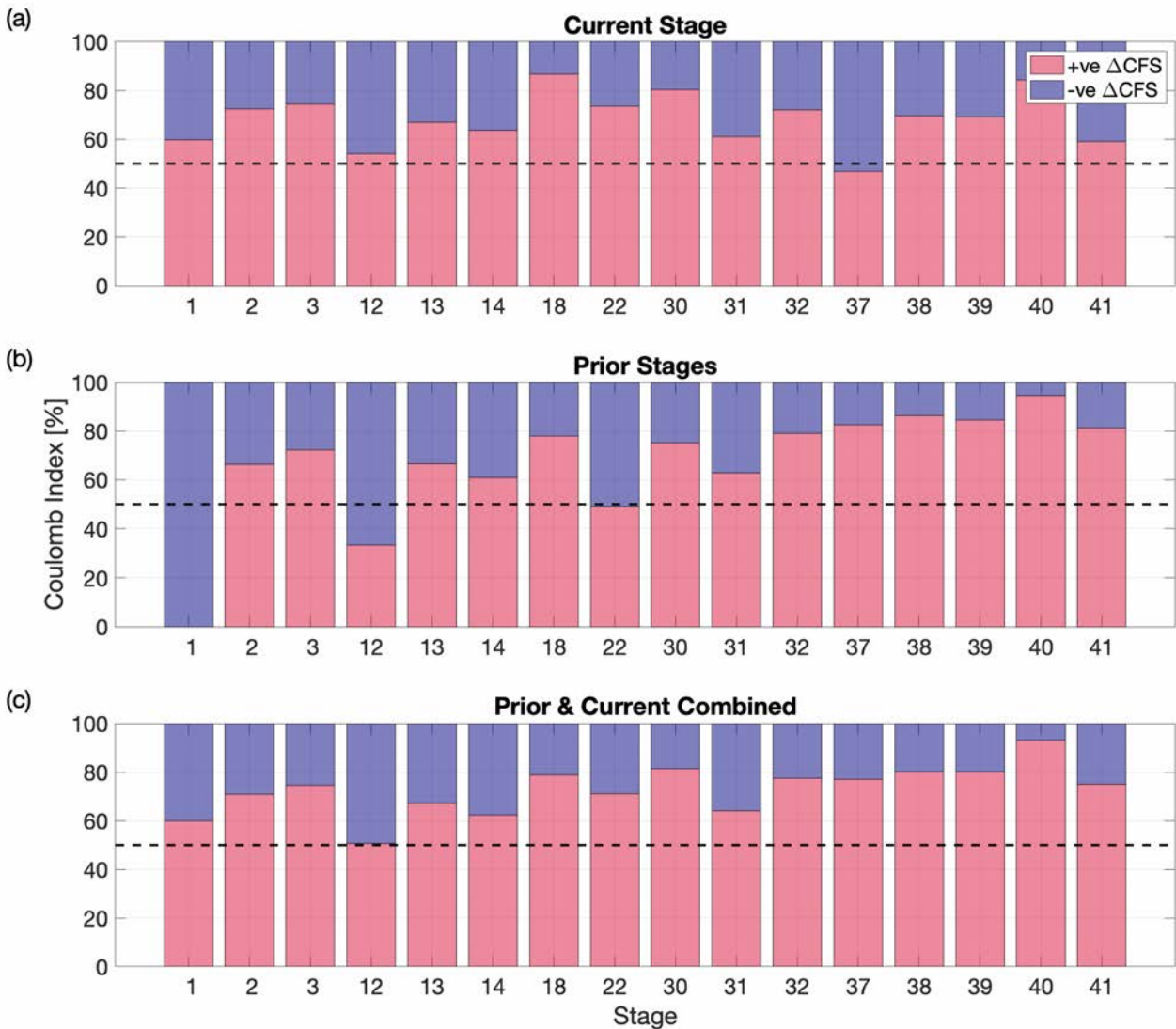


Figure 3.7: Coulomb index for each stage when considering deformation associated with (a) just the stage in question, (b) just the preceding stages, and (c) the current stage and preceding stages combined. CI values are consistently higher than 50%, especially for the later stages (18 onwards) where re-activation of the NEF-1 fault was observed.

In Section 2.7 we presented several microseismic observations that were at odds with fault reactivation induced solely by diffusion of elevated pore pressures. In the following section we re-evaluate these observations with respect to our modelled  $\Delta CFS$  values.

During Stages 2 and 3, we observed microseismicity occurring in a zone approximately 100 m to the NE of the main hydraulic fracturing zone. In Figure 3.8 we plot the  $\Delta CFS$  change resulting from the tensile opening of hydraulic fractures produced by these 3 stages. We observe a lobe of positive  $\Delta CFS$  change that extends to the NE from the hydraulic fractures of Stages 1 – 3, and the events to the NE are found in the middle of this lobe. The overall CI for Stage 3 events is 75%.

We conclude that the deformation associated with tensile opening of hydraulic fractures around Stages 1 – 3 caused stress transfer that promoted slip on NE-SW striking fractures. Evidently,

such features were present in the subsurface in a position roughly to the north of Sleeves 9 – 11, and the reactivation of these features, creating the cluster of microseismicity to the NE of Stages 1 – 3, was caused by stress changes generated by the tensile opening of hydraulic fractures.

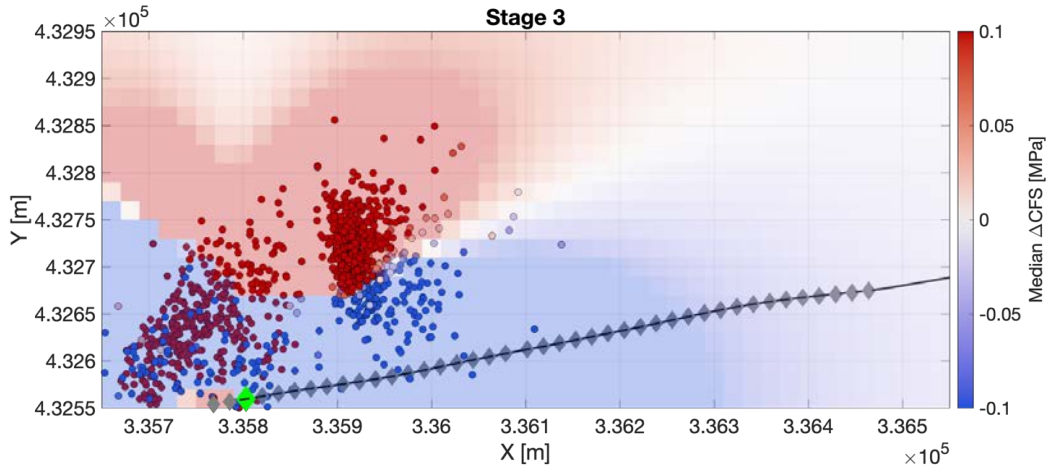


Figure 3.8: Map of median  $\Delta CFS$  produced by Stages 1 – 3, with the microseismic events during Stage 3 (dots) coloured by the  $\Delta CFS$  at each event's location. A lobe of positive  $\Delta CFS$  extends to the northeast, in which a second cluster of events occurs.

The  $\Delta CFS$  change associated with Stage 12 is plotted in Figure 3.9. In Section 2.7 we noted that microseismicity was able to propagate to the NE from certain stages, but there was minimal back-propagation of seismicity to the SW. The reason for this apparent “one-way” connection is clear when the  $\Delta CFS$  change created by Stage 12 is plotted: westward of the active hydraulic fracturing, a zone of negative  $\Delta CFS$  creates a stress-shadow (e.g., Green et al., 2015) in which microseismicity will be suppressed.

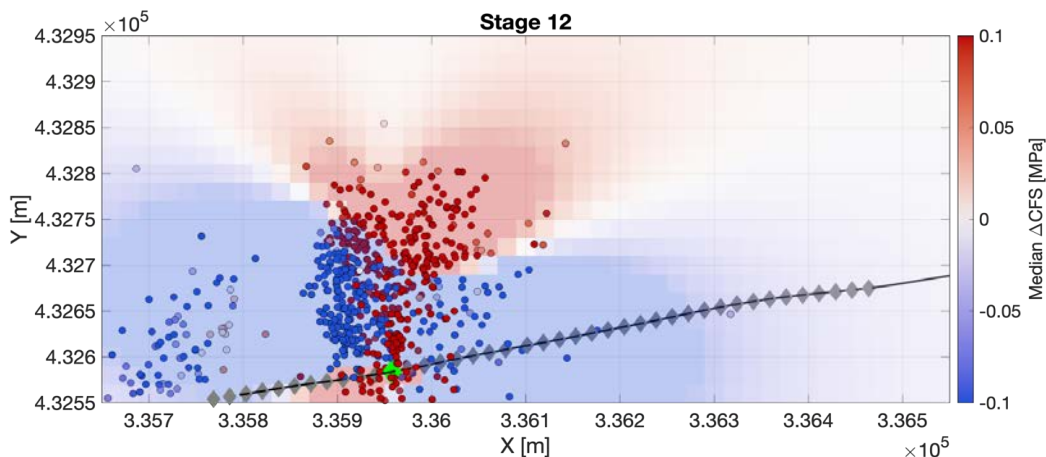


Figure 3.9: Map of median  $\Delta CFS$  produced by Stage 12, with the microseismic events (dots) during these stages, coloured by the  $\Delta CFS$  at each event's location. A lobe of negative  $\Delta CFS$  now occurs in the region where microseismicity occurred during Stages 1 – 3, suppressing activity in this area.

Stage 18 showed a very high rate of microseismicity given the injected volume of only  $10 \text{ m}^3$ , with events propagating over 100 m from the well, and producing the first  $M \geq 0.5$  event. Figure 3.10

shows the  $\Delta CFS$  values from all previous stages prior to Stage 18. We see that these prior stages create positive stressing in the region of Stage 18. Stage 18 is the first stage that intersects the pre-existing NEF-1 fault. Our results show that the previous stages created positive  $\Delta CFS$  changes in this area, stressing the fault such that it was able to re-activate and produce a large number of microseismic events with only minimal fluid injection at Stage 18. The  $CI$  for Stage 18 events, considering the deformation produced by all previous stages, is 78 %.

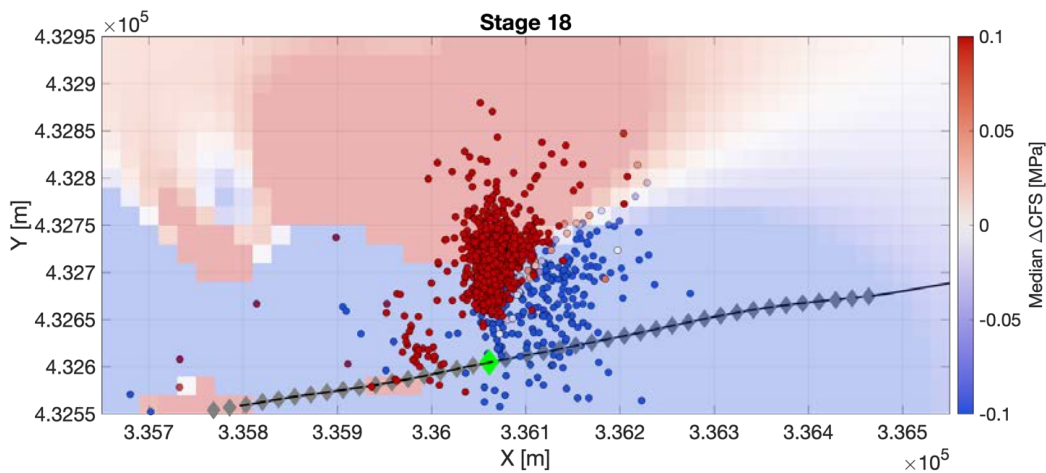


Figure 3.10: Map of median  $\Delta CFS$  changes produced by all of the stages prior to Stage 18, with the microseismic events that occurred during Stage 18 (dots) coloured by the  $\Delta CFS$  at the event's location. The previous stages caused stressing of the NEF-1 feature, which resulted in a large number of events occurring after a minimal volume of injection.

In the latter stages towards the heel of PNR-1z, we noted two features of interest: firstly, that microseismic events did not seem to back-propagate to the SW along the NEF-1 fault; and secondly that there was a clear gap between the injection sleeves at the well and the focus of the microseismicity. The  $\Delta CFS$  change produced by Stage 40 and all preceding stages is plotted in Figure 3.11. The majority of events occurred within regions in which deformation caused by this and previous stages had created positive stressing that promoted failure on NE-trending faults and fractures. Conversely, the regions closer to the well experience negative  $\Delta CFS$  changes, explaining why few microseismic events are observed here.

Whereas during Stage 22 we observed northeastward propagation of events along the fault zone, in these latter stages we do not observe significant numbers of events propagating back to the southwest. Figure 3.11 shows that the cumulative impact of the latter stages is to place the portion of the fault zone to the west of the active stage within a lobe of negative  $\Delta CFS$ , and therefore seismicity becomes suppressed. The significance of this effect can be seen in Figure 3.7: for Stages 30 – 41, when considering the cumulative impact of prior stages, the  $CI$  values are approximately 80%, indicating a strong stress transfer effect. As hydraulic fractures are created during each stage, a lobe of positive  $\Delta CFS$  is pushed towards the northeast, while a lobe of negative  $\Delta CFS$  is created behind (i.e. to the west) of the active stage. This geometry of positive and negative  $\Delta CFS$  lobes therefore has a strong control on where the fault zone is, and is not, reactivated.

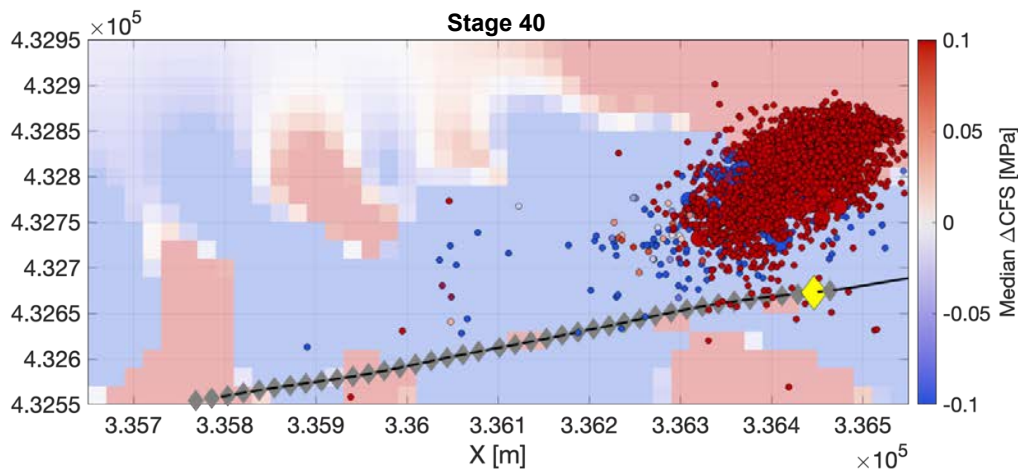


Figure 3.11: Map of median  $\Delta$ CFS changes produced by all of the stages up to Stage 40 inclusive, with the microseismic events that occurred during Stage 40 (dots) coloured by the  $\Delta$ CFS at the event's location. The previous stages caused stressing of the NEF-1 feature, which resulted in a large number of events occurring along this feature. Meanwhile, the region near to the well experiences negative  $\Delta$ CFS, leading to a gap between the well and the microseismicity.

The overall geometry and impact of this stress transfer effect is shown schematically in Figure 3.12. The fault strikes to the northeast, and in the present-day stress field favours left-lateral strike slip motion, i.e. the southeastern side of the fault moving to the northeast relative to the northwestern side. Hydraulic fractures extend northwards from the well. The tensile opening affects the stress field in the surrounding rock mass. The region west and northwest of the fractures is pushed to the west, and the region to the east and northeast of the fractures is pushed eastwards. Hence, the region to the east and northeast of the hydraulic fractures experiences stresses that are consistent with the preferred slip direction of the fault. The observed microseismicity is focussed within this zone. In contrast, regions to the west of the hydraulic fractures experience stresses acting in the opposite direction to the preferred fault slip direction, and microseismicity is suppressed in these regions.

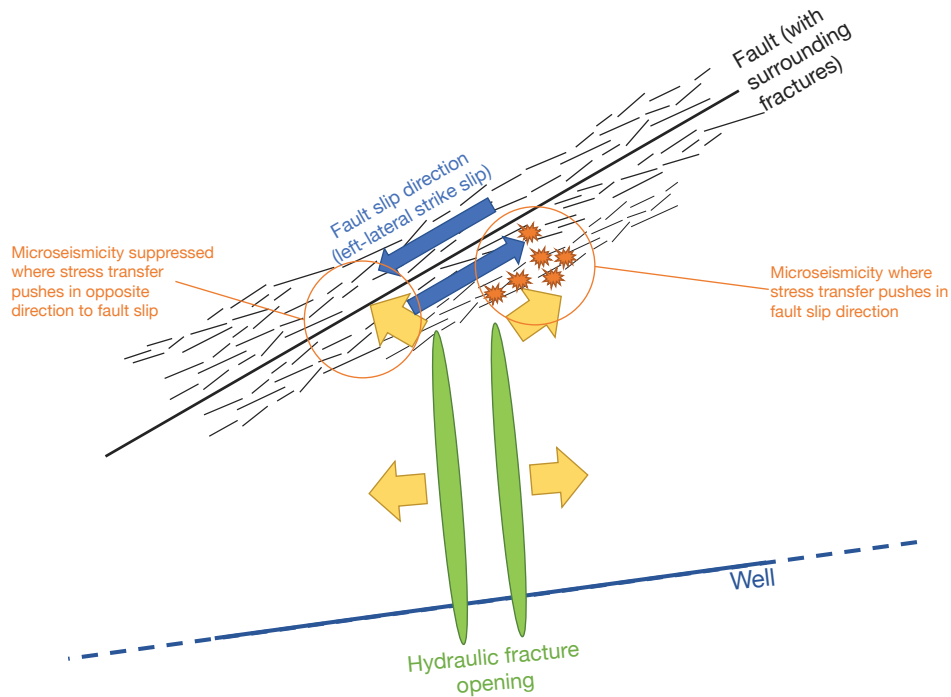


Figure 3.12: Schematic depiction of the stress transfer effect described above. The fault (and surrounding fracture zone, containing fractures with similar orientations) strikes to the northeast, and in the present-day stress field favours left-lateral strike slip movement. The hydraulic fractures extend northwards from the well, and the tensile opening exerts a force on the surrounding rock. Where that force pushes the rock in a direction that is subparallel to the preferred fault (and fracture zone) slip direction, microseismicity is promoted. Where that force pushes in the opposite direction, microseismicity is suppressed.

## 4. STRESS CHANGE ON MAPPED FAULTS

Prior to commencing operations, CRL acquired 3D seismic reflection data from this area, with which they identified several pre-existing faults. Several “seismic disturbances”, which are features in the reflection seismic data that could potentially represent smaller faults at the limit of detectability using the 3D seismic method, were also identified (Cuadrilla Resources, 2018).

The magnitude of an earthquake is determined by the dimensions of the rupture area (Hanks and Kanamori, 1979), so larger faults are capable of producing larger earthquakes. Reactivation of the larger faults identified by the reflection seismic survey could therefore pose a higher seismic hazard than the NEF-1 fault identified by the microseismic monitoring.

It is therefore of interest to assess how the stress-transfer effects described in Chapter 3 would have affected the stress conditions on the pre-existing faults identified in the hydraulic fracture plan.

We follow the method described in Chapter 3, computing the total deformation caused by tensile fracture opening from every fracturing stage. We resolve these stress changes into  $\Delta CFS$  changes resolved onto each fault orientation, across the full extent of each fault plane. Some of the fault planes are slightly curved – in such cases we fit an average fault plane orientation to the overall fault shape. Figure 4.1 shows an example of the  $\Delta CFS$  changes mapped onto the PNR fault, and the SD6 seismic discontinuity. The total  $\Delta CFS$  from every stage mapped onto each fault is shown in Appendix IV.

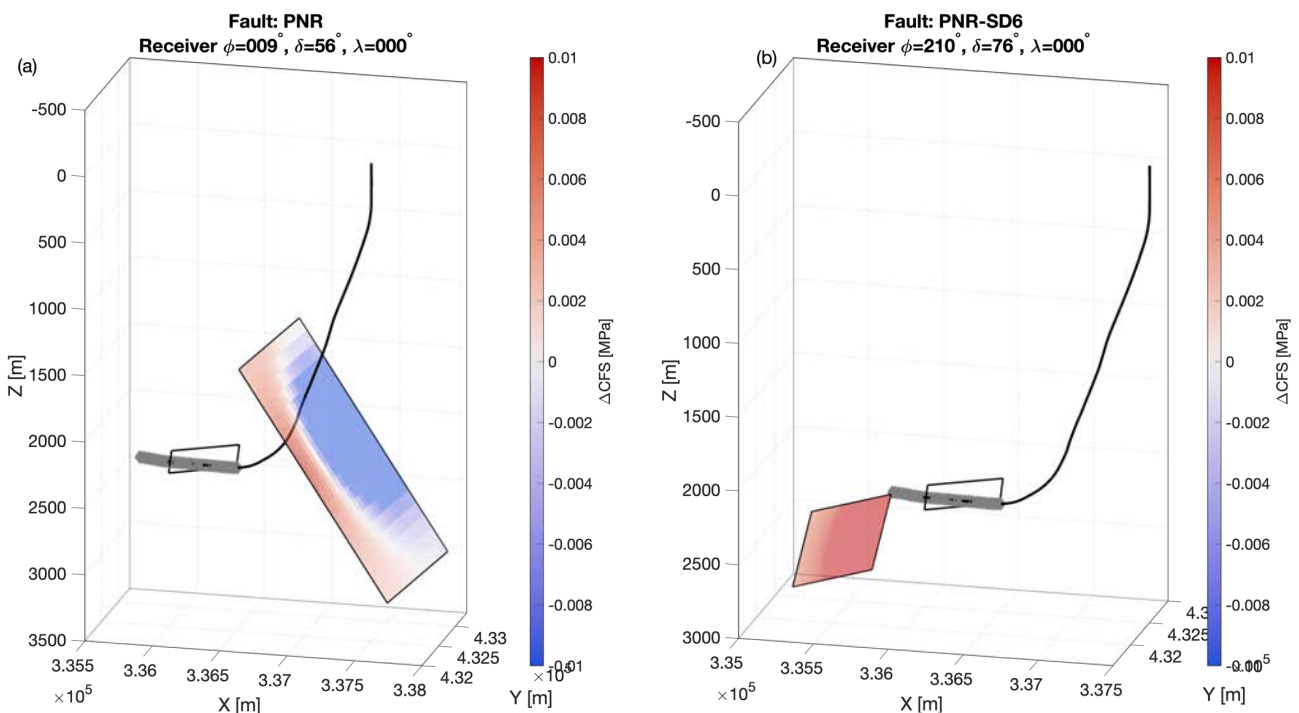


Figure 4.1:  $\Delta CFS$  changes resolved onto the PNR fault (a) and the SD6 seismic discontinuity (b) from the total deformation associated with hydraulic fracturing in PNR-1z. Note that the colour scale in this figure represents an order of magnitude smaller range than the figures shown in Chapter 3.

#### 4.1. RESULTS

Table 4.1 lists the minimum, median and maximum  $\Delta CFS$  changes experienced by each of the features identified by Cuadrilla Resources (2018).

Fault Name	Max +ve $\Delta CFS$ Change [MPa]	Max -ve $\Delta CFS$ Change [MPa]	Median $\Delta CFS$ Change [MPa]	% +ve to -ve $\Delta CFS$ Change [MPa]
Annas Road	3.41E-03	3.96E-04	-1.97E-02	74
Haves Ho	1.35E-03	6.65E-05	-5.44E-03	79
Kink	1.00E-03	1.97E-04	6.97E-05	100
Moor Hey	5.59E-05	-1.64E-05	-5.10E-03	41
Moor Hey B	-6.34E-05	-1.53E-03	-2.80E-02	0
PNR	9.59E-03	-2.60E-03	-5.59E-02	38
Preese Hall	1.23E-03	3.57E-04	1.30E-04	100
Thistleton N	9.13E-06	-2.36E-05	-4.42E-04	24
Thistleton S	4.79E-04	1.88E-05	-9.60E-04	70
PNR-SD1	1.96E-03	1.26E-03	-3.76E-03	84
PNR-SD2	7.36E-03	3.25E-03	1.33E-03	100
PNR-SD3	4.40E-01	5.72E-04	-1.55E+00	52
PNR-SD4	2.77E-02	1.35E-02	-2.44E-02	83
PNR-SD5	3.06E+00	-1.40E-02	-1.55E+01	44
PNR-SD6	4.18E-02	1.35E-02	5.62E-03	100

Table 4.1:  $\Delta CFS$  changes resolved onto the faults and seismic discontinuities identified around the PNR-1z well.

For the larger, named faults in Table 4.1, the modelled  $\Delta CFS$  changes are small, typically less than 0.01 MPa. These changes are at least an order of magnitude smaller than the modelled  $\Delta CFS$  changes on the NEF-1 fault produced in Chapter 3. These faults are further from the stimulation zones of the PNR-1z well, and stress transfer effects dissipate with distance. Clearly, the stress-transfer effects that caused reactivation of the NEF-1 fault are not of sufficient magnitude to produce reactivation of the larger, but more distant, faults identified by CRL's 3D reflection seismic survey.

Some of the smaller seismic discontinuities identified by CRL did receive significant, positive  $\Delta CFS$  changes – especially PNR-SD4 and PNR-SD6. However, no microseismicity occurred along either of these features. This absence of microseismicity can be accounted for in two ways. It is possible that the modelled  $\Delta CFS$  changes on these discontinuities is too small to cause reactivation. Alternatively, these seismic discontinuities are at the limit of what can be detected using 3D reflection surveys; it is therefore possible that the interpretation of these features as faults or fractures is not correct, and so there would be no reason to expect microseismicity in these areas.

## 5. FLUID FLOW MODELLING

As an alternative causative mechanism for the induced seismicity, we examine the diffusion of elevated pore pressures. In particular, the permeability of the pre-existing NEF-1 feature is not well constrained. Our objective therefore is to investigate the impact of the permeability (or impermeability) of this feature on the resulting spatial and temporal evolution of pore pressure.

We do this using the USGS code *MODFLOW-2005* (Harbaugh, 2005) to construct numerical pore pressure diffusion models. This modelling approach represents a severe simplification because it neglects several key physical processes at play during the hydraulic fracturing process:

- Formation of hydraulic fractures: in reality, hydraulic fractures are formed as the hydraulic stimulation is conducted, creating a high-permeability pathway extending from the well. Simulating this process requires a fully-coupled fluid-flow/geomechanical solver that combines fluid flow effects with the mechanical impacts of pressure changes on the rock (e.g., Profit et al., 2016). Instead, in our simulations we pre-insert zones of elevated permeability, based on the expected hydraulic fracture dimensions around the injection points as each stage is conducted.
- Pressure-dependent permeability: in a medium dominated by flow through fractures, one might expect the permeability to be pressure-dependent, since increased pressures may cause fractures to open, increasing the ability of fluids to flow (e.g., Wu and Pruess, 2000).
- Single phase fluid: in reality there may be multiple fluid phases, such as gas, *in situ* brines, and hydraulic fracturing fluid, flowing within the pore space. However, *MODFLOW* allows only a single fluid phase to be modelled.

These limitations could be addressed with a fully-coupled multi-phase fluid-flow/geomechanical solver (e.g., Profit et al., 2016). However such approaches are extremely computationally-expensive, and beyond the scope of this study, which aims simply to investigate the first-order effects of a pre-existing permeable fault or fracture corridor on the resulting pore pressure evolution.

### 4.1. FLUID-FLOW MODELLING APPROACH

The *MODFLOW* finite difference code solves the groundwater flow equation in three dimensions for a constant density and viscosity fluid in a heterogeneous and anisotropic aquifer:

$$\frac{\delta}{\delta x} \left( K_{xx} \frac{\delta h}{\delta x} \right) + \frac{\delta}{\delta y} \left( K_{yy} \frac{\delta h}{\delta y} \right) + \frac{\delta}{\delta z} \left( K_{zz} \frac{\delta h}{\delta z} \right) = S_s \frac{\delta h}{\delta t} - Q(t) \quad (5)$$

where  $K_{xx}$ ,  $K_{yy}$ , and  $K_{zz}$  are the principle components of the hydraulic conductivity tensor,  $h$  is the hydraulic head,  $Q$  is the flow rate per unit volume of injection, and  $S_s$  is the specific storage of the porous medium. The finite difference form of the above equation is derived using the continuity equation: the sum of all flows into and out of a cell must be equal to the rate of change of fluid stored. Fluid flow between cell faces is dictated by Darcy's law, and is dependent on the difference in pressure between the two cells, the conductivity, the area of the faces normal to

flow, and distance between the centres of each cell. The change in hydraulic head  $\Delta h$  is equivalent to pore pressure  $\Delta P$ , and is related by the specific weight of the fluid  $\gamma$  (a measure of the fluid's density):

$$\Delta P = \gamma \Delta h \quad (6)$$

Hydraulic conductivity  $K$  is related to permeability  $\kappa$  by the specific weight  $\gamma$  and dynamic viscosity  $\mu$  of the fluid:

$$K_{ij} = \frac{\gamma}{\mu} \kappa_{ij} \quad (7)$$

Both specific weight and dynamic viscosity are a function of temperature. We assume values for water at around 30-40 °C, partway between the ambient temperature of injection fluid prior to injection, and the reservoir temperature (on the order of 100 °C):  $\gamma = 9750 \text{ N m}^{-3}$ ;  $\mu = 8 \times 10^{-4} \text{ Pa s}$ .

Fluid pressure dissipation is controlled primarily by permeability and specific storage. Higher permeabilities aid flow, and higher storages slow the dissipation due to more fluid being stored or released for a given change in pressure. The only variable that we change in the test cases below is the permeability of the fault zone, and not its specific storage, in order to isolate permeability as the principal variable. We assume a specific storage of  $1 \times 10^{-5} \text{ m}^{-1}$ , a value typically used for impermeable shales and limestones (e.g., Keranan et al., 2014; Hearn et al., 2018).

The model is constructed first by defining the grid and the material properties of each cell, chiefly the permeability  $\kappa$ . This is followed by defining the locations of each of the injection points, in this case the middle of each sleeve, and the rate of flow  $Q$  through each as a function of time. The model then iteratively solves the groundwater flow equation in time increments and outputs the hydraulic head in each grid cell. The change in fluid pressure  $\Delta P$  at a given output time, can then be calculated by subtracting it from the starting conditions.

Our grid is 4 km by 4 km in  $x$  and  $y$ , and 1.5 km in  $z$ , with the well and fault zone in the centre of the domain. Grid size varies depending on the position within the grid, with the finest resolution (10 m) in the 500 m in all directions around the horizontal section of well. The roughly 2 km of excess grid space around the well is used to avoid any effects imposed by the boundary conditions. In our case, with a highly impermeable matrix surrounding the injection, pressure changes extend only hundreds of the metres, and thus do not interact with the boundaries. We assume a constant head boundary condition at the very edges of the model, and a uniform initial in situ pressure of 23 MPa, which is approximately hydrostatic.

We assume a typical shale horizontal permeability of 100 nD for the cells surrounding the wells (Chalmers et al., 2012; Dong, 2017). We assume vertical permeability is an order of magnitude smaller than horizontal permeability. At the start of each stage, we add a zone of enhanced permeability simulating the growth of hydraulic fractures, using a Gaussian function to simulate the gradual decrease in permeability as hydraulic fractures become less dense further from the injection point. In the first tens of metres around the stage, the permeability in the direction of fracture growth is equal to 1 D. In this hydraulically fractured zone,  $\kappa$  is assumed to be anisotropic, with permeability ten times lower perpendicular to the direction of fracture growth.

The hydraulically fractured zones extend for around 150 m to 200 m from the sleeve location to the north of the well, and around 50m to the south, again reflecting the asymmetric growth of fractures inferred from the microseismic. The enhanced permeability zone extends around 50 m horizontally either side of the sleeve, and around 75 m vertically above and below (Figure 5.1).

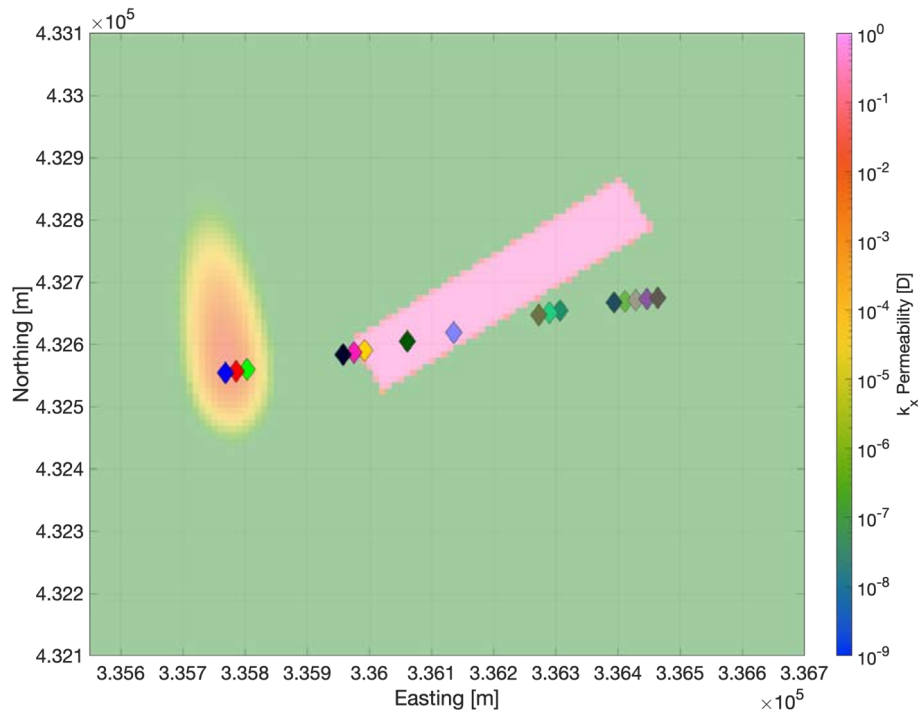


Figure 5.1: Map view of modelled permeability for fluid flow simulations. A zone of elevated permeability is simulated extending northwards from the active stage. The pre-existing NEF-1 feature is also included with an elevated permeability.

The fault zone is added as a region of higher permeability, simulating either a natural fracture network, or a fault damage zone. We have three test cases for the fault-parallel  $\kappa$ : 5 mD; 50 mD; and 500 mD. We refer to these as the high, medium and low-permeability model cases.

The fault-perpendicular  $\kappa$  is assumed to be an order of magnitude lower, representing the orientation of fractures within this zone. The extent of the fault zone is constrained by the microseismic event locations, particularly the highest magnitude events which occurred on the planar feature and the events that continued during the hiatus. This fault zone is modelled as 500 m long, 100 m wide, and 200 m high, is oriented vertically, and extends eastwards from Sleeve 18 to Sleeve 40.

We use simplified boxcar injection rates and only include main stages, not any minifrac or smaller injection tests. We compute the pore pressure in our grid at regular intervals during injection: every 30 mins during injection through each stage; once every hour for at least 3 hours after pumping; and every 3 three hours until the next stage begins. During the hiatus between the main stage injection in Stages 32 and 37, we compute the pressure on a daily basis.

The pressure distributions that we model are highly dependent on the assumptions made about the dimensions of the higher-permeability zones created by the hydraulic fractures, which are not well constrained *a priori*. Therefore the model results are by no means a definitive description of

the pressure changes that actually occurred in the subsurface. Nevertheless, they give a useful first-order indication of the expected extent of the subsurface that might be affected as pore pressures diffuse outwards through the shale rock.

#### 4.2. RESULTS

Figures 5.2 to 5.7 show model snapshots of either the total pressure increase over the course of the stimulation of the well, or the pressure increase over a particular stage, with microseismic events overlain. This allows us to qualitatively assess whether microseismicity is occurring in areas where we expect pore pressures to increase.

In Chapter 2 we identified that certain aspects of the spatio-temporal evolution of the events were not consistent with being driven by diffusion of elevated pressures from the well. This is further demonstrated in the modelling shown here. For instance, Figure 5.2 shows the modelled pressure increases produced by Stages 1 – 3. The events that are immediately to the north of the well fall within the zone of pore pressure increase. However, the second cluster of events located further to the northeast fall well outside this zone of pressure increase.

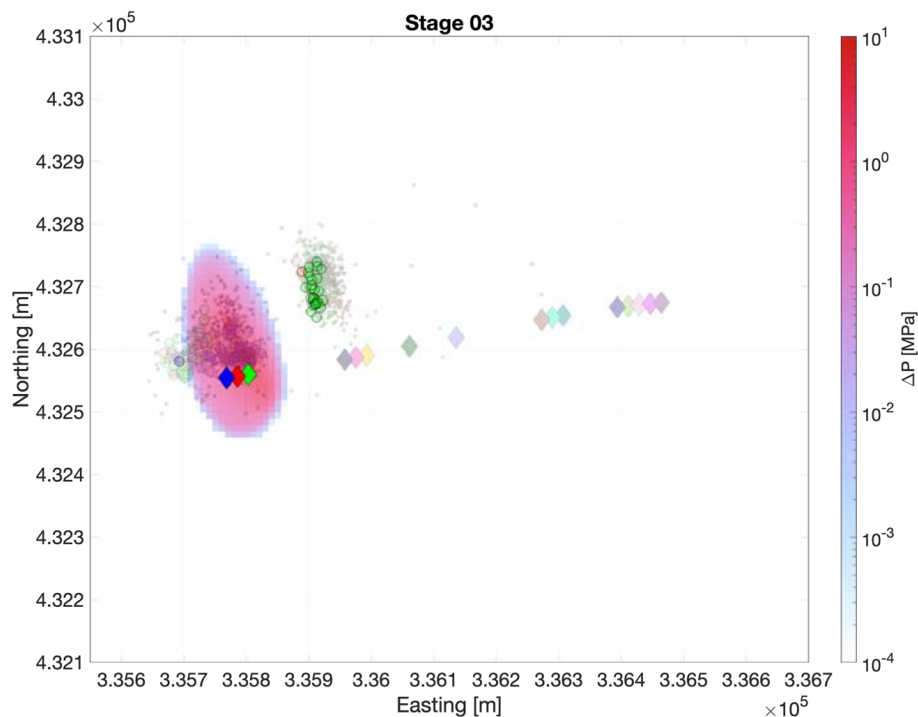


Figure 5.2: Modelled total pressure increase after Stages 1 – 3, with microseismic events overlain. A pulse of elevated pressure surrounds the active stages, but this does not extend out to the cluster of events to the NE of the stages.

Figure 5.3 shows the pore pressure increase caused by Stage 18. Because this stage injected only a very small volume, pressure changes are small and contained very close to the well. However, microseismicity extends over 150 m northwards from the well, well outside the modelled zone of pore pressure increase. Similarly, Figure 5.4. shows the pore pressure increase caused by Stage 37. This stage injected approximately 200 m<sup>3</sup>, significantly less than the full stage volume of 400 m<sup>3</sup>. Again, our models find that the extent of the pore pressure increase is

limited and does not reach the loci of the microseismic events, even for the high-permeability fault case.

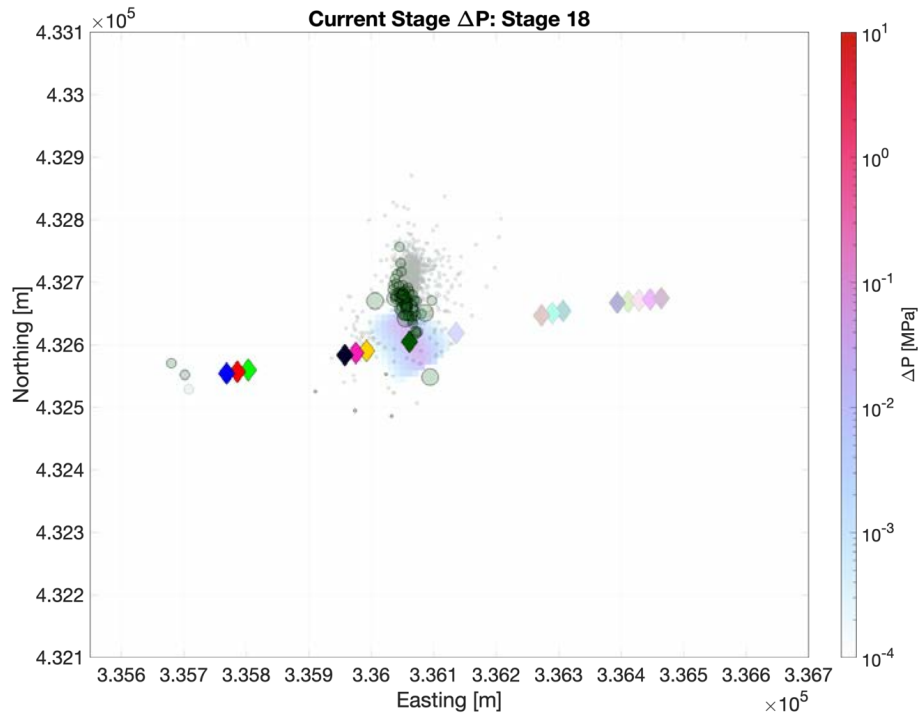


Figure 5.3: Modelled pressure increase produced by Stage 18 for the high fault  $\kappa$  case. This stage injected less than  $10 \text{ m}^3$  of fluid, and so any pressure change is extremely limited around the injection point.

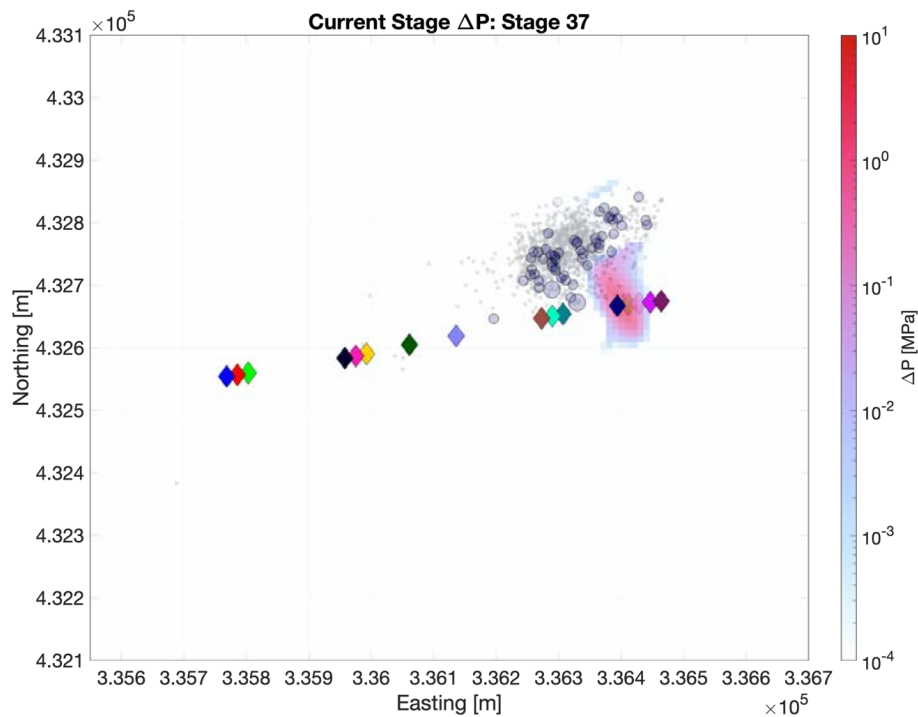


Figure 5.4: Modelled pressure increase produced by Stage 37 for the high fault  $\kappa$  case. The volume in this stage was insufficient to have a significant impact on the NEF-1 fault, and the modelled pressure pulse does not reach the position where most of the microseismicity occurs.

In Figures 5.5 – 5.7 we compare the results provided by the high and low permeability NEF-1 fault cases. Figure 5.5. shows the total pressure increase from all stages up to and including Stage 14. We find that, for the high fault permeability case, the increased pressure is able to enter the NEF-1 fault and propagate along it, whereas pressure propagation is much more restricted in the low permeability case. The microseismicity during Stage 14 is generally found in close proximity to the injection point, and does not show any evidence for propagation along the fault. We therefore infer that, at least initially, the NEF-1 fault zone may have had a relatively low permeability.

In contrast, Figure 5.6 shows the modelled pressure change produced by Stage 22. The events during Stage 22 were observed to extend to the NE and SW along the NEF-1 fault. This behaviour is better re-created by the higher fault permeability case, where elevated pressures are also able to extend along the fault. If so, this implies that the interaction between the hydraulic fracturing and the fault has acted to increase its permeability. However, as described in Chapter 4, a significant proportion of these events occurred in regions experiencing a positive  $\Delta CFS$  caused by the tensile opening of the hydraulic fractures, in which case the permeability of the fault will be irrelevant with respect to the occurrence of microseismicity.

Figure 5.7 shows the total modelled pressure increase caused by all stages from 1 – 37. We note that pressures are transferred along the length of the NEF-1 fault, with pressure distributions that are very similar for both the high and low fault permeability cases. We infer that the observed microseismic distributions are therefore not particularly useful in differentiating between these cases.

The lateral limits of the pore-pressure increase are therefore controlled by the assumed lateral extent of the fault (shown in Figure 5.1). Extending this zone would allow pressure to propagate further. Therefore, if the NEF-1 fault zone extended further to the northeast, we would expect to observe pore pressure increases further to the northeast, and therefore microseismicity occurring further to the northeast. The fact that it does not indicates that the fault zone probably does not extend further to the east the approximately in line with Stages 39 or 40.

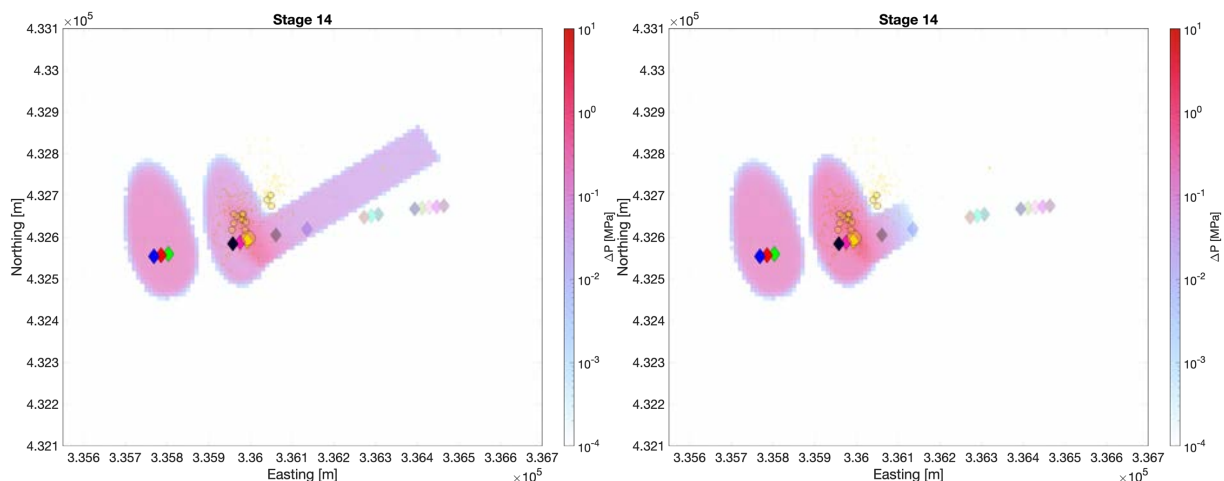


Figure 5.5: Modelled total pressure increase after Stage 14 for the high fault  $\kappa$  (left) and low fault  $\kappa$  (right) cases. In the high  $\kappa$  case, pore pressure is transferred along the NEF-1 fault, whereas for the low  $\kappa$  case, the pressure pulse is much more restricted.

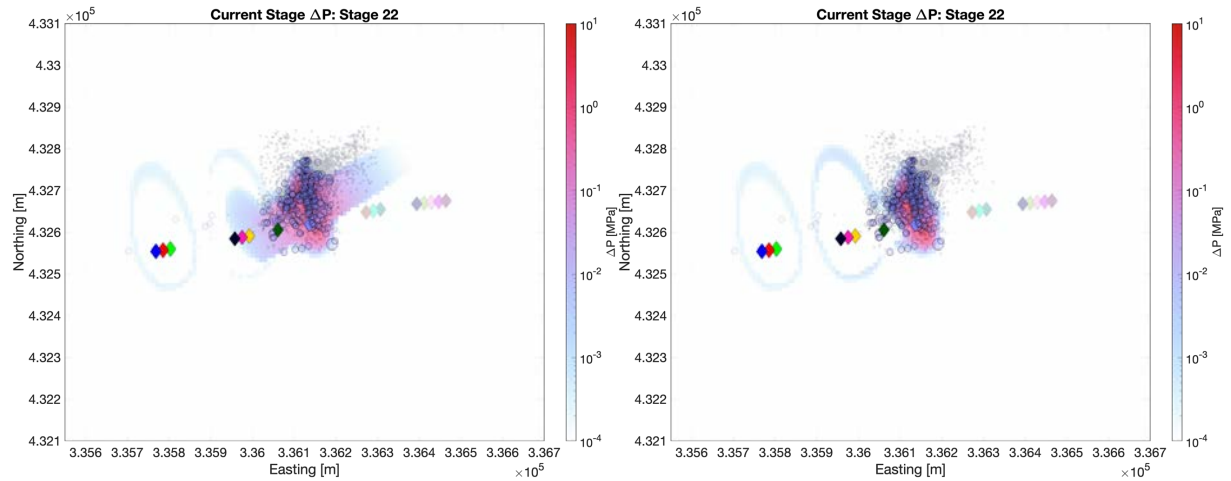


Figure 5.6: Modelled pressure increase produced by Stage 22 for the high fault  $\kappa$  (left) and low fault  $\kappa$  (right) cases. In the higher  $\kappa$  case, the pressure pulse is able to extend along the NEF-1 fault.

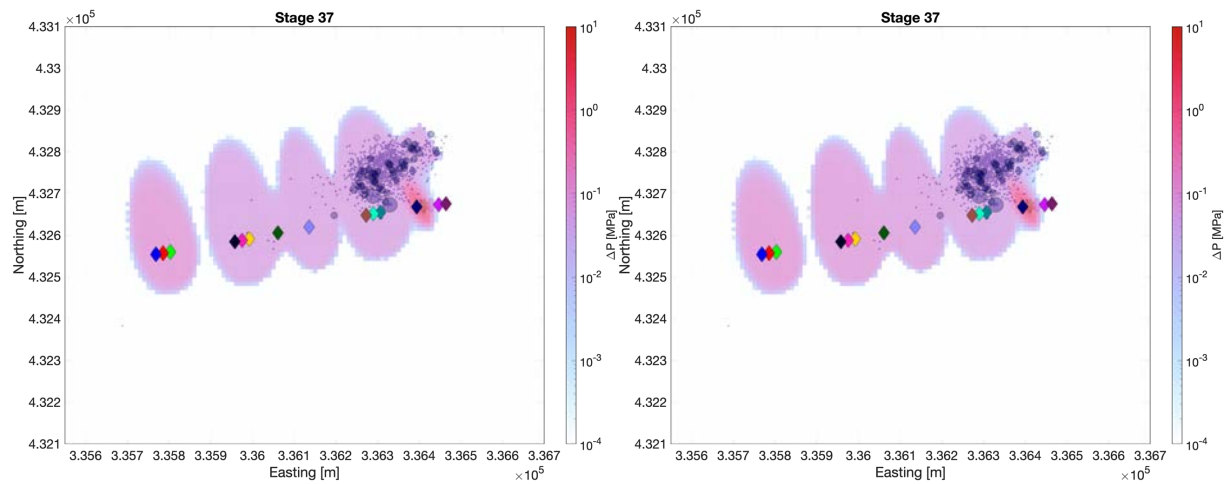


Figure 5.7: Modelled pressure increase produced by all stages from Stage 1 – 37 for the high fault  $\kappa$  (left) and low fault  $\kappa$  (right) cases. The combined impact of multiple stages is to cause elevated pressures along the length of the NEF-1 fault, regardless of the assumptions made about its permeability. The limit to pressure transfer is therefore controlled by the assumed dimensions of the feature.

## 6. CONCLUSIONS

In this study we examine and interpret the microseismicity induced by hydraulic fracturing in the PNR-1z well, Lancashire, with a particular focus on understanding the interaction between the hydraulic fracturing and any pre-existing faults.

The microseismic observations reveal the presence of a pre-existing fault or fracture zone running to the northeast from the well. Most of the larger seismic events occurred along this feature, which was intersected by many of the stages along the horizontal well. This fault was not visible on the 3D seismic reflection data acquired at the site.

The spatial and temporal evolution of the microseismicity produced several observations that are difficult to explain if events are driven solely by elevated fluid pressures and hydraulic fracture propagation away from the well. These observations included clusters of events that were spatially separated from the injection point, and the occurrence of events at large distances from the well for stages with small injection volumes. The “ $r-t$ ” behaviour of the events showed microseismicity occurring near-instantaneously across a range of distances, as opposed to an increase in distance with time that might be expected for a process controlled by diffusion of pore fluid pressure from the well.

These observations led us to investigate the role of elastic stress transfer in driving the observed seismicity. We did so using stochastic models to represent the loading created by the tensile opening of hydraulic fractures, computing the stress change that would then occur on features with the same orientation as the observed fault. We find that overall there is a strong correlation between regions that receive positive  $\Delta CFS$  changes and the occurrence of microseismicity, implying that this mechanism is an important one in controlling fault reactivation at PNR-1z. As the hydraulic fracturing progressed eastward along the well, a lobe of positive  $\Delta CFS$  change developed to the northeast of each active stage, pre-stressing the region into which subsequent fracture stages were conducted. This effect may account for why some stages produced significant amounts of microseismicity for relatively small injection volumes. The regions to the west, i.e., behind the active stages typically received negative  $\Delta CFS$  changes, acting to clamp the fault. This may explain why there was relatively little “back-propagation” of microseismicity to the west along the fault, and why the fault was never active along its entire length at any one time, since some portions of the fault were receiving positive  $\Delta CFS$  change, and others negative  $\Delta CFS$  change, at any one time.

These effects will be highly dependent on the specific orientations of both the hydraulic fractures and the receiving faults, and so cannot easily be generalised to other sites. However, the stochastic modelling approach, combined with the PSCMP modelling code, is able to provide results at a speed that could plausibly be applied in near real time during injection operations. Doing so could enable operators to identify whether their planned stimulation program is likely to stress or to clamp any faults identified before or during injection, and potentially to make appropriate adjustments to their program to minimise induced seismicity.

Having established that stress transfer effects were playing an important role, we then examined the potential impact of these effects on the pre-existing faults identified using reflection seismic surveys. We find that stress transfer effects do not have a significant impact on any of the larger

faults identified in the HFP. Two of the smaller “seismic discontinuities”, PNR-SD4 and PNR-SD6, did receive significant, positive  $\Delta CFS$  changes. However, the lack of any microseismicity on these features brings into question whether they are actually pre-existing faults, since they are at the limit of what can be resolved using reflection seismic imaging.

We also develop some simple fluid-flow models to investigate the role of pore pressure diffusion in triggering the seismicity. These models are simple in nature, as they do not include coupled fluid-flow/geomechanical effects, pressure-dependent permeability, or multi-phase flow. Nevertheless, they provide an interesting first-order idea of how elevated pore-pressures might be transferred into the rock from the well. We find that, as indicated by the stress-transfer modelling, there are areas in which the spatial distribution of microseismicity cannot easily be explained solely by pore pressure effects. We go on to use these models to investigate how the permeability of the NEF-1 fault zone, which is not constrained a priori, could affect the pressure distribution in the subsurface. Unfortunately, it was not possible to make any strong conclusions about the permeability of the fault. However, it is clear from the lack of microseismicity any further to the east than the heel-most stages that the feature does not extend further than approximately 200 m from the well.

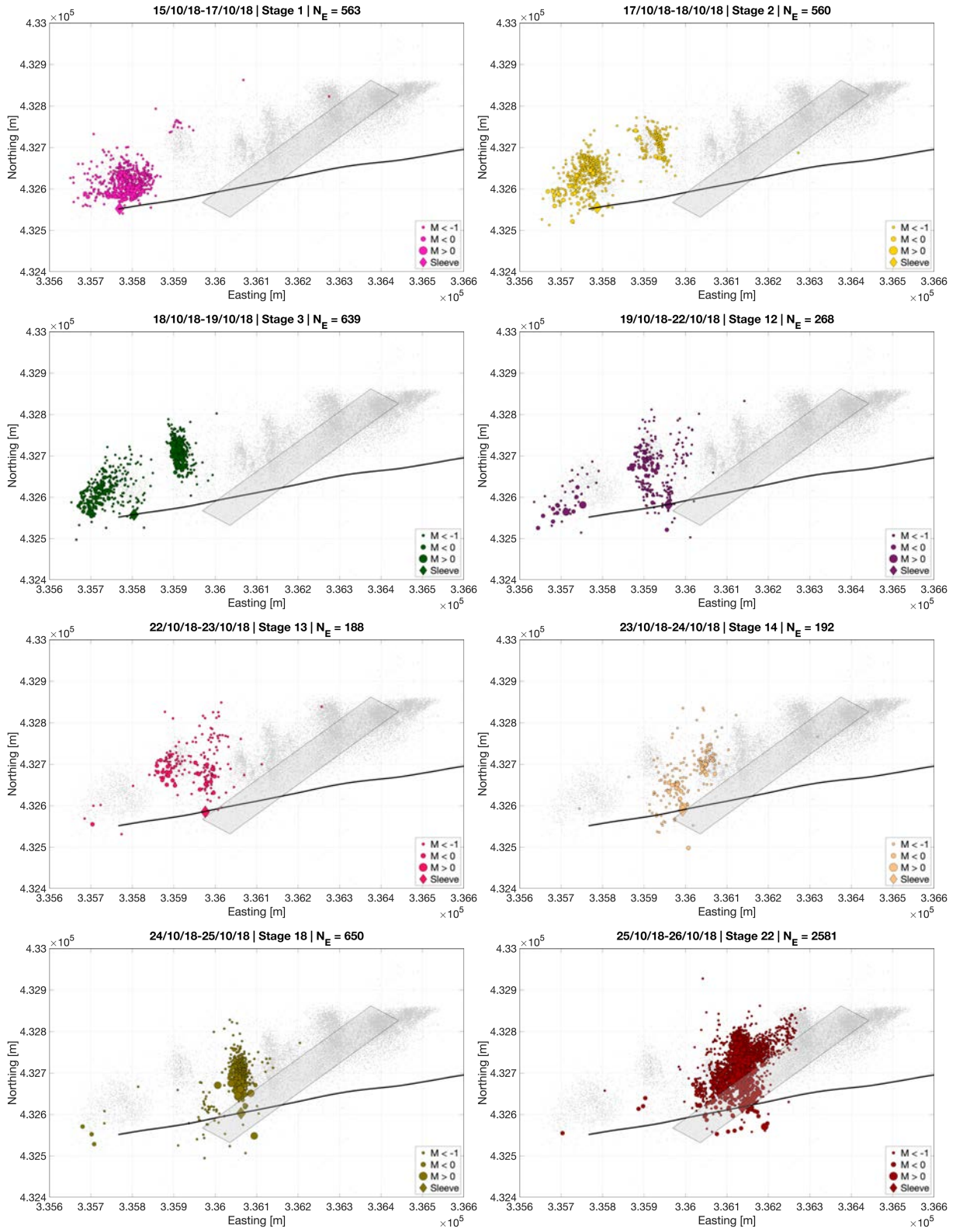
## REFERENCES

- Bao X. and D.W. Eaton, 2016. Fault activation by hydraulic fracturing in Western Canada: *Science* 354, 1406-1409.
- Clarke H., J.P. Verdon, T. Kettlety, A.F. Baird, J-M. Kendall, 2019. Real time imaging, forecasting, and management of human-induced seismicity at Preston New Road, Lancashire, England: *Seismological Research Letters*, *in press*.
- Chalmers G.R.L., D.J.K. Ross, R.M. Bustin, 2012. Geological controls on matrix permeability of Devonian gas shales in the Horn River and Liard Basins, northeastern British Columbia, Canada: *International Journal of Coal Geology* 103, 120-131.
- Cuadrilla Resources, 2018. Hydraulic Fracture Plan PNR 1/1Z. Accessed from: [https://consult.environment-agency.gov.uk/onshore-oil-and-gas/information-on-cuadrillas-preston-new-road-site/supporting\\_documents/Preston%20New%20Road%20HFP.pdf](https://consult.environment-agency.gov.uk/onshore-oil-and-gas/information-on-cuadrillas-preston-new-road-site/supporting_documents/Preston%20New%20Road%20HFP.pdf) on 20/7/2019.
- Deng K., Y. Liu, R.M. Harrington, 2016. Poroelastic stress triggering of the December 2013 Crooked Lake, Alberta, induced seismicity sequence: *Geophysical Research Letters* 43, 8482-8491.
- Dong T., N.B. Harris, K. Ayranci, C.E. Twemlow, B.R. Nassichuk, 2017. The impact of composition on pore throat size and permeability in high maturity shales: Middle and Upper Devonian Horn River Group, northeastern British Columbia, Canada: *Marine and Petroleum Geology* 81, 220-236.
- Economides M.J. and K.G. Nolte, 2003. *Reservoir Stimulation*, John Wiley and Sons, Chichester UK.
- Eyre T.S., D.W. Eaton, M. Zecevic, D. D'Amico, D. Kolos, 2019. Microseismicity reveals fault activation before  $M_w$  4.1 hydraulic-fracturing induced earthquake: *Geophysical Journal International* 218, 534-546.
- Ghanizadeh A., C. Clarkson, S. Aquino, O.H. Ardakani, H. Sanei, 2015. Petrophysical and geomechanical characteristics of Canadian tight oil and liquid-rich gas reservoirs: I. Pore network and permeability characterization: *Fuel* 153, 664-681.
- Green R.G., T. Greenfield, R.S. White, 2015. Triggered earthquakes suppressed by an evolving stress shadow from a propagating dyke: *Nature Geoscience* 8, 629-633.
- Hanks T.C. and H. Kanamori, 1979. A moment magnitude scale: *Journal of Geophysical Research* 84, 2348-2350.
- Harbaugh A.W., 2005. MODFLOW-2005, The USGS Geological Survey modular ground-water model – the ground-water flow process: U.S. Geological Survey Techniques and Methods 6-A16.
- Hearn E.H., C. Koltermann, J.L. Rubenstein, 2018. Numerical Models of Pore Pressure and Stress Changes Along Basement Faults Due to Wastewater Injection: Applications to the 2014 Milan, Kansas Earthquake: *Geochemistry, Geophysics, Geosystems* 19, 1178-1198.
- Holland A.A., 2013. Earthquakes triggered by hydraulic fracturing in south-central Oklahoma: *Bulletin of the Seismological Society of America* 103, 1784-1792.
- Igonin N., J.P. Verdon, J-M. Kendall, D.W. Eaton, 2019. The importance of pre-existing fracture networks for fault reactivation during hydraulic fracturing: *Earth and Space Science Open Archive*, DOI: 10.1002/essoar.10500976.1.
- Jones G.A., D. Raymer, K. Chambers, J-M. Kendall, 2010. Improved microseismic event location by inclusion of a priori dip particle motion: a case study from Ekofisk: *Geophysical Prospecting* 58, 727-737.
- Keranen K.M., M Weingarten, G.A. Abers, B.A. Bekins, S. Ge, 2014. Sharp increase in central Oklahoma seismicity since 2018 induced by massive wastewater injection: *Science* 345, 448-451.
- Kettlety T., J.P. Verdon, M.J. Werner, J-M. Kendall, J. Budge, 2019. Investigating the role of elastostatic stress transfer during hydraulic fracturing-induced fault reactivation: *Geophysical Journal International* 217, 1200-1216.

- Maxwell S.C., J. Shemeta, E. Campbell, D. Quirk, 2008. Microseismic deformation rate monitoring: SPE Annual Technical Conference, SPE116596.
- Maxwell S.C., M. Jones, R. Parker, S. Miong, S. Leaney, D. Dorval, D. D'Amico, J. Logel, E. Anderson, K. Hammermaster, 2009. Fault activation during hydraulic fracturing: SEG Annual Meeting Expanded Abstracts 28, 1552-1556.
- Maxwell S.C., J. Rutledge, R. Jones, M. Fehler, 2010. Petroleum reservoir characterization using downhole microseismic monitoring: *Geophysics* 75, A129-A137.
- Maxwell S.C., D. Cho, M. Norton, 2011. Integration of surface seismic and microseismic Part 2: Understanding hydraulic fracture variability through geomechanical interpretation: *Canadian Society of Exploration Geophysicists Recorder* 36, 26-30.
- Nordgren R.P., 1972. Propagation of a vertical hydraulic fracture: *Society of Petroleum Engineers Journal* 12, 306-314.
- Okada Y., 1992. Internal deformation due to shear and tensile faults in a half-space: *Bulletin of the Seismological Society of America* 82, 1018-1040.
- Perkins T.K. and L.R. Kern, 1961. Widths of hydraulic fractures: *Journal of Petroleum Technology* 13, 937-949.
- Profit M., M. Dutko, J. Yu, S. Cole, D. Angus, A. Baird, 2016. Complementary hydro-mechanical coupled finite/discrete element and microseismic modelling to predict hydraulic fracture propagation in tight shale reservoirs: *Computational Particle Mechanics* 3, 229-248.
- Questiaux J-M., G.D. Couples, N. Ruby, 2010. Fractured reservoirs with fracture corridors: *Geophysical Prospecting* 58, 279-295.
- Rogers S.F., 2003. Critical stress-related permeability in fractured rocks, in M. Ameen (ed.), *Fracture and In Situ Stress Characterisation of Hydrocarbon Reservoirs*, Geological Society of London Special Publication 209, 7-16.
- Schultz R., V. Stern, M. Novakovic, G. Atkinson, Y.J. Gu, 2015. Hydraulic fracturing and the Crooked Lake sequences: Insights gleaned from regional seismic networks: *Geophysical Research Letters* 42, 2750-2758.
- Shapiro S.A. and C. Dinske, 2009. Fluid-induced seismicity: pressure diffusion and hydraulic fracturing: *Geophysical Prospecting* 57, 301-310.
- Shapiro S.A., E. Huenges, G. Borm, 1997. Estimating the crust permeability from fluid-injection-induced seismic emission at the KTB site: *Geophysical Journal International* 131, F15-F18.
- Shapiro S.A., C. Dinske, E. Rothert, 2006. Hydraulic-fracturing controlled dynamics of microseismic clouds: *Geophysical Research Letters*, 33, L14312.
- Sneddon I.N., 1946. The distribution of stress in the neighbourhood of a crack in an elastic solid: *Proceedings of the Royal Society A* 195, 229-260.
- Stein R.S., 1999. The role of stress transfer in earthquake occurrence: *Nature* 402, 605-609.
- Toda S., R.S. Stein, T. Sagiya, 2002. Evidence from the AD 2000 Izu islands earthquake swarm that stressing rate governs seismicity: *Nature* 419, 58-61.
- Wang R., F Lorenzo-Martin, F. Roth, 2006. PSGRN/PSCMP – a new code for calculating co- and post-seismic deformation, geoid and gravity changes based on the viscoelastic-gravitational dislocation theory: *Computers and Geosciences* 32, 527-541. SPE Production and Facilities, SPE25890-PA.
- Warpinski N.R., Z.A. Moschovidis, C.D. Parker, I.S. Abou-Sayed, 1994. Comparison study of hydraulic fracture models – test case: GRI Staged Field Experiment No. 3: *Society of Petroleum Engineers SPE* 25890-PA.
- Wu Y-S. and K. Pruess, 2000. Integral solutions for transient fluid flow through a porous medium with pressure-dependent permeability: *International Journal of Rock Mechanics and Mining Sciences* 37, 51-61.



## APPENDIX I: MICROSEISMIC EVENT MAPS FOR EACH STAGE



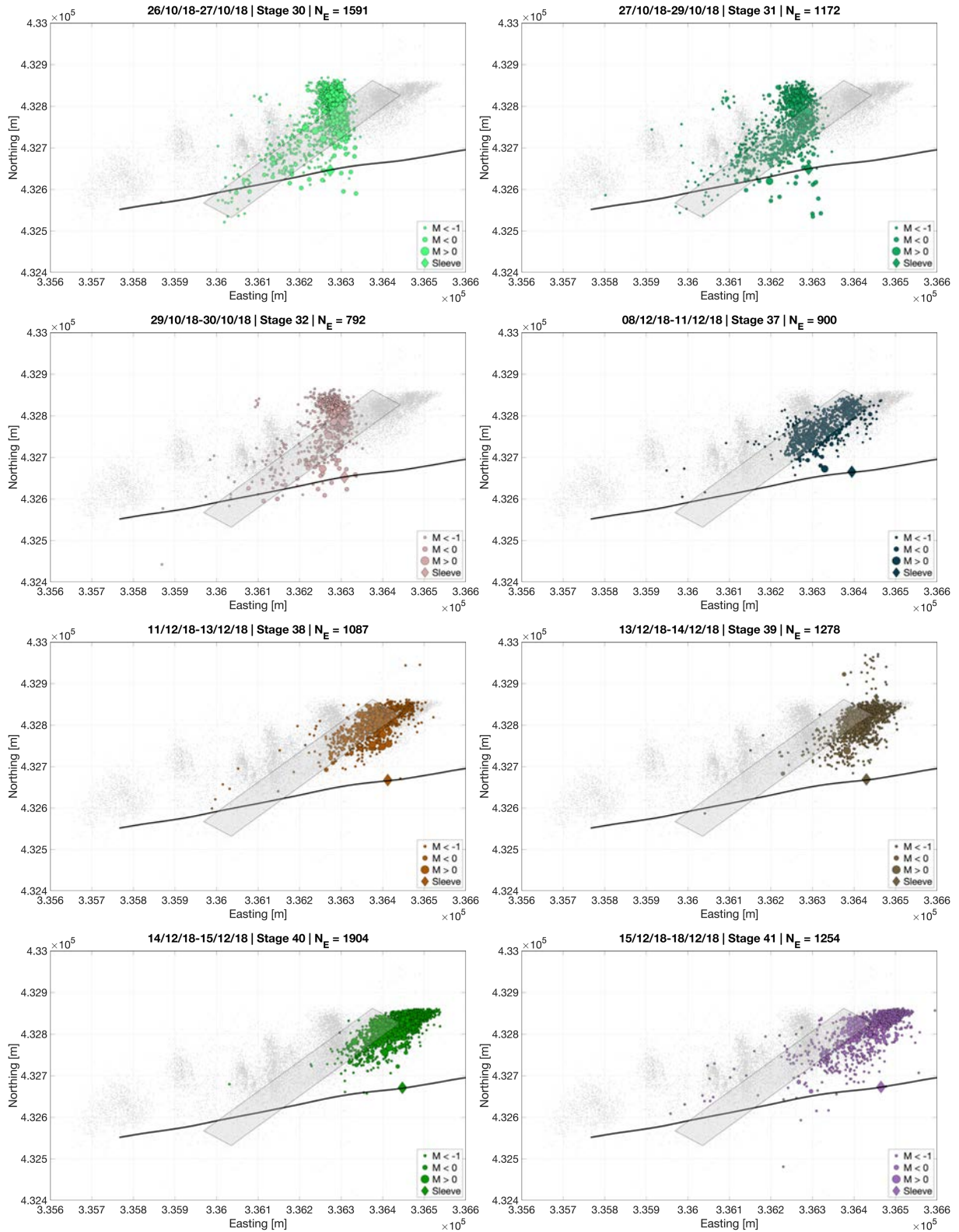
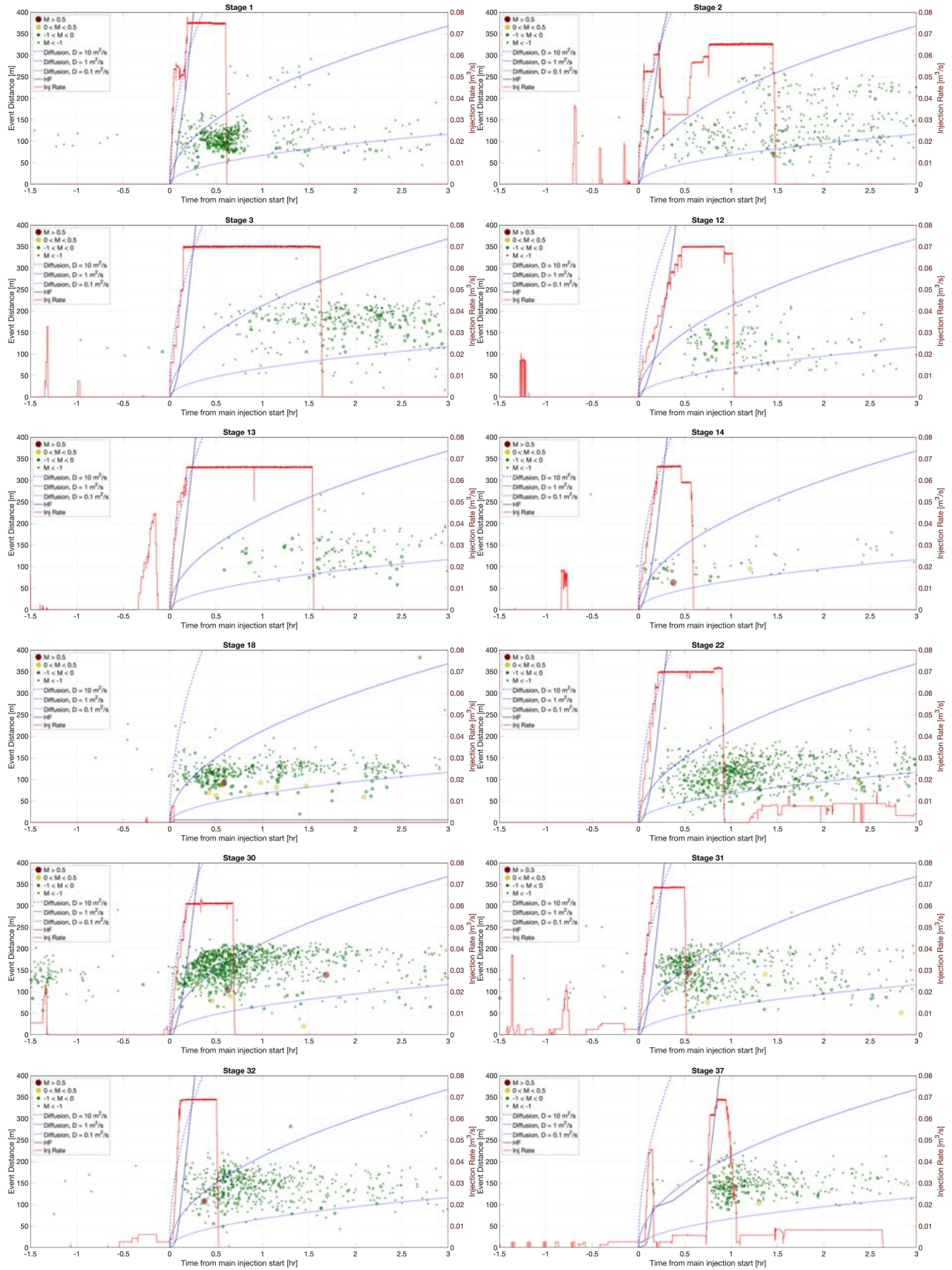


Figure A1.1: Microseismic event maps for each hydraulic fracture stage.

## APPENDIX II: DISTANCE VS TIME PLOTS FOR EACH STAGE



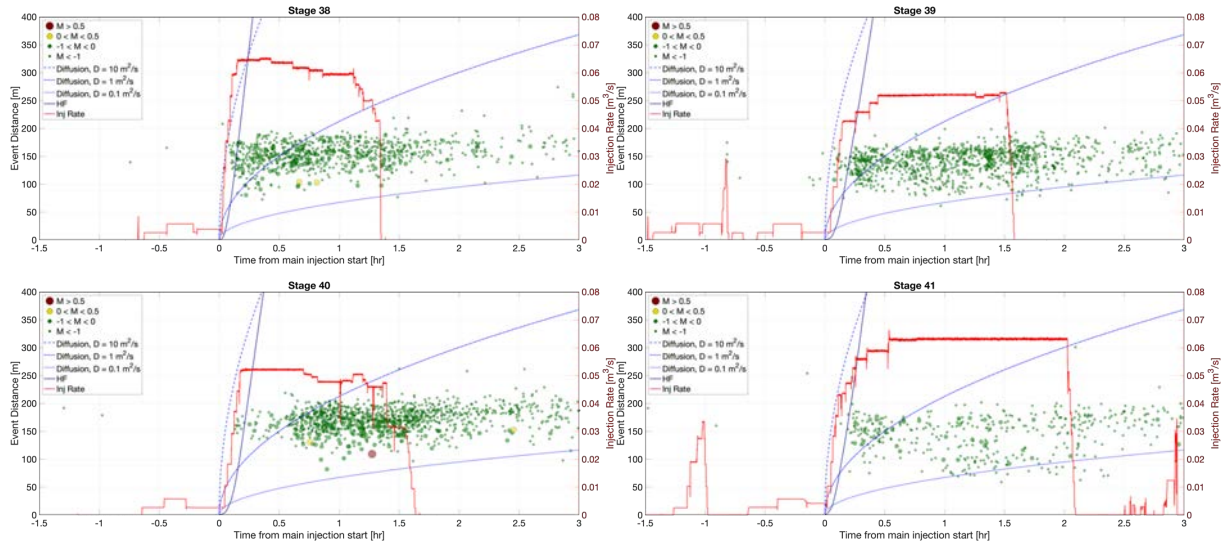
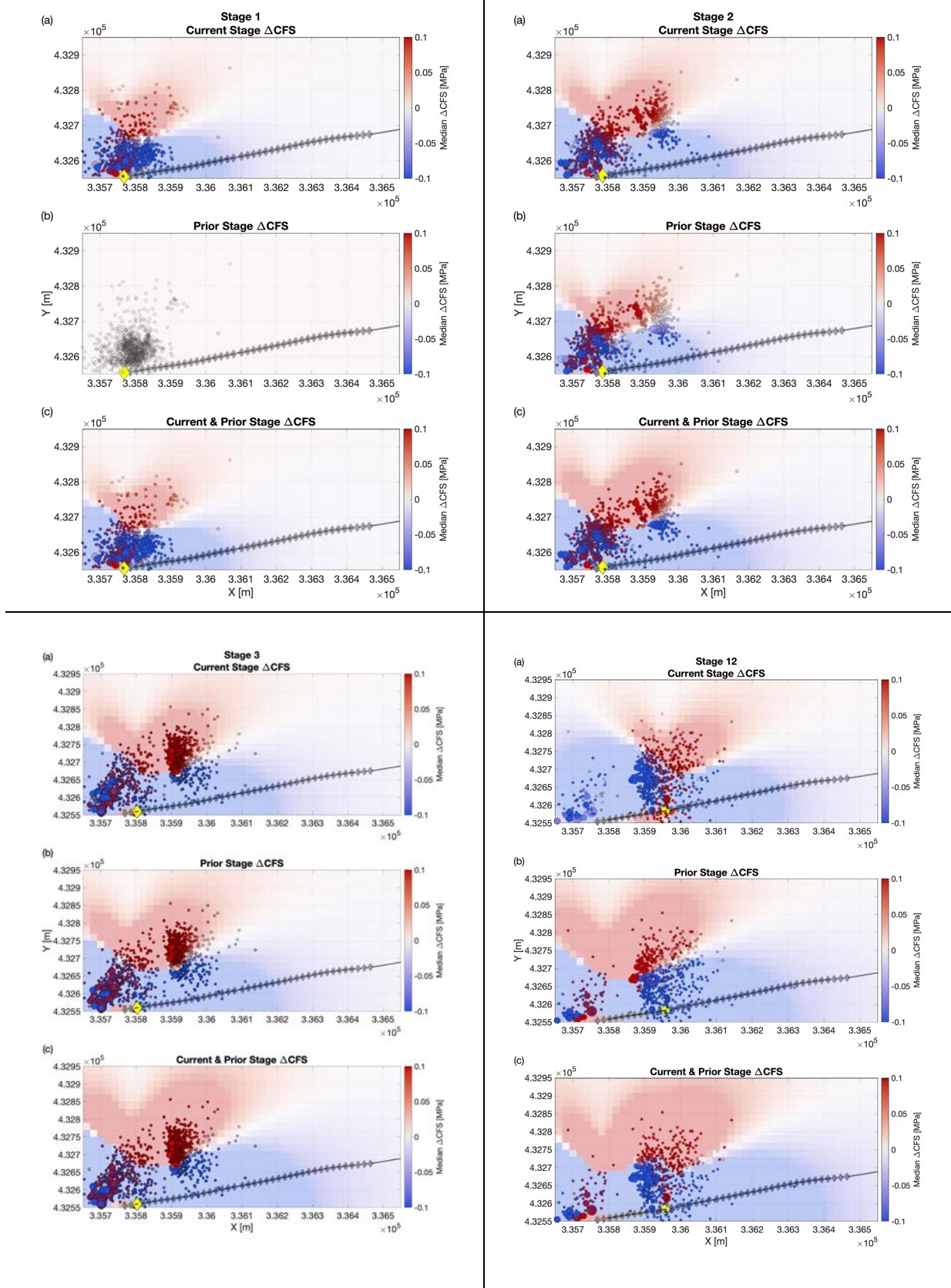
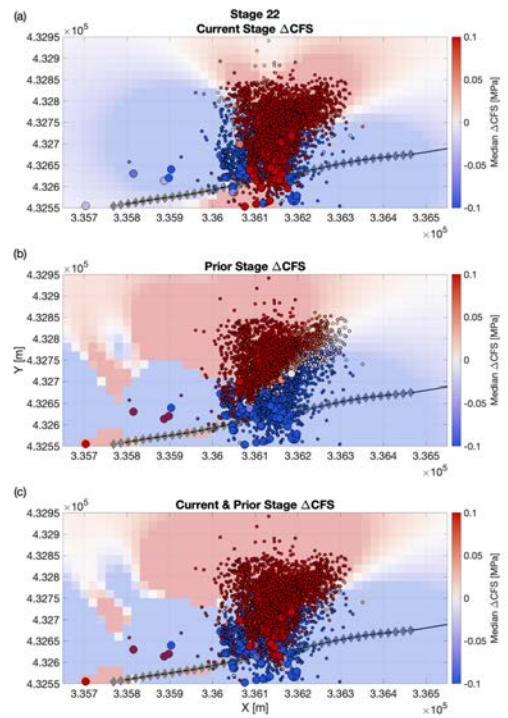
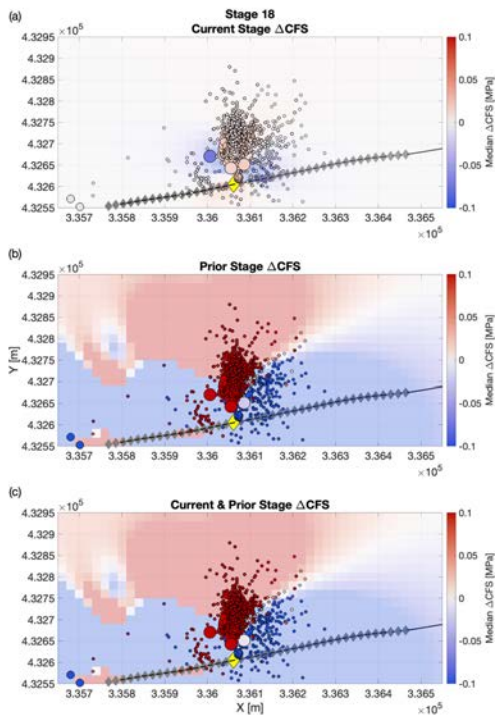
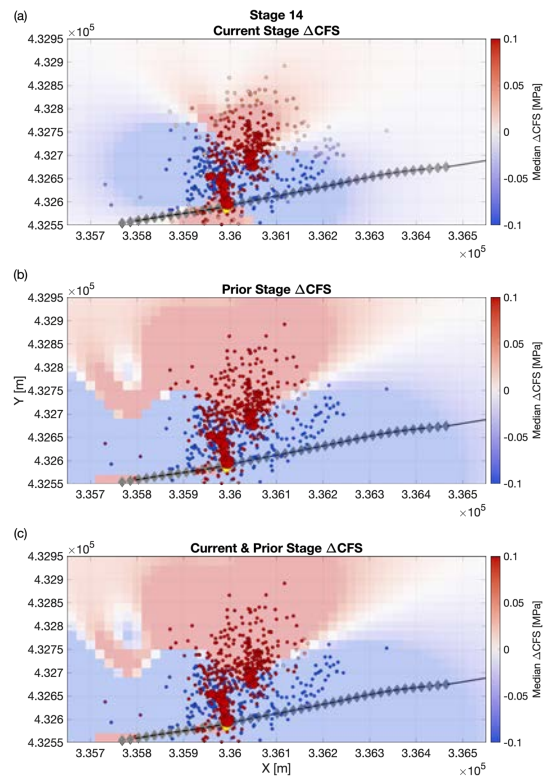
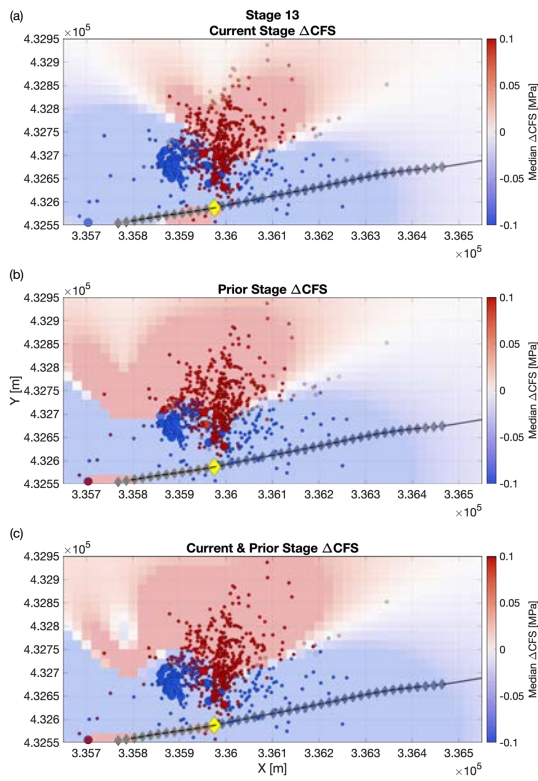
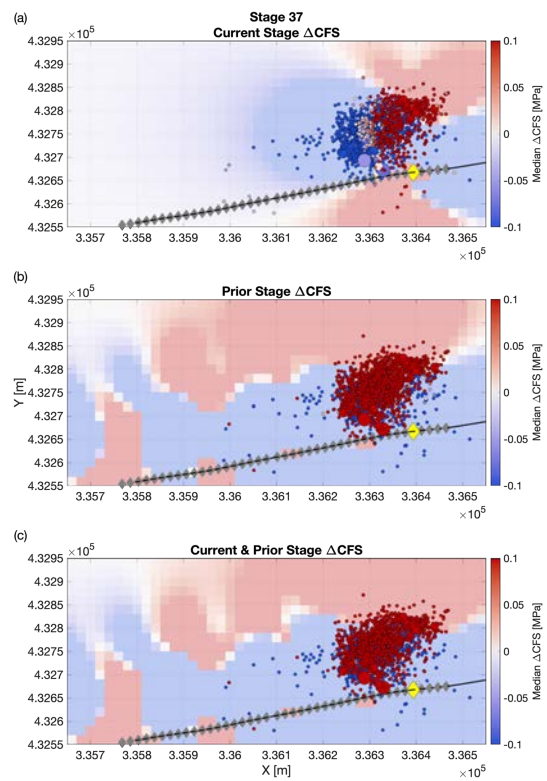
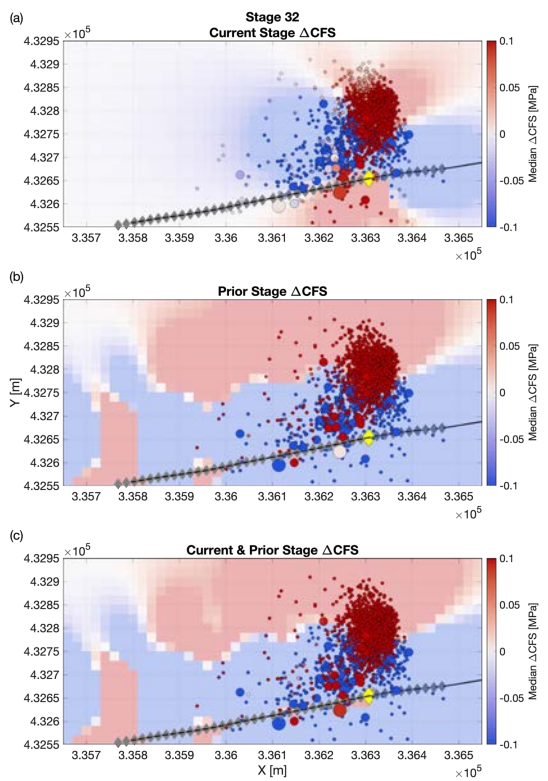
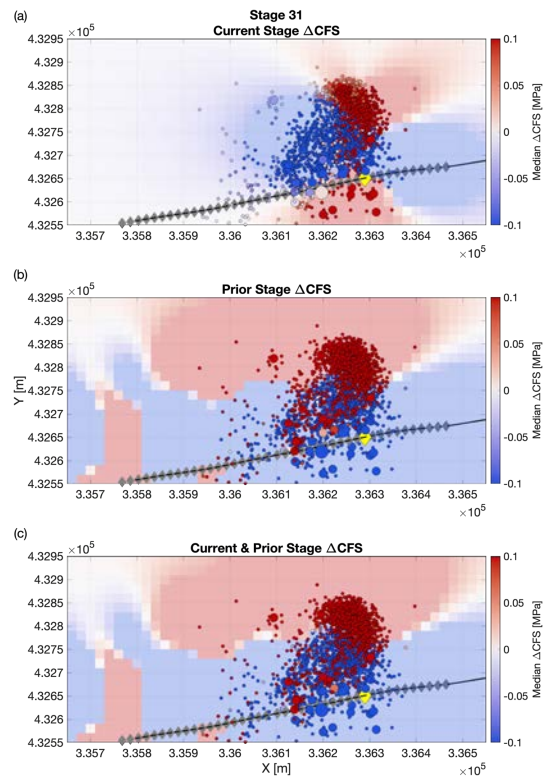
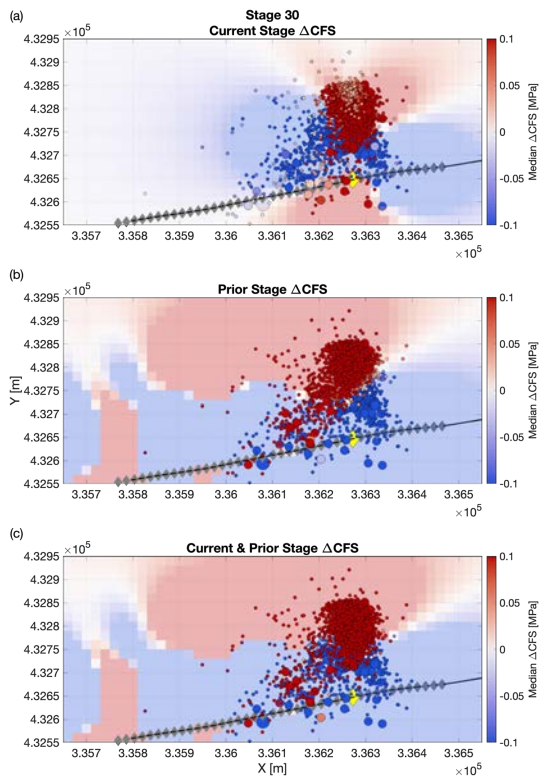


Figure A2.1: Distance of microseismic events (dots) from the injection point as a function of time, for each injection stage. The time-distance behaviour can reveal the underlying triggering cause. We also show the injection rate (red line), and the expected time-distance behaviour produced by diffusion models with  $D = 0.1, 1$  and  $10 \text{ m}^2/\text{s}$  (blue dashed lines), and a hydraulic fracture model assuming  $h_f = 25 \text{ m}$ ,  $w_f = 2.5 \text{ mm}$  and no fluid loss (black line).

## APPENDIX III: MODELLED $\Delta$ CFS FOR EACH STAGE







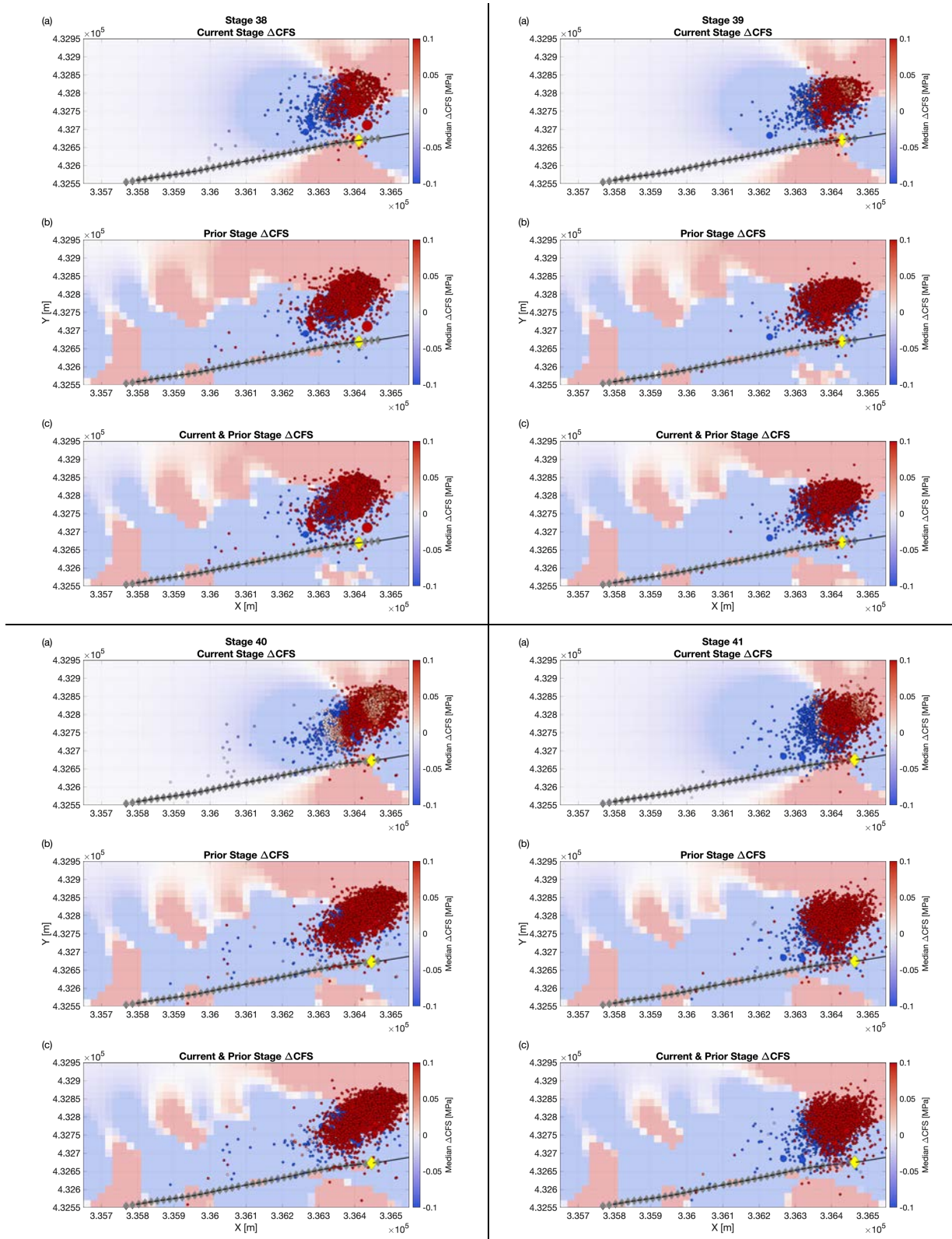


Figure A3.1: Coulomb failure stress changes for each Stage, showing  $\Delta CFS$  produced by the current stage (top panels), all previous stages (middle panels) and the combined current and previous stages (bottom panels). The microseismic events from each stage are also shown, coloured by the  $\Delta CFS$  received.

## APPENDIX IV: MODELLED $\Delta$ CFS FOR FAULTS

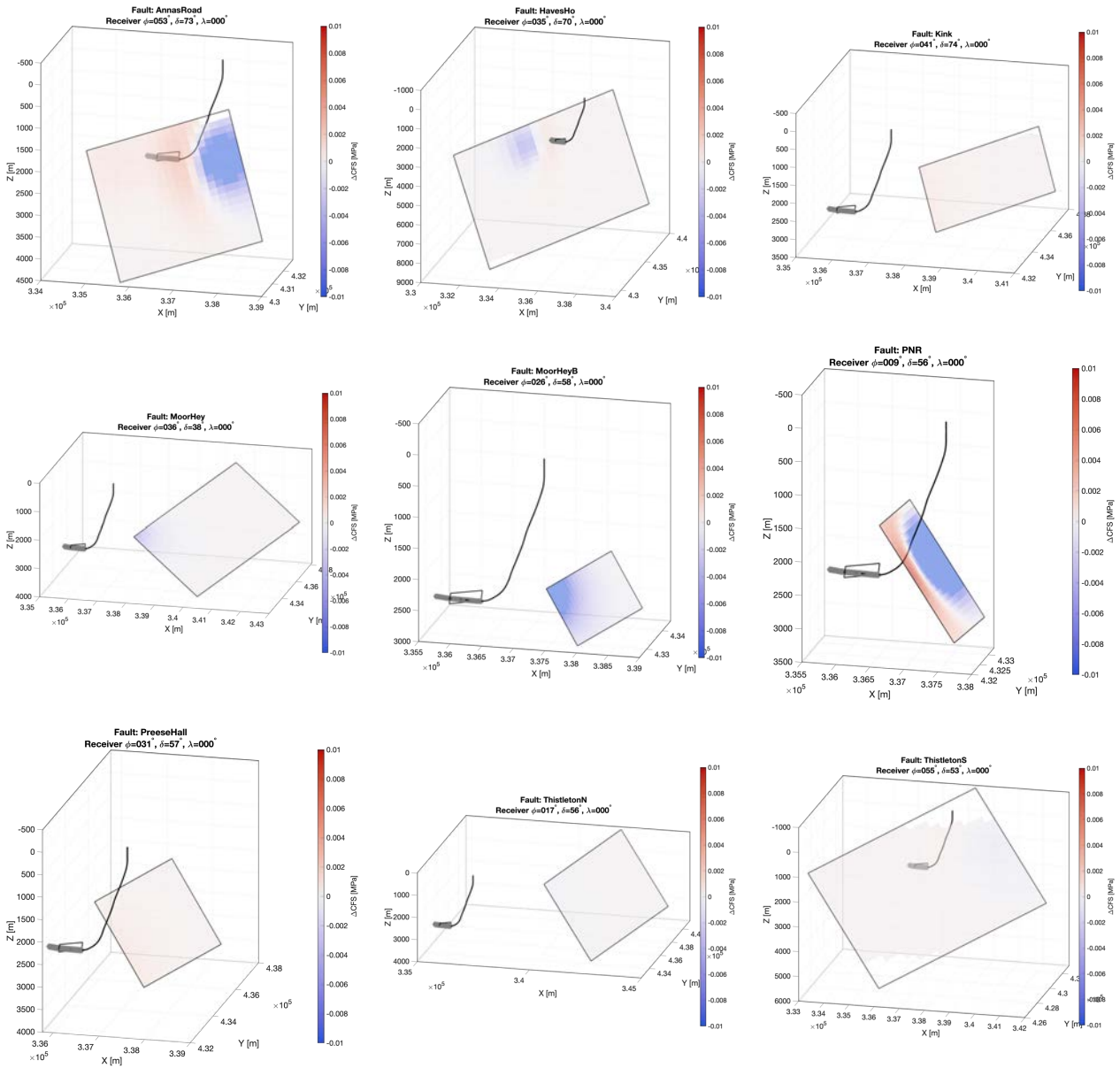


Figure A4.1: Coulomb failure stress changes resolved onto the larger, but more distant faults identified by CRL using 3D seismic survey data. Note that the colour scale is an order of magnitude smaller than that used in Chapter 3 for stress changes on the NEF-1 fault.

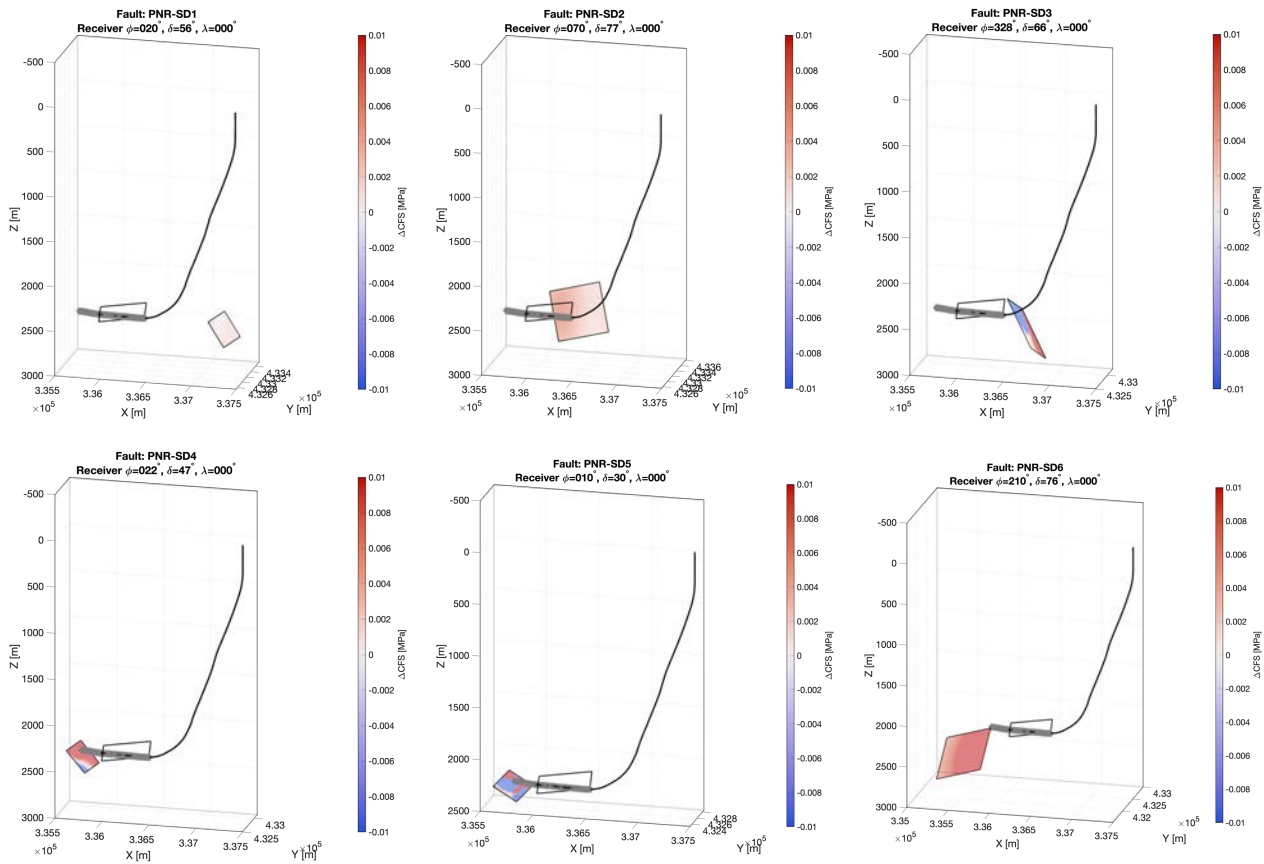
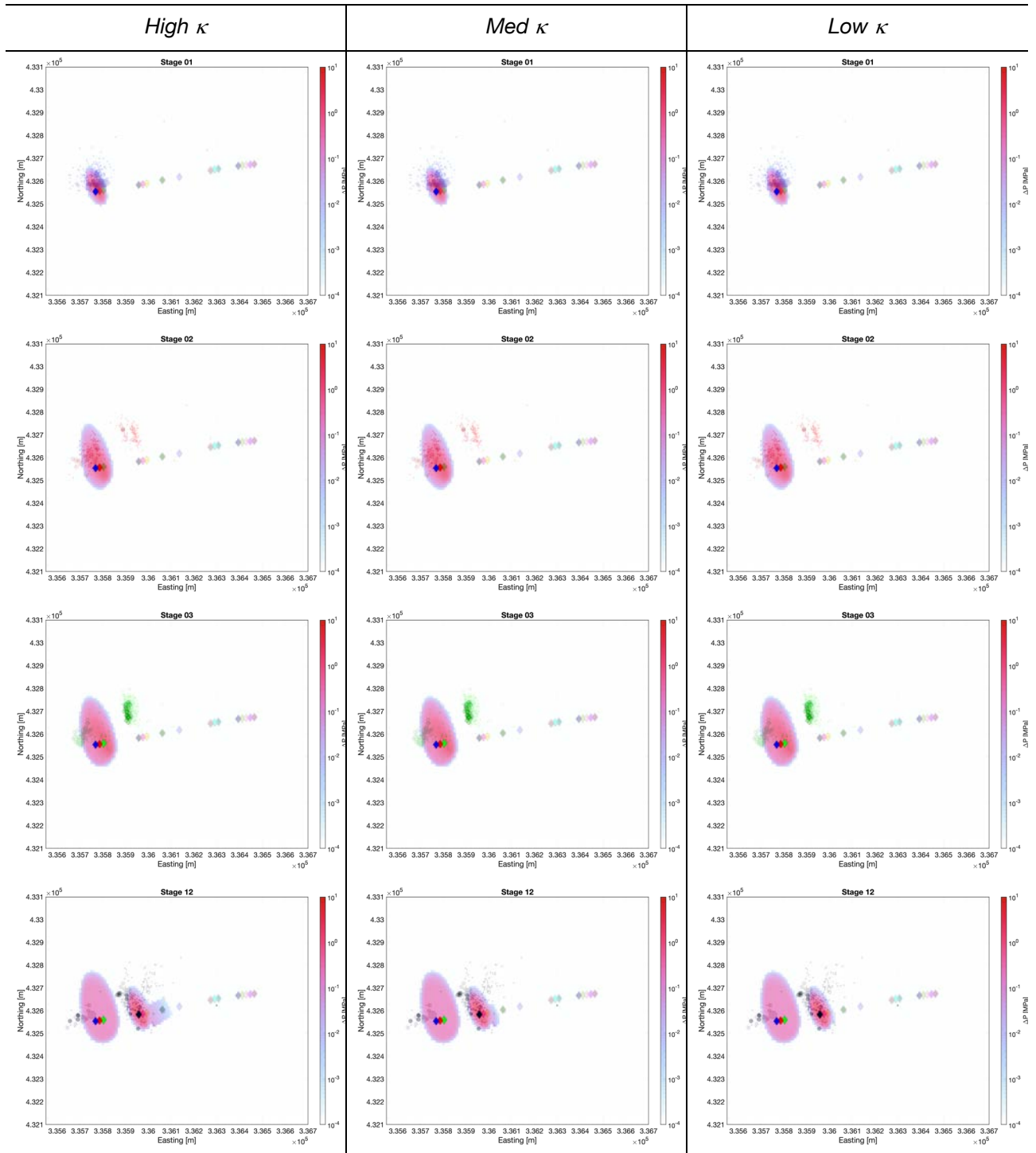
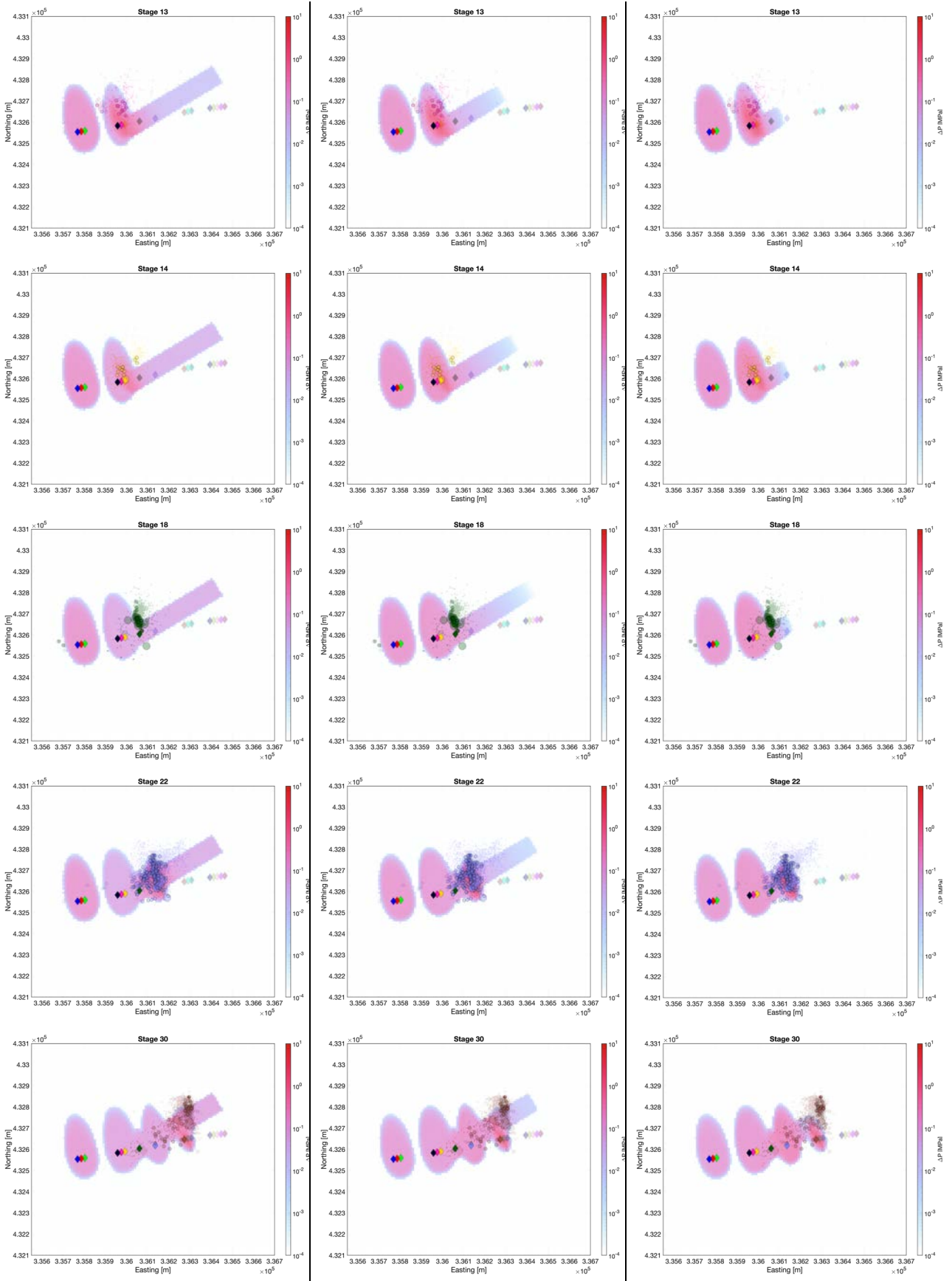
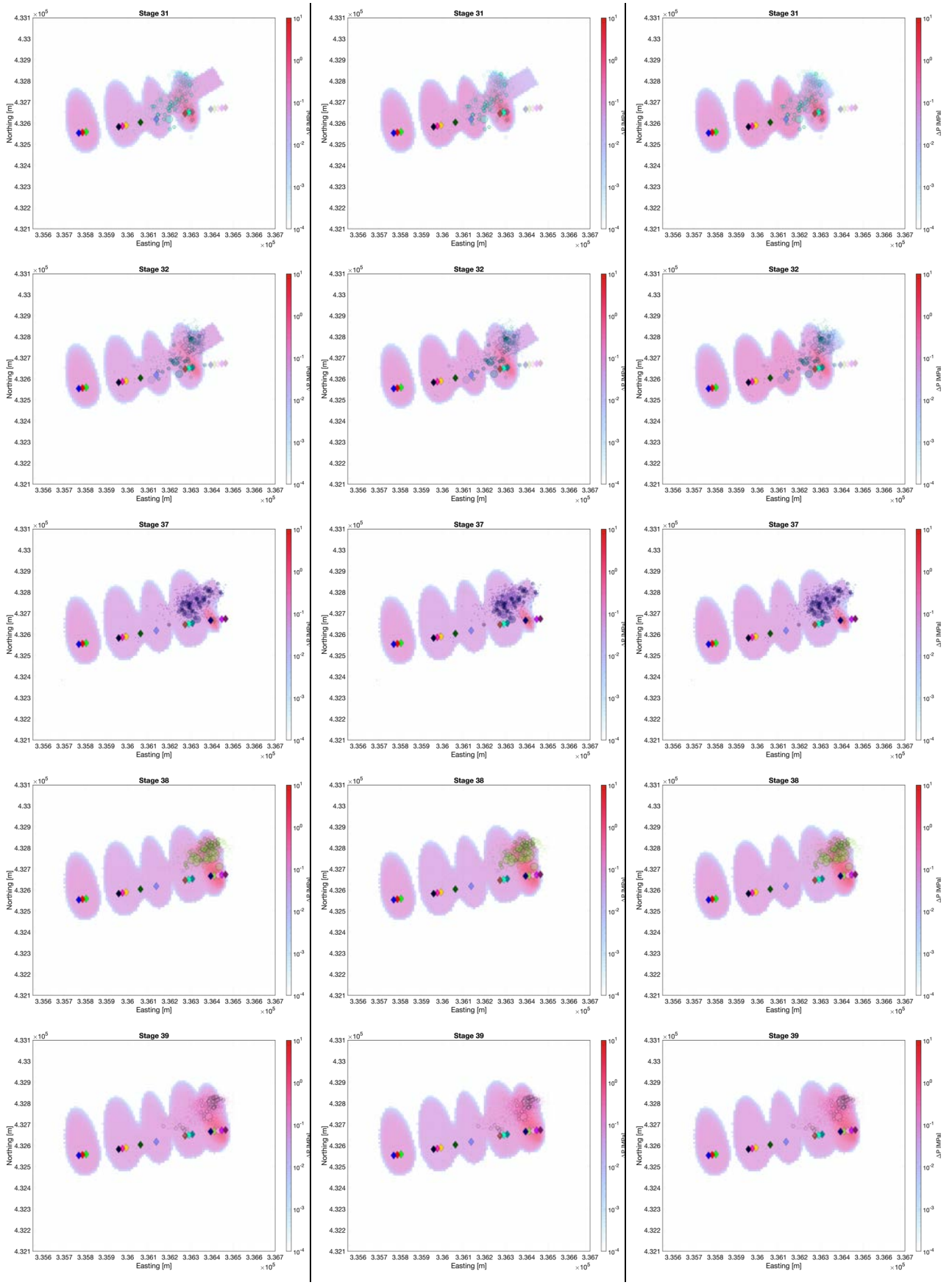


Figure A4.2: Coulomb failure stress changes resolved onto the “seismic discontinuities” identified by CRL using 3D seismic survey data. Note that the colour scale is an order of magnitude smaller than that used in Chapter 3 for stress changes on the NEF-1 fault.

## APPENDIX V: PRESSURE DIFFUSION MODEL RESULTS







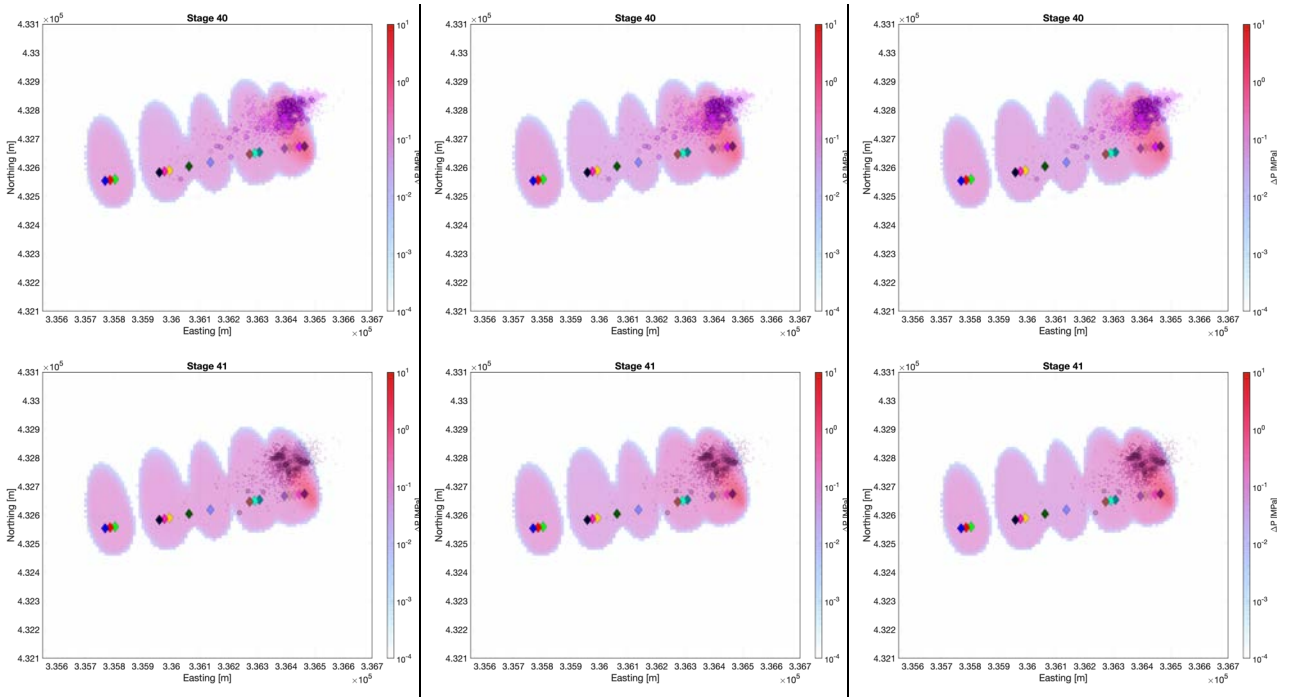
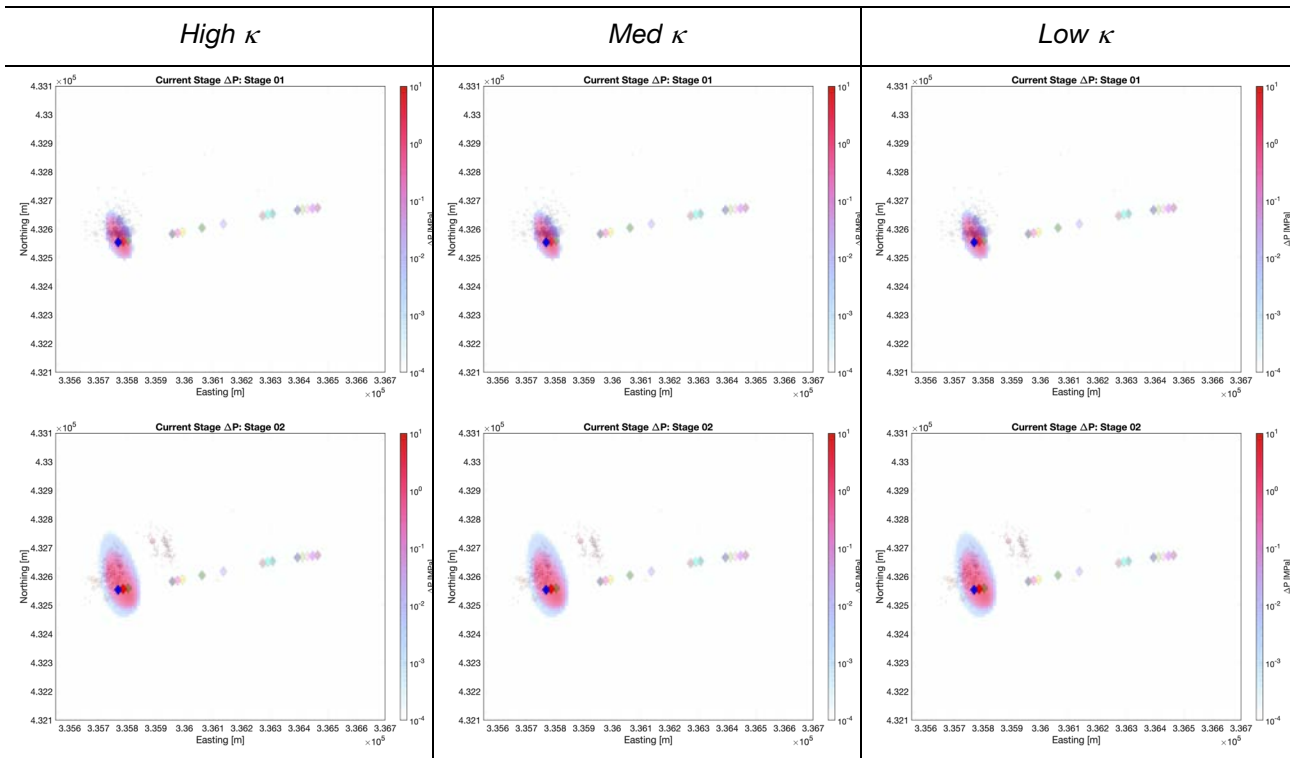
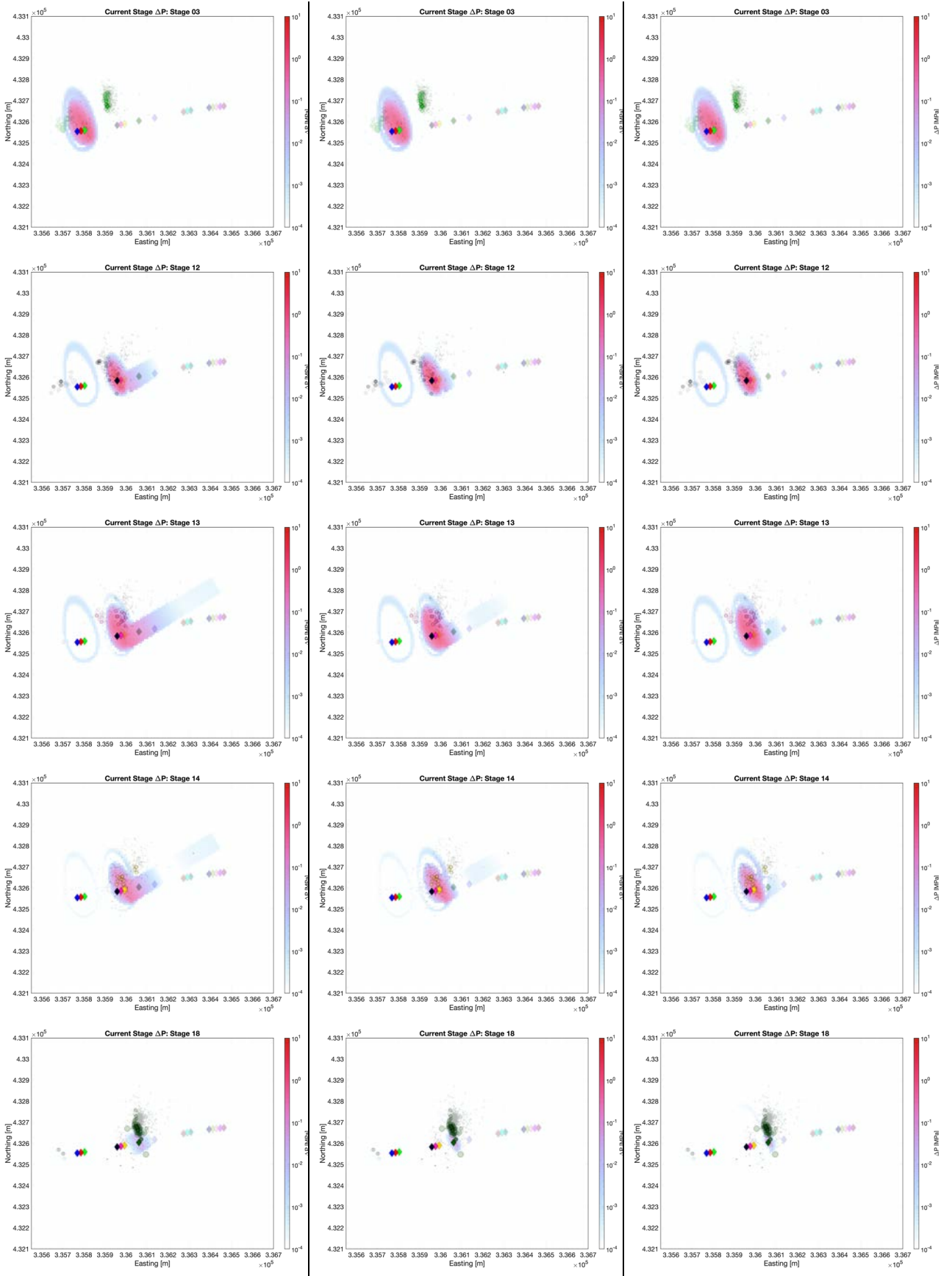
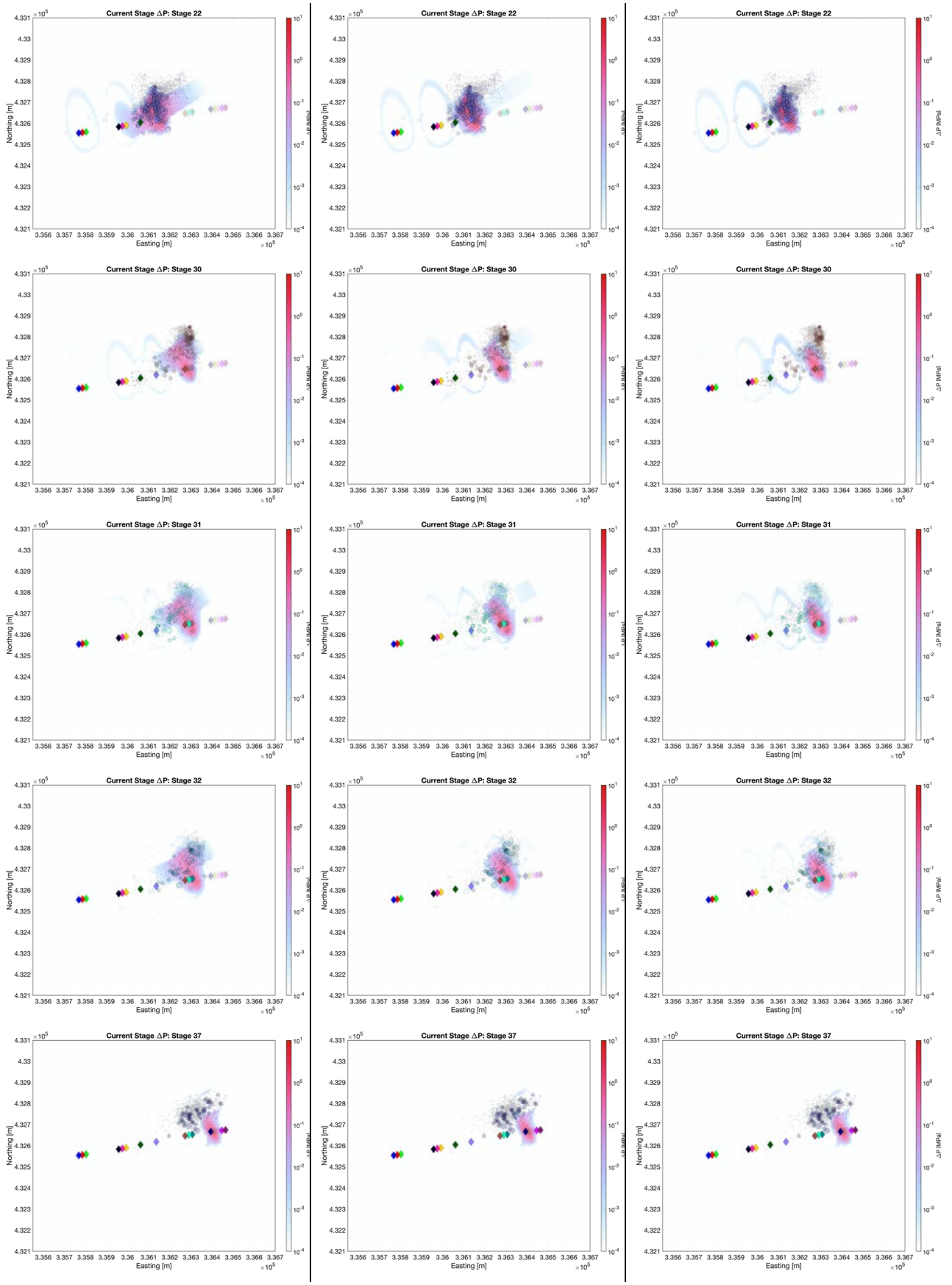


Figure A5.1: Map views of total modelled pore pressure increases from the start of stimulation to the end of each stage, with microseismic events overlain. In the left column, we assume that the NEF-1 fault zone has a high permeability ( $\kappa = 500$  mD), in the middle column we assume a moderate permeability ( $\kappa = 50$  mD), and in the right column we assume a low permeability ( $\kappa = 5$  mD). Pore pressures are contoured with a logarithmic scale.







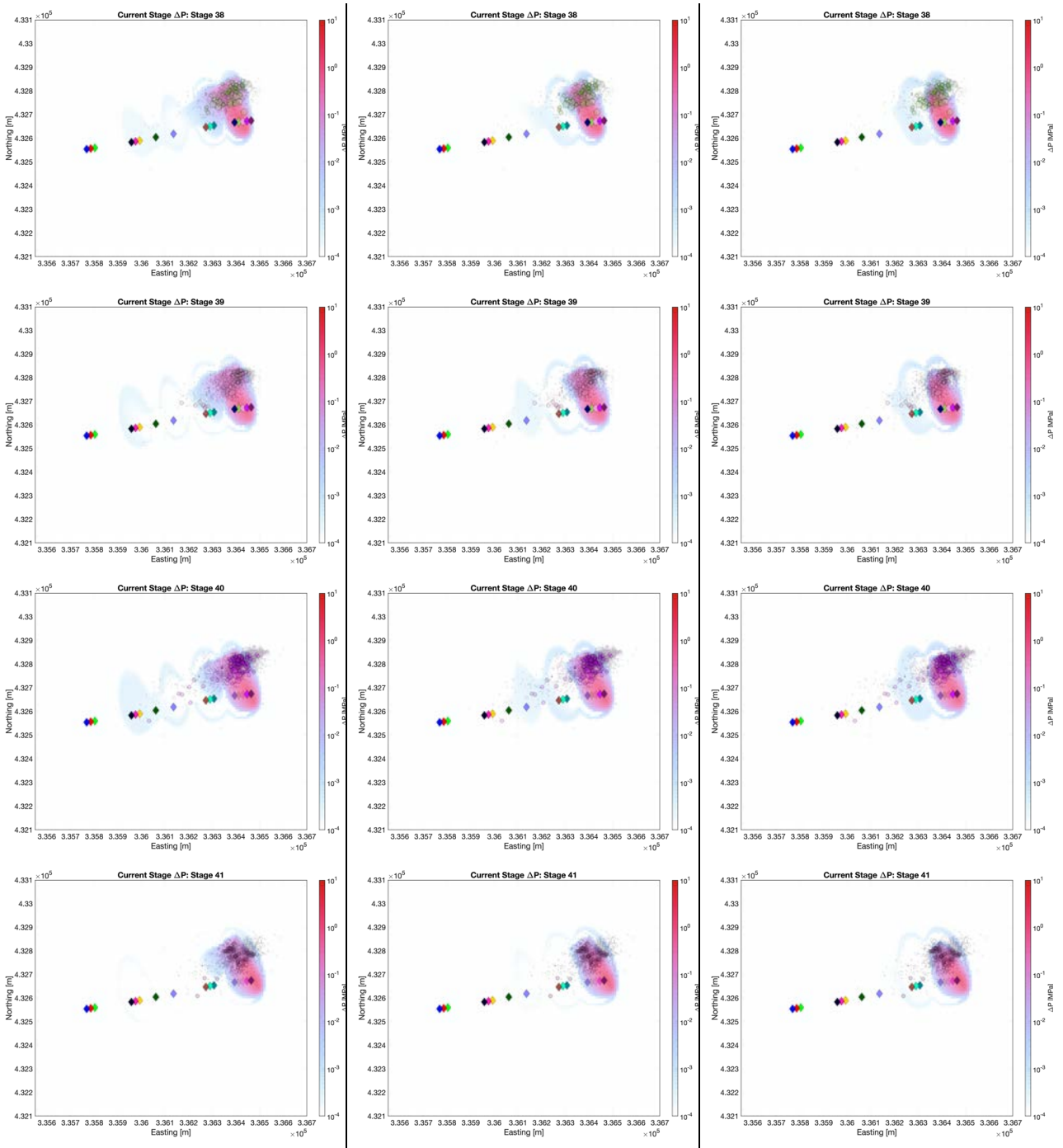


Figure A5.2: Map views of modelled pore pressure increases over the course of each stage, with microseismic events overlain. In the left column, we assume that the NEF-1 fault zone has a high permeability ( $\kappa = 500$  mD), in the middle column we assume a moderate permeability ( $\kappa = 50$  mD), and in the right column we assume a low permeability ( $\kappa = 5$  mD). Pore pressures are contoured with a logarithmic scale.

